

Analytical Investigation on the Underexpanded Jet Issuing from Circular and Elliptic Nozzles.

A thesis

Submitted to the Department of Mechanical Systems Engineering,

The University of Kitakyushu, Japan

in partial fulfillment of the requirements for the degree of

Doctor of Philosophy

by

Muhammad Minarul Islam

ID No. 2019DBA401



September 2022

Acknowledgements

I would like to express my gratitude and respect to my supervisors, Prof. Yoshiaki Miyazato and A/Prof. Shinichiro Nakao for choosing me as their research student of High-Speed Gasdynamics Research Lab and supervising my study at the University of Kitakyushu. A lot of thanks to their incessant advice, encouragement, and support inside and outside of the campus, I could finish this study and enrich my mind for the last three years in Japan.

I would like to express my gratitude to Mr. Yuta Kimura, Mr. Yusuke Awata, Mr. Ryota Fukunaga, Mr. Tatsuya Nagata, and other lab mates for their cooperation and assistance in my early established in Japan. Specially thanks to Mr. Ryota Fukunaga, and Mr. Tatsuya Nagata for supporting experimental investigation which help me to compare with theoretical results.

I express my gratitude to the Japanese government ‘MEXT’ scholarship program which contributed to accomplishing present investigation and exploring Japan life. In addition, I am also grateful to all staff of the University of Kitakyushu, especially I am indebted to all the staff of international support center of this university. I express my gratitude to Prof. Dr. Md. Mahmud Alam, Khulna University, Bangladesh and Prof. Dr. Rabindra Nath Mondal, Jagannath University, Bangladesh for their valuable encouragements and advise about Japan life which help me to perform present study successfully.

I am also very grateful to my parents and families. Particularly, I am expressing especial thanks to my better half and daughter for their endless affections, supports, nursing and sacrifices during the time of research which help me to complete my thesis in Japan. Finally, I express deep gratitude to my all friends, colleagues, and well-wishers.

Muhammad Minarul Islam
The University of Kitakyushu, Japan.

Abstract

The shock containing free jet emerging from a convergent-divergent nozzle with circular or elliptic shape at the exit has been investigated experimentally and theoretically. In the experimental investigation, the blowdown wind tunnel is used to generate a supersonic jet from round Laval nozzle with design Mach number of 1.5 followed by a cylindrical duct with an inner diameter of 10 *mm*, and length of 50 *mm*. Density measurements, and internal flow feature of the jet have been conducted using a rainbow schlieren deflectometry combined with the computed tomography to observe the three-dimensional structure of overexpanded and underexpanded jets. The effect of cylindrical duct on jet flow properties are examined. Contour, isopycnic visualizations and favorable flow characteristics of the cylindrical duct exit surface are also shown and discussed to compare the analytical results.

In the theoretical analysis, a modified vortex sheet model taking viscosity into account has been proposed. The first Fourier mode of eigenvalues expansion, and recurrence relations with orthogonal properties of Bessel's functions for circular jet and Mathieu functions for elliptic jet are executed to evaluate the explicit solution for inviscid and viscous jet respectively. The flow characteristics through convergent-divergent cylindrical and elliptic nozzle such as centerline pressure and density, density contours, density mesh have been calculated for the inviscid and viscous jet separately. Comparing with the Tam's and Emami et al. models, the results of modified model for both circular and elliptic jets are exhibited quantitatively good agreement with the rainbow schlieren deflectometry. The shock-cell spacing, and size measuring of elliptic jets have also been examined theoretically by aspect ratios (AR), nozzle pressure ratios (NPR) and design Mach numbers (M_d) arbitrarily and favorable output is shown in first time by comparing with the Rao's experiment for $AR = 7.72$. Finally, it has found that the modified elliptic model is presented more effective flow than the circular flow from their comparison. The calculated theoretical results may contribute to future investigate of the internal shock structure for large aspect scale, design of the advanced aircrafts with vessels, and so on where the effect of screech tones or noise, leakage, exhaustion, and plumes are momentous.

Nomenclature

Variables	Definition
α	: Mach angle
c	: speed of sound
e	: eccentricity
h	: enthalpy
l	: perimeter
m	: mass
p	: pressure
q	: vector velocity
r	: polar radial axis
γ	: specific heat ratio
t	: time
μ	: dynamic viscosity
v	: specific volume
τ	: shear stress
x	: Cartesian x -axis
y	: Cartesian y -axis
z	: Cartesian z -axis
ϕ	: velocity potential
ρ	: density
θ	: azimuth/ polar angle
ξ	: elliptic confocal
A	: cross-sectional area
β	: volume expansion
C	: specific heat
D	: diameter
E	: bulk modulus of elasticity
E	: internal energy
F	: body force
G	: mass flow rate

K	: coefficient of gas compressibility
L	: length
M	: Mach number
O	: center
P	: force potential
Q	: total thermal energy per unit mass
T	: absolute temperature
U	: axis velocity
V	: velocity
Δ	: increment
$\bar{\nabla}$: <i>vector differential operator</i>
AR	: aspect ratio
Re	: Reynolds number
NPR	: nozzle pressure ratio

Subscripts

b	: ambient
d	: design
e	: nozzle exit
j	: fully expanded
m	: major
n	: minor
p	: constant pressure
s	: shock-cell spacing
t	: turbulent
v	: constant volume
eq	: equivalent

Superscripts

*	: critical condition
---	----------------------

Table of Contents

Title	Page No.
Title of thesis	1
Acknowledgement	2
Abstract	3
Nomenclature	4
Table of Contents	6
Chapter 1 Introduction	9
1.1 Background	9
1.2 Objectives	12
1.3 Literature Review	13
1.4 Construction of the thesis	16
Chapter 2 Basic Principles of Compressible Flow	19
2.1 Introduction	19
2.2 Summaries of Thermodynamic Contents	20
2.2.1 Ideal Gas	20
2.2.2 Specific Volume	20
2.2.3 Equation of State	20
2.2.4 Specific Heat	21
2.2.5 Volume expansion, Compressibility and Bulk Modulus of Elasticity	21
2.2.6 Internal Energy	22
2.2.7 Enthalpy	23
2.2.8 Properties of First Law of Thermodynamics	23
2.2.9 Properties of Second Law of Thermodynamics	24
2.2.10 Combination of First and Second Law of Thermodynamics	25
2.2.11 Viscous and Inviscid Fluid	27
2.2.12 Viscosity	27
2.2.13 Governing Equations of Motion for a Gas	29

2.2.14	Speed of Sound	31
2.2.15	Mach Number	32
2.2.16	Geometrical Transmission of Sound Waves	33
2.2.17	Reynolds Number	35
2.2.18	Isentropic Flow, Nozzle and Diffuser	35
2.2.19	Isentropic Flow through a Duct	36
2.2.20	Isentropic Flow Relations for a Perfect Gas	40
2.2.21	Characterizes of a Perfect Gas through a Nozzle	43
2.2.22	Shock Waves	45
Chapter 3	Shock Containing Circular Jet	48
3.1	Introduction	48
3.2	Cylindrical Co-ordinates System	50
3.3	Experimental Apparatus and Method	52
3.4	Modified Model of Circular Jet	55
3.5	Results and Discussion	70
3.5.1	Experimental Analysis	70
3.5.1.1	Rainbow Schlieren Pictures	70
3.5.1.2	Density Contour Plots	71
3.5.1.3	Density Profiles along Jet Centerline	72
3.5.1.4	Effect of Cylindrical Duct	73
3.5.1.5	Three-Dimensional Jet Structure	74
3.5.1.6	Concluding Remarks of Rainbow Schlieren Pictures	75
3.5.2	Theoretical Analysis	76
3.5.2.1	Theoretical Density Profile along Jet Centerline	76
3.5.2.2	Theoretical Density Contour Plot	77
3.5.2.3	Theoretical Density Mesh Plot with Contour Plot	80
3.5.2.4	Conclusion Remarks of Theoretical Analysis	82
Chapter 4	Shock Containing Elliptic Jet	83
4.1	Introduction	83
4.2	Elliptic Cylinder Co-ordinates System	85
4.3	Modified Model for Elliptic Jet	87
4.4	Spacing of Shock-cell	102

4.5	Size of Fully Expanded Jets	104
4.6	Results and Discussion	106
4.6.1	Theoretical Analysis of Elliptic Jets	106
4.6.1.1	Comparison of Elliptic Centerline Density with Circular Profile	106
4.6.1.2	Theoretical Elliptic Density Contour Plots	108
4.6.1.3	Theoretical Elliptic Density Mesh Plots with Contour Plots	112
4.6.1.4	Analysis of Shock-cell Spacing	114
4.6.2	Conclusion Remarks of Elliptic Theories	115
Chapter 5	Conclusion	116
References		119

Chapter 1

Introduction

1.1 Background

The advancement of underexpanded and overexpanded jet study is one of the most important research components in the contemporary globalization. This unprecedented innovation of momentum with the passage of time has brought existence to a unique height where the high-speed jets development is directly unified. A couple of well-known researchers have been doing their works on the supersonic jet flow over the years integrated with the shock structure particularly the presence of shock waves which all are based on the characteristics of compressibility. The effects such as jet exhaust, plumes, noise, screech tone, ignition, combustors associate to the characteristics of mixing promoting and thrust producing propulsive schemes having their potential applications in fluid mechanics, aerospace and aeronautic engineering, aerodynamics, and others technical sectors which are brought revolutionary advances. Especially, broadband shock associated noise is one of the instances of supersonic jet which is set at the interface of the shock-cell with the turbulent vortexes in the shear layer and appeared as multiple crests on the far field spectra. At first, Harper-Bourne and Fisher [1] introduced such types of noise components for insight and forecasting of the intensity, spectrum and directivity of broadband shock associated noise. Later Tam [2] was also capable to predict the near and far field noise by the stochastic model for broadband shock associated noise. Reducing broadband shock associated noise and lucrative noise prediction methods are necessary to advance the jet exhaust systems for producing highly developed propulsive airframe engine of aeroacoustics engineering, because it can cause sonic fatigue failure. On the other hand, some control systems or operating condition needs refining to deal

the severity of these high-speed flows due to outflow of forced fluid or noxious leakage of gases as unintentional or misapplication sources and ballistic explosions with thermal diffusion as danger or lethal relevant reasons where the potentiality of mixing and propulsive is undeniable. The knowledge of risk prediction in each situation and link control of the overall structure of the jet can be compared with several physical parameters such studies referenced by Franquet et al. [3].

Recently, the design and fabrication of a micro-electro-mechanical systems (MEMS) has been increased to analyze the characteristics of high-speed jet through the axisymmetric microscale devices (such as micro-orifices, micro-nozzle, micro-valves) and asymmetric microscale devices (such as micro-slot, micro-rectangle, micro-hexagon, micro-elliptic nozzle, and so on). It is noted that the structural variation of fine crevices, notches, rips, and coarsened surfaces along with the nozzle exit geometry is one of the major tools for causing jet vortex and turbulent mixing. The shape, size and structural mechanism of the nozzle are also the most key factors affecting the jet flow. This is because jets size and features vary due to the differences of nozzle characteristics. For example, the shock wave structure of a rectangular nozzle is formed from the corner of the nozzle exit which blows to downstream and the Mach reflection scene is apparent on the surface of the incident shock wave. Parallely, the Mac disk is originated at the end of first cell. The shape of a Mac disk may be like a nozzle type, such as a square nozzle may produce square disk, round and elliptical nozzle would form circular and elliptical shape disk respectively and so on. Scroggs and Settles [4] first introduced axisymmetric nozzles that included a remarkable contribution in the supersonic microjets structures. Consequently, there are several experimental methods are qualitatively established in visualizing and analyzing the underexpanded supersonic jet flow, schlieren and shadowgraph optical techniques, Twyman-Green interferometry and Mach-Zehnder interferometry are one of them. These new optical setups [details in the section 1.3] including small satellite thruster in space engineering are effective by the microscale devices where mass-flow rate at a low Reynolds number and micro-propulsion system are vital components for the investigation of noise and shock-cell structures referenced by [5, 6, 7]. Additionally, the appropriate portion of the large-scale mass of vortices entering and small-scale mass of vortices transporting on the flow field is the perfect mechanism of the mixing augmentation. The small-scale mass transportation and mixing-promotion inherent characteristics are appeared simultaneously in non-circular nozzle due to the azimuthal asymmetry, whereas circular nozzle

is seen to be organized separately due to the axisymmetric studied inclusion from Kumar and Rathakrishnan [8].

The high-speedy free jets require a straightforward flow geometry, despite having the existence of turbulence and shock-cells decaying effects. It is good to know that the incompatibility of the nozzle outlet pressure and the ambient pressure at the off-design conditions is the reason to create supersonic jet comprises oblique shocks and expansion fans which are striking on the jet boundary as the quasi-periodic multi shock-cell structures. More clearly, a wave-series or waveguide of expansion-compression waves is formed and kept continuing to the ambient from the nozzle exits for recovering the mismatch of the static pressures. Tam et al. [9, 10], and Tam [11] were developed the Harper-Bourne and Fisher [1] progress by a multi-scales shock-cell model including the effects of slow jet propagation and turbulence attenuation. In fact, the turbulence, or supersonic schemes measurement with the advantage of mean flow properties is by far the most satisfactory of the inventions. Also, the turbulence structures of jet that mimics downstream and periodic waveguide modes and its permeability stimulates the turbulence blending progress at the wide range first introduced by Tam and Tanna [9]. Consequently, Morris and Miller [12] advanced a model through the average Reynolds average Navier-Stokes solution where required two parameters governing with the jet flow, nozzle pressure ratio and the total temperature ratio. They were explained the nozzle interior and exterior jet flow by the inbuilt two boundary conditions associated the nozzle geometry and ambient flow circumstances. Further, Kalyan and Karabasov [13] enhanced to predict the mixing noise, screech tone and broadband shock associated noise issued from axisymmetric and asymmetric convergent-divergent and convergent nozzle by their improved turbulence scale model. Usually at the lip region of convergent and convergent-divergent nozzle, these types of flow behavior have long been observed by the reference of Love et al. [14].

Apparently, the flow of underexpanded or overexpanded jet is influenced by the compressible properties of entire flow field. The effects of compressibility depend on the variation in density at high flow speed or substantial temperature changes, whereas the significant velocity changes yield substantial pressure variation. The theoretical advanced interests of the propulsive and mixing promotion yield into the pressure and density variation of axisymmetric and asymmetric underexpanded jets are increasing now. Because of authorized imperfectly expanded flow field of jet is analyzed by the various experimental

works where the axisymmetric and asymmetric nozzle are performed, rainbow schlieren deflectometry (RSD) [15] is one of the quantitative experiments. Although there are some studies of circular, rectangular, and elliptic supersonic jets that developed theoretically, Tam [16, 17] and Emami et al. [18] are one of them. Tam referred to as the vortex-sheet shock-cell model where the mixing layer of the jet is approximated by a discontinuous surface along the entire length of the circular, rectangular and elliptic jets, whereas Emami's model was the linearized theory taking the mean Reynolds stresses into account of the fully expanded circular jet only. Perturbation conservation equations were solved by the eigenfunction expansion, and the first Fourier mode is considered for the simplicity in both cases. Additionally, the explicit solution with shock-cell structures analysis of axisymmetric and asymmetric jets were discussed in Tam's model, but there has lack of explicit solution for the elliptic jets. Moreover, the theoretical understanding of circular and elliptic supersonic jet flow with 3D effect of jet boundary are one of the requirements now a days, despite having a quite bit of difficulties to analyze the shock-cell structures and shock-cell sizes due to their involuted phenomena and characteristics.

1.2 Objectives

The content of this thesis has been established basing on theoretical assumptions with the importance of shock containing jet flow where the kinematic and dynamic flow conditions must be employed. The first purpose is to establish a modified model for isentropic flow of fluid by extending the well-known Navier-Stokes equations where quiescent dry air and the Reynolds eddy viscosity is considered in the conservation of mass and momentum equations respectively. In momentum equation, the measured turbulent viscosity of Witzs [19] is modified for the fully developed jet by a variation term which makes a difference from the Tam's [16, 17] and Emami's [18] models. The isentropic energy equation is built up by considering the fully expanded speed of sound in terms of pressure changes due to density changes. In the boundary conditions, the change of pressure gradient due to downstream direction of flow is considered instead of velocity gradient where established other conditions are satisfied by the properties of dynamic and kinematic systems as well. Second purpose is to find the explicit solution of this modified model where the effects of eddy and without eddy are considered for the cylindrical and elliptic supersonic jet separately. Third purpose is to derive the density profile through the explicit solution of pressure for visualizing the centerline effects, contour effects and Mesh contour effects of shock containing for circular and elliptic

jet individually. Fourth purpose is to analyze the experimental results elaborately where the possible flow characteristics of round sonic jet are recognized by the rainbow schlieren pictures. Fifth, the calculated analytical results of circular and elliptic supersonic jets will have to compare with the Tam's [16, 17], Emami's [18] and the round jet data of rainbow schlieren experiment where the equivalent nozzle exit has to use for the validity of the modified model. Final wish is to develop the theories of fully expanded shock-cell size and shock-cell spacing through the nozzle exit diameter and compare with the experiment of Rao's [20] data for checking the error tolerance between developed theories and published data. Additionally, the perturbation techniques and the mean flow properties are used to linearize the modified model. The fast Fourier mode of eigenvalues problem has deemed to solve the modified theories where the mixing layer consider as the vortex sheet surface of Tam's [16, 17] concepts and mean Reynolds stress of Emami et al. [18] concepts are also taking into the account. The effects of arbitrary nozzle pressure ratios, arbitrary aspect ratios of nozzle exit geometry for elliptic jets, and arbitrary design Mach numbers are also provided sequentially to analyze the 3D density profile of shock-cell structures as a pioneer work. Though, the present elliptic analysis is rare significantly to compare with any reliable elliptic data either analytical or experimental, because lack of availability of verified references till now. Nevertheless, the results of elliptic jets help to future investigate of the internal shock structure for large aspect scale, design of the advanced aircrafts and vessels, increase the control system of conducting light gases, and so on where the effect of screech tones or noise, leakage, exhaustion, plumes are momentous.

1.3 Literature Review

The approach of using the analysis of underexpanded supersonic axisymmetric and asymmetric jets, reasonable accurate results may be possible to provide through the experimental and numerical works with mathematical simulations. To validate an analytical and computational model reliable experimental data are important. The availability of experimental data provides a scope to show stability of analytical results by comparing those results. The balance and compatibility equations for the compressible fluid representing a constitutive model that captures the characteristics of supersonic jets with laminar or turbulence shock waves suitably. As a laboratory experiment, the schlieren and shadowgraph techniques familiar with optical tools [21] have widely used earlier to understand and visualize the salient features of complex shock waves. The traditional schlieren strategies can visualize qualitative

flow because they require considerable effort to extract quantitative features. On the other hand, recent methods for quantitatively visualizing the field of jet density include laser-based interferometry such as Twyman-Green interferometry [22] and Mach-Zehnder interferometry [23, 24], or schlieren-based optical techniques such as background oriented Schlieren (BOS) [25], calibrated schlieren [26, 27], and rainbow schlieren deflectometry [28-30]. Among them, rainbow schlieren deflectometry measurement may be the easiest and effective optical system for quantitatively measuring the jet density field. The rainbow schlieren deflection measurement method is a variant but different from the conventional schlieren such as grayscale schlieren with knife edges and color schlieren with tricolor filters [21, 30] in that it can capture density field of flow with variable refractive index. In addition, rainbow schlieren deflectometry can be combined with computer tomography to measure the density field of 3D free jets [28]. A comprehensive and detailed review of the rainbow schlieren method is presented by Agarwal et al. [31] where includes theoretical and numerical algorithms, system design criteria, hardware setup, rainbow calibration, and density measurement methods. The leek peeler nozzle jets in rainbow schlieren deflectometry method has been carried out by Ezoë et al. [32] to improve nozzle peeling efficiency and explore a new nozzle with a higher removable potential for peeling leeks than the traditional nozzles. These newly invented nozzles are able to present complex issues such as noise associated screech tone frequency, turbulence scale of exhausted jet, expansion-compression waves, variation of density by analyzing the inside and outside features of the underexpanded or overexpanded flow.

Early working with high velocity jets, Powell [33] was the first to visualize data on the sound field and physical phenomenon of rectangular choked jets by shadowgraph technique. The high-intensity discrete-frequency acoustic noise referred to as the screech tone was the crucial clue of Powell. Hammit [34] also kept some contribution to measure the oscillating jet and sound fields in terms of the length of the shock-wave cells. The progress of theoretical assessment for measuring the shock cell structure and wavelength as well as shock-cell spacing of an imperfectly underexpanded supersonic jet issuing from orifice with the velocity of sound launched with the search of Prandtl [35]. He considered the velocity of efflux as the mean velocity and estimated the wavelength by using the slightly perturbed first term solution. Though his work based on the Emden's experimental results [36] where he used jets (air, carbon dioxide and hydrogen) exhibited approximated periodic structure known as wavelength for the first time. Successively, a linearized velocity potential equation derived from Euler equation of motion for compressible inviscid underexpanded jet was solved by Pack [37]. He

explored that the wavelength was expressed in terms of the mean velocity of the jet. He also modified the mean velocity of cylindrical jets as the bounding streamlines, but not the velocity of efflux which was the main difference from Prandtl model [35]. Satisfactory agreement was found by Pack's correction which is known as vortex sheet shock-cell model. Subsequent, the linearized pressure perturbation problems promoted as shock-cell noise problem was solved and developed by Tam [16] and Howe and Ffowcs-williams [38] respectively. Later, a numerical model of turbulent axisymmetric jet was developed by Seiner et al. [39] where they added eddy viscosity at first time in the governing equations. After few of research on the inviscid jet flow and shock feature, the characteristic of underexpanded screeching jet was used to determine the shock oscillation by the linearized solution of Panda [40]. However, all the jet flow model exhibits simple flow geometry and effective at near shock-cell, but there has lack of clear concept about later shock-cells. Further, Emami et al. [18] provided an analytical solution of under/over expanded turbulent supersonic jet by extending the Navier-Stokes equation where the mean Reynolds stress was considered. In their developed model, the Favre-averaged continuity and momentum equations for turbulence were used but neglected molecular viscous terms. The obtained outcomes were compared with inviscid experimental data, there has absent viscous comparison.

Shock-containing jets from elliptic nozzles exhibit significant flow features relative to round nozzles. Gutmark et al. [41] compared the mixing characteristics between the circular, elliptic and rectangular underexpanded jets and found that the elliptic and rectangular jets have a higher spreading rate when compared to the circular jet, especially at the minor axis plane. Kinzie and McLaughlin [42] compared aeroacoustics properties of supersonic round and elliptic jets and showed that elliptic jets radiate less noise than the round jet at comparable operating conditions. Menon and Skews [43] investigated the near-field shock structures of underexpanded sonic jets from square, rectangular, slot, and elliptic nozzles by the grey scale schlieren technique and Reynolds-averaged Navier-Stokes (RANS) simulations. Mitchell et al. [44] acquired the velocity fields and turbulent statics of underexpanded jets from a convergent nozzle with an aspect ratio of 2 at the exit using planar particle image velocimetry (PIV). Kumar and Rathakrishnan [8] obtained flow characteristics of supersonic jets from a design Mach number of 2 with an aspect ratio of 2 by Pitot probe measurements along the jet centerline and shadowgraph technique. Kalyan and Karabasov [13] proposed a new flow model to predict the broadband shock associated noise from axisymmetric and asymmetric jets and found that for the same thrust conditions, the elliptical nozzles lead to noise reduction at the source in

comparison with the corresponding axisymmetric jets. In addition, they showed that the area ratio (AR) of the major to minor axis dimensions at the exit of an elliptic nozzle increases, the number of shock-cells and their width reduces. Li et al [45] investigated flow characteristics of highly underexpanded jets from four different nozzles with the circular, square, rectangular, and elliptic shapes at the nozzle exit by the large eddy simulation (LES). They showed that the circular and square jets both correspond to a three-dimensional helical instability mode, while the elliptic and rectangular jets have two-dimensional flapping instability in their minor axis planes.

1.4 Construction of the Thesis

The present study is constructed by five chapters. Chapter 1 is allocated to the discussion of axisymmetric and asymmetric high-speed jets flow background and main objectives of this study with their important usages. Further, a literature review of the circular, rectangular and elliptic supersonic jet has been discussed through the authentic referenced papers. Lastly, chapter wise constructive summery is included to gather overall idea about the thesis.

In Chapter 2, some fundamental concepts with related definitions are discussed to understand the flow features, governing equations of motion and the characteristics of scalar and vector quantities of compressible fluid flow. Various flow configurations based on nozzle shapes have also been sketched to get the clear concept of such complex phenomena with behavior of supersonic flow.

Chapter 3 is titled by the Shock Containing Circular Jet. In the first section, the jet from a round Laval nozzle with a design Mach number of 1.5 followed by a cylindrical duct with an inner diameter of 10 *mm* and a length of 50 *mm* is investigated experimentally. Quantitative flow visualization of the jet issued from the duct exit is performed over a range of nozzle pressure ratios from 2.0 ~ 4.5 using the rainbow schlieren deflectometry combined with the computed tomography to investigate the jet three-dimensional structure. The flow features of the near-field shock systems in the jets are displayed with the density contour plot at the cross-section including the jet centerline. Effects of the nozzle pressure ratio on the density profile along the jet centerline are clarified quantitatively. In addition, a comparison between the present experiment and the previous one with a conventional Laval nozzle for jet centerline density profiles is carried out to examine the effect of the cylindrical duct. Furthermore, the three-dimensional structures of overexpanded and underexpanded jets are demonstrated with

the isopycnic surfaces to visualize the internal flow features. In the second section, a modified model of high-speed jet has to form where the turbulent viscosity [18] is considered and linearize by the assumptions of mean value properties with perturbation techniques. At the off-design condition of axisymmetric convergent divergent nozzle, the explicit solutions of normalized pressure and density profile have been derived for the fully expanded inviscid and viscous jet separately, where the mixing layer of the jets are approximated by the discontinuous surfaces along the entire length of the jet's idea linked with [16]. A quantitative comparison among the evaluated analytical results with the rainbow schlieren experiment, Tam's [16] theory and Emami's [18] theory has been constructed by the centerline density curves, contours of density profiles and Mesh plots with contour plots. In the final section, a very good promising conclusion is constructed about the proposed modified models and it's explicit solutions where the solution of inviscid jet is followed completely by the Tam's [16] model and the solution of turbulent viscous jet is shown the better agreements with the RSD experiment rather than Emami et al. [18] model. In the comparison section, the molecular interactions are neglected and the turbulent viscosity of Witz's [19] measure is modified by a variation term for the best fitting of the analytical results with the experiment upon the jet axis.

In Chapter 4, a theoretical analysis of supersonic elliptic jets has been constructed by employing the modified model of Chapter 3 to elliptic co-ordinates system, exploring the explicit solutions of pressure as well as density profile, and developing size and spacing formulas of shock-cell structures of Tam's [17] theories. In this section, the fully developed free jet is produced from the convergent-divergent asymmetric nozzle at exit elliptic cross-section under the off-design conditions where a mixing layer is replaced by thin vortex sheet with assumption of the inviscid flow inside the jet layer same as Tam's [16, 17] models. A downstream multi-shocks structure with periodic elliptic expansion and compression waves are developed where the maximum 25 expansion coefficients of Mathieu function has been considered in the MATLAB scripts first time. The fast Fourier mode of eigenvectors is used for the straightforward flow feature on the near shock-cell of nozzle exit. Further, the effects of major and minor axis planes of elliptic jet flow parameters are provided for the first time due to the arbitrary nozzle pressure ratios, aspect ratios, and design Mach numbers on the shock-cell structure. Additionally, the centerline density, contours, and mesh contours of fully expanded jet satisfied by the appropriate kinematic and dynamic boundary conditions have been measured and analyzed with the circular jet theories and experiment. Very favorable hypothetical results are found for the shock-cell spacings with Rao's [20] experimental result.

At the last part, a comprehensive analysis with conclusion is written as a pioneer work. A prominent quantitative output of fully expanded elliptic jet has been discussed and analyzed by theoretically and graphically with the arbitrary nozzle pressure ratios, arbitrary aspect ratios, and arbitrary design Mach numbers for the first time. From the comparison of elliptic and circular canonical field of shock containing jet, it is found that the elliptic jet exhibits better output than the circular jets, though the experimental results of round nozzle have been presented as a criterion in the comparison where the circular exit diameter is considered as an equivalent diameter in the elliptic jet for the betterment of the investigation.

In Chapter 5, a comprehensive conclusion of this study has been included for understanding the present work and feasibilities of further investigations. It is mentionable that the present analytical results of elliptic supersonic jet haven't compared directly to any data either theoretical or experimental because lack of available reliable references into the domain. Though, the newly investigated result may help, associate, and contribute some qualitative information significantly to increase and develop the knowledge of the high-speed jet flow field, especially in broadband shock associated noise prediction, reducing screech tones, jet mixing promotion matter and thrust propulsive systems. Finally, the studied journals, proceedings, symposiums, books and used links are listed into the Reference section.

Chapter 2

Basic Principles of Compressible Flow

2.1 Introduction

The compressible fluid flow causes variation in density pertaining to the gas dynamics because of compressibility effect. In favor of this concepts, gases (oxygen, helium, nitrogen, carbon dioxide, and so no) are treated as the compressible fluid. Variation in density arises considerably owing to large scale changes in pressure and temperature. Though, the large-scale pressure changes depend on the large-scale velocity changes of fluid. There is no doubt that the studies involving with the mechanics, aerodynamics, chemical kinetics, and thermodynamics where consider the compressibility effect have often been employing the basic concerns and principles on gas dynamics.

The basic principles and definitions that underlie the theoretical basis for the analysis of supersonic gas flow are the main assessments in this chapter. The analysis of gas dynamic problem concerns with the compressible fluid flow is based on the interrelationships among the below mentioned laws are referenced from [46, 47]:

- (i). The law of conservation of mass.
- (ii). Newton's second law of motion.
- (iii). The first law of thermodynamics.
- (iv). The second law of thermodynamics.

It is universally acknowledged that these laws are independent according to the principles of flowing fluid or flow process. Whereas the requirements of flow are fulfilled by the law of conservation of mass which is conveying the physical interpretation of the equation of continuity in the flow model. Newton's second law of motion can be described the kinetic and dynamic effects of fluid flow through the inertia frame which is referred as the momentum equation entire the governing form. The first law of thermodynamics states that the principle of the conservation of energy which is defined as the energy equation. And the second law of thermodynamics relates with heat interaction and irreversibility which is known as the entropy equation in the mathematical model of compressible fluid flow.

2.2 Summaries of Thermodynamic Contents

The following concepts, definitions, and relations of compressible fluid flow are referenced from [47, 48].

2.2.1 Ideal Gas

If the molecules of a gas have negligible volume and apparently there has no mutual attraction of molecules, then such gas is called ideal gas or perfect gas. Oxygen (O_2), hydrogen (H_2), nitrogen (N_2), carbon dioxide (CO_2), helium (He), and so on are the ideal gases.

2.2.2 Specific Volume

The volume which is captured by the unit mass of a gas, is defined as the specific volume, and denoted by v . Another way, the specific volume v is the reciprocal of the density ρ . The following expression can be written for the specific volume v ,

$$v = 1/\rho. \quad (2.1)$$

2.2.3 Equation of State

The well-known equation of state for ideal compressible fluid can be defined by the following relation among the absolute pressure p , specific volume v , specific gas constant of a particular gas R and the absolute temperature T which obey the perfect gas law,

$$pv = RT. \quad (2.2)$$

Using Eq. (2.1), then Eq. (2.2) becomes,

$$p = \rho RT, \quad (2.3)$$

At the atmospheric air, the gas constant R is considered 287.04 J/kg-K for the convenience. On the other hand, the ambient pressure p_b is 101.325×10^3 Pa and the ambient temperature T_b is 295 K. It is good to know that used all the components are measured in absolute scale.

2.2.4 Specific Heat

If the amount of heat required to raise the temperature of a unit mass of a gas by one degree, then the system is defined as specific heat of a gas which is denoted by C . The following expression can be written for the specific heat,

$$C = (\partial Q / \partial T) \quad (2.4)$$

where, δQ is the amount of heat required to raise the temperature δT . The constant volume process and the constant pressure process are the two well-known process to evaluate the specific heat of a gas. The following mathematical symbols are required to express such process:

$$\text{Specific heat at constant volume, } C_v = (\partial Q / \partial T)_v \quad (2.5)$$

$$\text{Specific heat at constant pressure, } C_p = (\partial Q / \partial T)_p \quad (2.6)$$

2.2.5 Volume expansion, Compressibility and Bulk Modulus of Elasticity

With the presence of shearing forces, the continuous deformation is exhibited by fluids. The gas is the perfect example of compressible fluid which shows the density (ρ) changes with the changes of pressure (p) and temperature (T). So, the total density changes ($d\rho$) can be expressed as the following way,

$$d\rho/\rho = (1/\rho) \times (\partial\rho/\partial T)_p dT + (1/\rho) \times (\partial\rho/\partial p)_T dp. \quad (2.7)$$

Using Eq. (2.1), the total volume changes (dv) can be evaluated as:

$$dv/v = (1/v) \times (\partial v/\partial T)_p dT + (1/v) \times (\partial v/\partial p)_T dp. \quad (2.8)$$

Now at the constant pressure, the comparative change in volume (or density) produced by an infinitesimal change of temperature is called the coefficient of volume expansion β as,

$$\beta = (1/v) \times (\partial v/\partial T)_p = -(1/\rho) \times (\partial \rho/\partial T)_p. \quad (2.9)$$

Similarly, at the constant temperature or isothermal process, the comparative change in volume (or density) produced by an infinitesimal change of pressure can be defined as the coefficient of gas compressibility (K) as

$$K = -(1/v) \times (\partial v/\partial p)_T = (1/\rho) \times (\partial \rho/\partial p)_T, \quad (2.10)$$

here, the minus notation bears the decreasing volume with increasing the pressure.

Finally, the quantity of bulk modulus of elasticity is defined as the ratio of volumetric stress to the volumetric strain. If a little enhances in pressure dp causes a change dv of the specific volume v , then the bulk modulus of elasticity (E) can be expressed as,

$$E = dp/-(dv/v) = \rho(dp/d\rho). \quad (2.11)$$

Using Eqs. (2.8) with (2.9) and (2.10), the expressions can be simplified as:

$$E = \frac{1}{K - \beta \times (dT/dp)}. \quad (2.12)$$

2.2.6 Internal Energy

The amount of heat which store in a gas is called internal energy and denoted by E . More clearly, when certain amount of heat is supplied to a gas, then temperature of gas or volume of gas or both may increase thereby performing some external work. The internal energy E of a perfect gas can be defined as follows by the temperature T only.

$$E = E(T) \quad (2.13)$$

Therefore, we can be added that the internal energy is directly proportional to the temperature which is known as kinetic energy theory.

2.2.7 Enthalpy

The enthalpy per unit mass of the system can be expressed by the sum of internal energy (E) and pressure specific volume product pv . If the enthalpy is denoted by h , then the total heat content or enthalpy is,

$$h = E + pv \quad (2.14)$$

2.2.8 Properties of First Law of Thermodynamics

Form the first law of thermodynamics which implies the law of conservation of energy, the change of internal energy (dE) can be written as,

$$dQ = dE + pdv, \quad (2.15)$$

where, Q is the total thermal energy per unit mass, E the internal energy per unit mass, p the pressure, and v the specific volume of a perfect gas. Using the specific heat properties of the perfect gas, then Eq. (2.15) becomes,

$$C_v = \frac{dE}{dT} = \left(\frac{\partial Q}{\partial T}\right)_v \quad (2.16)$$

$$C_p = \frac{dE}{dT} + p \left(\frac{\partial v}{\partial T}\right)_p = \left(\frac{\partial Q}{\partial T}\right)_p \quad (2.17)$$

Again, from Eq. (2.4), the following one can be derived,

$$\left(\frac{\partial v}{\partial T}\right)_p = R/p \quad (2.18)$$

By using Eq. (2.16) to (2.18), the following relation is built up,

$$C_p - C_v = R \quad (2.19)$$

Therefore, according to the kinetic energy theory we can say that C_v and C_p are constant for a particular gas which are carried out by the Eq. (2.16) and (2.17) respectively. Also, the ratio of C_p and C_v is known as adiabatic constant or specific heat ratio that is expressed by,

$$C_p/C_v = \gamma \quad (2.20)$$

From Eq. (2.19) and (2.20), it is clear that $C_p > C_v$ and $\gamma > 1$. It is mentionable that the specific heat ratio or adiabatic index is 1.40 for air, 1.41 for hydrogen, 1.30 for carbon dioxide, 1.66 for helium, 1.67 for argon and so on are used at the absolute temperature level to verify the one- or two-dimensional flow model.

2.2.9 Properties of Second Law of Thermodynamics

From the second law of thermodynamics, the concept of **irreversible process** has been carried from a process where both a system and its environment can be restored to its the initial states. Though, the irreversible process is performed at an infinitely slow rate, then the system becomes quasi-equilibrium entire the process. Again, a process which proceeds at a finite rate with finite potential differences is also irreversible. Similarly, an absolute scale of temperature with extensive property called **entropy** ideas are also introduced by the second law of thermodynamics. Entropy is a measure of the probability that a system is in a particular microscopic state and is associated with the irreversible of thermodynamic processes. In the reverse process, changes in the entropy of a fixed-mass system are due to thermal interactions only referenced by [47]:

$$dS = (\delta Q/T)_{rev} \quad (2.21)$$

For the irreversible process, the changes in entropy due to thermal interactions is as,

$$dS > (\delta Q/T)_{irrev} \quad (2.22)$$

If initial and final conditions are specified, the actual process will only occur if the change in entropy (dS) is greater than the value of $\delta Q/T$. Whether the path is reversible or irreversible, the change in entropy is the same. However, the heat exchange is less in an irreversible way. On the other hand, the reversible adiabatic process is called **isentropic** while the entropy remains constant.

2.2.10 Combination of First and Second Law of Thermodynamics

The significant measures p, ρ and T having their usual meaning which associate with the equation of gas state can be assembled as a pair of independent variables into any thermodynamical function ϕ where $v = 1/\rho$ is considerable referencing from [48].

If $\phi(p, v)$ be a function of p, v that depends only on the conditions at the initial (P_0) and any state (P), not other paths of joining P_0 to P , then $\phi(p, v)$ is called a function of state. According to the assumption of total differentiation, $\phi(p, v)$ can be written as,

$$d\phi(p, v) = M(p, v)dp + N(p, v)dv, \quad (2.23)$$

where, $M(p, v)$ and $N(p, v)$ depends on p and v only. Now, $d\phi(p, v)$ becomes an exact differential, if $(\phi_p - \phi_{p_0})$ independents of the path joining P_0 to P and fulfill the below mentioned necessary and sufficient condition of exactness.

$$(\partial M/\partial v)_p = (\partial N/\partial p)_v. \quad (2.24)$$

From Eq. (2.15) and (2.16) of first law of thermodynamics, it can write,

$$dE = C_v dT. \quad (2.25)$$

The perfect gas Eq. (2.4) can be written as,

$$dT = (1/R) \times d(pv). \quad (2.26)$$

Using Eqs. (2.25) and (2.26),

$$dE = \frac{C_v}{R} \times d(pv). \quad (2.27)$$

Now combining Eqs. (2.15) and (2.27),

$$dQ = \frac{C_v}{R} \times d(pv) + pdv. \quad (2.28)$$

$$\Rightarrow dQ = \frac{C_v}{R} \times (pdv + vdp) + pdv = \frac{C_v}{R} \times vdp + \left(1 + \frac{C_v}{R}\right) \times pdv.$$

$$\begin{aligned}
\Rightarrow dQ &= \frac{C_v}{R} \times v dp + \left(\frac{C_p}{R}\right) \times p dv; & [\text{using Eq. (2.19)}]. \\
\Rightarrow dQ &= T \left(\frac{C_v}{p}\right) \times dp + T \left(\frac{C_p}{v}\right) \times dv; & [\text{using Eq. (2.4)}]. \\
\therefore dS &= \left(\frac{C_v}{p}\right) \times dp + \left(\frac{C_p}{v}\right) \times dv; & [\text{using Eq. (2.21)}]. \quad (2.29)
\end{aligned}$$

Here, Eq. (2.29) and (2.23) are identical, then it can be expressed as,

$$M(p, v) = (C_v/p) \quad \text{and} \quad N(p, v) = (C_p/p).$$

Hence, $(\partial M/\partial v)_p = 0 = (\partial N/\partial p)_v$

which implies that the change of entropy dS is an exact differential; so, the entropy S is a function of state. By integrating Eq. (2.29) with the initial S_0 and final (S) conditions, then it becomes,

$$\begin{aligned}
S - S_0 &= C_v \ln(p) + C_p \ln(v). \\
\Rightarrow S - S_0 &= C_v \ln(p) + \gamma C_v \ln(v), \quad [\text{using Eq. (2.20)}]. \\
\Rightarrow \frac{S - S_0}{C_v} &= \ln(p) + \ln(v^\gamma) = \ln(pv^\gamma). \\
\Rightarrow pv^\gamma &= e^{\frac{S-S_0}{C_v}}, \quad (2.30)
\end{aligned}$$

since S is the entropy per unit mass and the flow is isentropic, then S is constant, though C_v and S_0 are obviously constant. Therefore, Eq. (2.30) can be evaluated as,

$$pv^\gamma = \text{constant}, \quad (2.31)$$

which is one of the properties of isentropic flow. It can also be written as,

$$\frac{p}{\rho^\gamma} = \text{constant}. \quad (2.32)$$

The following useful processes can be described basing on the above properties:

(i). Isothermal Process: In a process where the compression or expansion of a gas is happened at the constant temperature T , is called an isothermal process. For a perfect gas, Eq. (2.4) becomes, $pv = p/\rho = \text{constant}$ at the isothermal process.

(ii). **Adiabatic Process:** In a process where the compression or expansion of a gas holds a passage in such a way that the gas doesn't exchange heat with its surroundings, is called an adiabatic process. In the reversible adiabatic process, $pv^\gamma = \text{constant}$.

(iii). **Homentropic Process:** when the entropy of every single quantity of a gas of fixed mass is the same and remains constant with any change of the quantity, then such a change is defined as homentropic process.

2.2.11 Viscous and Inviscid Fluid

In generally, **body forces** and **surface forces** act on an infinitesimal fluid element where first one is proportional to the mass of the body and second one is proportional to the surface area. A fluid element enclosed in a surface (s) at the point p is depicted in the Fig. 2.1 where the unit element ds , normal stress, and shearing stress are marked significantly. Here the normal force per unit area is called **normal stress** or pressure and the tangential force per unit area is called shearing stress.

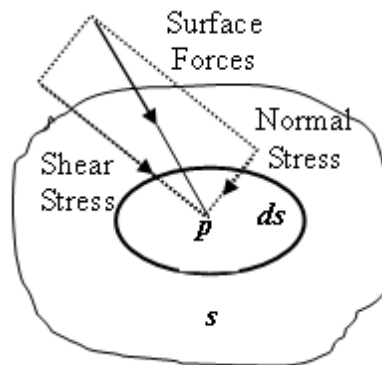


Fig. 2.1: Schematic view of normal stress and shear stress of a fluid.

Therefore, when normal as well as shearing stress is present in a fluid, then it is called a **viscous** or real fluid. Oppositely, when shearing stress doesn't exist, then it is called **inviscid** or non-viscous or perfect or ideal fluid. Water and air are the ideal examples of inviscid fluid.

2.2.12 Viscosity

Fluid viscosity is an important feature that can describe the properties of a fluid and control the conduct of shear stress in the case of angular distortion of the fluid. The strong background of viscosity is one of the measures of fluidity. In detail, viscosity is the amount of

internal reluctance that is exhibited when one layer of fluid is moved relative to another. Whereas the velocity gradient is due to the boundary layer that accumulates on the wall during the motion of real fluid. In the Fig. 2.2 is shown that at the wall velocity is zero and it increases up to the free-stream level outside the boundary layer. So, the construction of boundary layer bases on the effect of fluid viscosity is referenced from Saad [47].

Consider v be the velocity of the lower portion and $(V + dV)$ be the slightly increase velocity of the upper portion of two contiguous layers. The difference of the velocity of the extreme layers at the wall and the free stream is controlled by the boundary conditions. Since the upper layer is faster, there is a net momentum transport from the upper layer to the lower layer. While balancing this motion of flow, there is a shear force between the two layers, dragging the slower layer to the fast-moving layer.

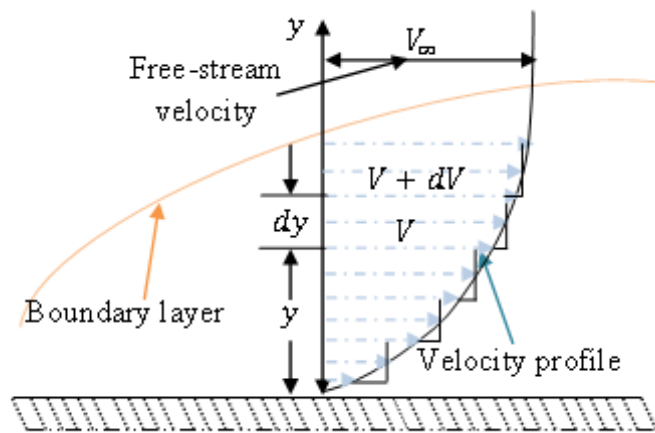


Fig. 2.2: Effect of velocity gradient with viscosity to construct the boundary layer.

For the most exposed fluids, the proportional relation between shear stress and rate of strain can be expressed as the following way,

$$\tau \propto \left(\frac{dV}{dy}\right),$$

where, τ and (dv/dy) indicates the and the velocity gradient respectively. By assigning a proportionality constant, the above shear stress relation becomes,

$$\tau = \mu \left(\frac{dv}{dy}\right), \quad (2.33)$$

where, used constant μ is called the coefficient of viscosity or dynamic viscosity which is familiar as **Newton's law of viscosity**. So, the fluid which follows this characteristic is called **Newtonian fluid** and which doesn't follow is called **non-Newtonian fluid**.

It is important to know that the coefficient of viscosity is a characteristic of fluid which is independent of the flow geometry but depends on pressure and temperature. Because the gases viscosity is increased, whereas the liquid viscosity is decreased with increasing the temperature. So, the viscosity of perfect gases can be defined as the function of only molecular dimensions and of absolute temperature through the kinetic theory of gases. On the other hand, the coefficient of viscosity is zero for the perfect gases or inviscid fluids.

2.2.13 Governing Equations of Motion for a Gas

(i). **The Equation of Continuity:** The inherent objective of the equation of continuity is expressing the law of conservation of mass where the motion of fluid is continuous. The main premise of the law of conservation of mass is that the fluid mass would neither be created nor be destroyed. Based on this assumption, the equation of continuity describes the fact that at any given time, the increase in the mass of the fluid on a closed surface drawn in the fluid must be equal to the excess of the mass flow out over the flow mass. The below vector form is known as the equation of continuity that holds all points of fluid free from sources and sinks,

$$\partial\rho/\partial t + \nabla \cdot (\rho\mathbf{q}) = 0, \quad (2.34)$$

where, $\nabla = (\partial/\partial x)\hat{i} + (\partial/\partial y)\hat{j} + (\partial/\partial z)\hat{k}$ is called the vector differential operator, ρ is the fluid density and $\mathbf{q} = u\hat{i} + v\hat{j} + w\hat{k}$ is the velocity at any point $p(x, y, z)$ of time t . In the steady motion of a gas, the term $(\partial\rho/\partial t) = 0$, then Eq. (2.34) becomes,

$$\nabla \cdot (\rho\mathbf{q}) = 0. \quad (2.35)$$

(ii). **The Equation of Motion:** The well-known Navier-Stokes equation of motion is based on the Newton's second law of motion which is described by the kinetic and dynamic effects of a viscous compressible fluid flow.

$$(\partial\mathbf{q}/\partial t) + (\mathbf{q} \cdot \nabla)\mathbf{q} = F - (\nabla p/\rho) + \nu\nabla^2\mathbf{q} + (\nu/3) \times \nabla(\nabla \cdot \mathbf{q}), \quad (2.36)$$

where, $\nu = (\mu/\rho)$, F , and p be the kinematic viscosity, external body force, and pressure at any point $p(x, y, z, t)$ respectively. Now, Eq. (2.36) becomes for the inviscid fluid,

$$\frac{\partial \mathbf{q}}{\partial t} + (\mathbf{q} \cdot \nabla) \mathbf{q} = F - \frac{\nabla p}{\rho}. \quad (2.37)$$

Equation. (2.36) is known as the Euler's equation of motion which is valid for both compressible and incompressible flows. For the compressible flows ρ is the function of both pressure and temperature while ρ is constant for the incompressible flows. In the case of steady motion of a gas which is free from body forces, then Eq. (2.36) becomes,

$$(\mathbf{q} \cdot \nabla) \mathbf{q} = -\frac{\nabla p}{\rho}. \quad (2.38)$$

(iii). The Energy Equation: The Euler's equation of motion is always integrable when the velocity potential and force potential are exists. Because velocities and external forces are derivable from the potential function. If ϕ is the velocity potential and P is the force potential, then the following pressure equation can be derived from Eq. (2.36),

$$-\frac{\partial \phi}{\partial t} + \frac{q^2}{2} + P + \int \frac{dp}{\rho} = f(t), \quad (2.39)$$

where, $\mathbf{q} = -\nabla \phi$, $F = -\nabla P$ and ρ is a function of pressure p . For the steady motion where no body forces are acting, then the Bernoulli's equation. Eq. (2.39) becomes,

$$\frac{q^2}{2} + \int \frac{dp}{\rho} = k. \quad [\text{where, } k \text{ is a constant}] \quad (2.40)$$

When flow becomes isentropic where the entropy remains constant, then Eq. (2.40) can be derived as follow by using the Eq. (2.32):

$$\frac{q^2}{2} + \frac{\gamma}{\gamma - 1} \times \frac{p}{\rho} = k, \quad (2.41)$$

where, the concepts of γ is established from the combination of first and second law of thermodynamics. The values of specific heat are varied depending on the gases.

(iv). The Equation of State: When the study is conducted with the ideal or perfect gas, then the equation of state is given by,

$$p = \rho RT, \quad (2.42)$$

using the notation R is the universal constant for a gas under consideration.

The various formation of continuity, momentum and energy equations based on the particular co-ordinates system are used in a variety of fluid models. The cylindrical and elliptical co-ordinates formations of continuity, momentum and energy equations has been established details in **Chapter 3** and **Chapter 4** separately.

2.2.14 Speed of Sound

Sound waves are infinitely small pressure disturbances which are travels through a medium in compressive and propagative ways. The speed at which small pressure vibrations (waves) propagate through a medium is known as the speed of sound. Thus, the compressible effect of the medium where sound waves propagate is crucial for measuring the speed of sound.

Using the continuity and momentum equation to a control volume of small length of observer is configured in the referenced [47] across the pressure wave where p is the pressure, ρ is the density, dV is the steady velocity and A be the cross-sectional area of piston, then the speed of sound (c) can be conveyed as:

$$c = \sqrt{dp/d\rho}, \quad (2.43)$$

where, the symbols dp and $d\rho$ are used having their usual meaning. If the process is considered under the isentropic where negligible heat interaction becomes the process reversible and adiabatic, then speed of sound can be stated as,

$$c = \sqrt{(\partial p / \partial \rho)_s} = \sqrt{\gamma p / \rho} = \sqrt{\gamma RT}. \quad (2.44)$$

For the process is conducted in an isothermal system, the velocity of sound can be derived as,

$$c = \sqrt{RT}. \quad (2.45)$$

It is clear that Eqs. (2.44) and (2.45) show the effect of change in temperature on the velocity of sound at their respective process. The speed of sound can also be expressed in terms of bulk modulus and effect of change in velocity.

2.2.15 Mach Number

In compressible flow field, there is a dynamic relation between velocity of fluid flow and the local velocity of sound. So, the ratio of the velocity of fluid (V) at a point to the local speed of sound (c) at the same point is called Mach number. In mathematical, the Mach number (M) can be defined as,

$$M = V/c. \quad (2.46)$$

In contrast, fluid contains the elastic nature, so Mach number can also be stated as the ratio of inertia forces to elastic forces which specifies that when the inertia forces or velocity of fluid becomes smaller than the elastic forces or local speed of sound, then Mach number becomes low. In that case, the variation of density is considered small, and the flow may be referred to incompressible. The following classification of compressible fluid flow has been included based on the different measures of Mach number:

(i). Subsonic flow: A flow is turned into subsonic, when the Mach number (M) is less than unity ($M < 1$), which implies that the local velocity of sound (c) is greater than the velocity of fluid (V), *i.e.* $V < c$.

(ii). Sonic flow: A flow is become sonic, when the Mach number (M) is equal to unity ($M = 1$), which indicates that the value of fluid velocity (V) is same as the rate of small-pressure disturbances (c), *i.e.* $V = c$.

(iii). Supersonic flow: A flow is said to be supersonic, when the Mach number (M) is greater than unity and less than the value of five, (*i.e.* $1 < M < 5$), which implies that the velocity of fluid (V) is greater than the local speed of sound (c), *i.e.* $V > c$.

Parallely, when Mach numbers (M) are greater than 5, then the flow is called hypersonic. Again, if the Mach numbers (M) somewhat less than unity or slightly greater than unity, approximately ($0.8 < M < 1.4$), then the flow is called transonic.

2.2.16 Geometrical Transmission of Sound Waves

Let us consider a system of continuous waves is emitted in a compressible fluid or gas from a moving particle where waves are propagated in all directions with the finite velocity of sound c . Since the Mach numbers are the measure of transmission of sound wave, then the possible flow pattern has been established by Figs. 2.3 to 2.5 where the effects of subsonic, sonic, and supersonic flow are configured. The contents are referenced from [47].

For the subsonic effect in Fig. 2.3 where a particle is moving at a constant velocity V and reached a position such as P, Q, R , and so on according at the times $0, t, 2t$, and so on. As a result, a spherical wave would be emitted by the particle. By covering the distance Vt , the disturbance particle is transmitted P to Q during the time t . In contrast, the wave is radiated up to the radius distance ct from the source position P specifying the point disturbance. So, the disturbances effects are perceived throughout the flow field, and point disturbances always drop behind the spherical waves which are generated by it. Continuous spherical waves are dense in the direction of motion and the pattern is non-symmetrical.

The sonic feature is illustrated in Fig. 2.4 where the source is moving with the same speed as the waves it produces, and a series of spheres touch each other tangentially at the point of interference representing the sound waves. At this speed, acoustic disturbances cannot convey the information and the fluid cannot pre-adapt to the approaching particles.

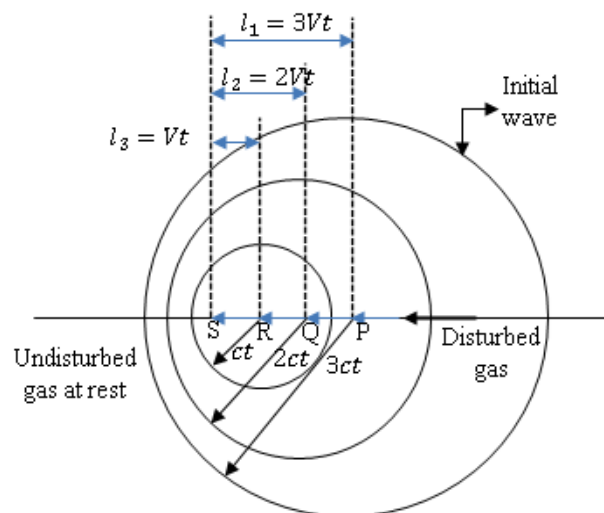


Fig. 2.3: Subsonic flow, ($V < c, M < 1$)

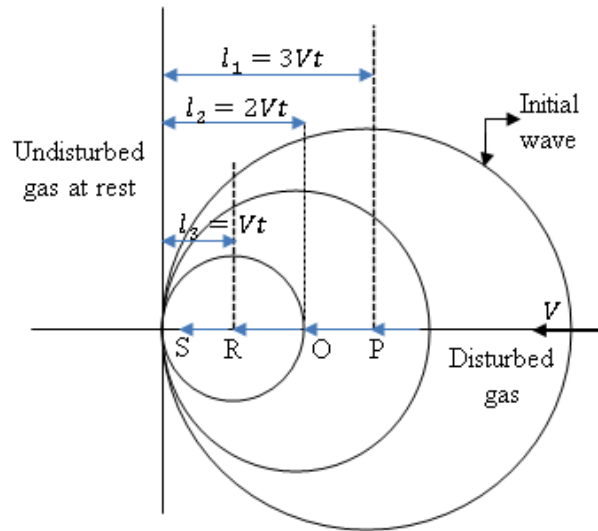


Fig. 2.4: Sonic flow, ($V = c, M = 1$)

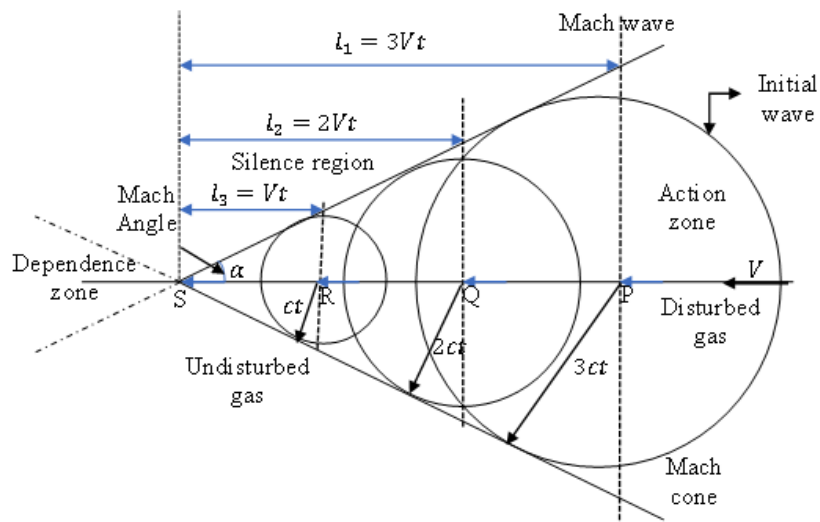


Fig. 2.5: Supersonic flow, ($V > c, M > 1$)

At the supersonic speeds, the particle moves faster than the generated waves which are enveloped in a circular cone, called the Mach cone showing in the Fig. 2.5. Whereas the Mach lines or Mach waves can be defined by the generators of the Mach cone and the coincided angle of the Mach line with the moving direction of particle can also be specified by Mach angle α . At the action zone, the disturbance effect of source point is restricted. So, it is mentionable that the disturbances cannot propagate upstream in supersonic flow. Again, the dependence zone is created by expanding the Mach lines oppositely and keeping the same measurement of the Mach cone at same apex where the pressure and velocity at the point disturbance are also affected through the inside disturbances of the Mach cone. The region outside of the

dependence zone and Mach cone is unchanged by the disturbance that is called the silence zone. Using the right triangle property on Fig. 2.5 with Eq. (2.46), Mach angle α is given by

$$\alpha = \sin^{-1}(ct/Vt) = \sin^{-1}(1/M). \quad (2.47)$$

Equation (2.47) is implemented only for supersonic flow. For sonic flow $\sin\alpha = 1$, or $\alpha = \pi/2$ and subsonic flow $\sin\alpha < 1$ or $\alpha < \pi/2$. From Eq. (2.47), it can say that the Mach angle decreases with increasing the Mach number and Mach cone also depends on the Mach number. For an example of supersonic flow, when an airplane is flying at a supersonic speed, then a viewer cannot hear the sound until it is a long way behind the viewer.

2.2.17 Reynolds Number

The classified laminar and turbulent fluid flow can be described by the concepts of dimensionless Reynolds number. The ratio of inertia forces to viscous forces is defined by the Reynolds number. The mathematical expression of Reynolds number (Re) is as follows:

$$Re = (VD/\nu) = (\rho VD/\mu). \quad (2.48)$$

Here, D is the characteristic length or diameter, ν is the kinematic viscosity, ρ is the density and V is the velocity of fluid. When the inertia forces are predominated, then Reynolds number is high, and flow becomes turbulent. Since the turbulent flow does not show simple flow structure, because of random eddies existence which causes change of momentum across the mean streamlines. The mean velocity is still required to describe this fluid flow. On the other hand, when the viscous forces are predominated, then the Reynolds number is low, and flow shows laminar structure where the adjacent layers of fluid move in an orderly way parallel to each other to the flow direction. In a circular device, the flow is laminar and parabolic when Reynolds number is below 2100, whereas it is turbulent when the Reynolds is exceeded 4000.

2.2.18 Isentropic Flow, Nozzle and Diffuser

In general, the insertion of simple flows originates the complex flow structures which are visualized through the flow of compressible fluid. Under some considerations, the flow of compressible fluid obeys the isentropic flow properties, though ideal isentropic flow is quite hard to occur. The diminished irreversible effects are occurred by the smoothness of duct's inner walls and the zero viscosity of fluid which are approaching adiabatic flow to isentropic

flow through a variational cross-sectional area of duct is shown in Fig. 2.6. In an isentropic flow which is adiabatic and frictionless, the static characteristics change depending on the cross-sectional area, but stagnation characteristics do not change.

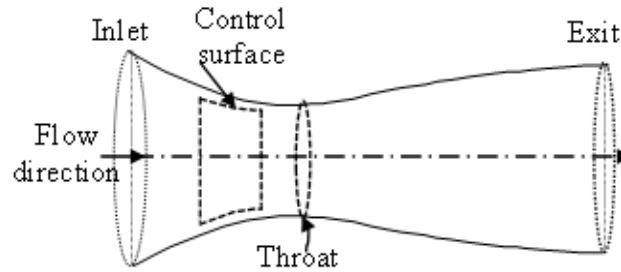


Fig. 2.6: Flow through a varying area of a nozzle.

A nozzle is a duct of short length having variable cross-sectional area for accelerating fluid from reservoir. The front part of nozzle may be **convergent** or **divergent**. The flow passage decreases to a minimum cross-section in a **convergent-divergent** nozzle or **Laval-nozzle** is known as the **throat** shown in Fig. 2.6. Because of a short length of nozzle, the flow is assumed frictionless, and no work is done along the boundary, then it is turned to isentropic flow. A nozzle is acted as a diffuser when fluid is decelerating through the cross-sectional area.

2.2.19 Isentropic Flow through a Duct

Figure 2.7 is illustrated an isentropic gas flow through a duct where the pressure (p), velocity (V), density (ρ) and temperature (T) are located at the cross-sectional area (A). Then, the continuity equation of the steady-state one-dimensional gas through a duct becomes,

$$\rho AV = K(\text{constant}). \quad (2.49)$$

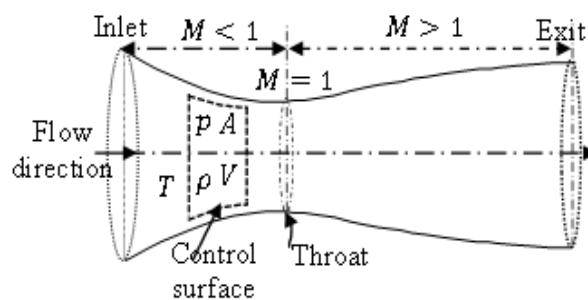


Fig. 2.7: Isentropic flow through a duct.

The differentiating form of Eq. (2.49) is,

$$(d\rho/\rho) + (dA/A) + (dV/V) = 0. \quad (2.50)$$

From the Bernoulli's equation (2.40), it can be rearranged by,

$$(1/\rho) = -V \times (dV/dp). \quad (2.51)$$

Again, using Eq. (2.43), the speed of sound can be written as,

$$c^2 = (dp/d\rho). \quad (2.52)$$

Now, combining Eqs. (2.51) and (2.52),

$$(d\rho/\rho) = (-V/c^2) \times dV. \quad (2.53)$$

From Eqs. (2.53) and (2.50),

$$(-V/c^2) \times dV + (dA/A) + (dV/V) = 0. \quad (2.54)$$

Using Eq. (2.46), then Eq. (2.54) becomes,

$$\Rightarrow dV/V = dA/[A \times (M^2 - 1)]. \quad (2.55)$$

From Eqs. (2.55) and (2.50),

$$\Rightarrow d\rho/\rho = M^2 \times dA/[A \times (M^2 - 1)]. = -M^2(dV/V). \quad (2.56)$$

Again, using Eqs. (2.56), (2.52), and (2.50),

$$\Rightarrow \frac{dp}{p} = \frac{\gamma M^2}{(1 - M^2)} \frac{dA}{A}. \quad (2.57)$$

Equations (2.55) to (2.57) represent the relative change in velocity, density, and pressure respectively according to the relative change in cross-sectional area which are also drawn in the Figs. 2.8 to 2.10 separately against the Mach number. It is clear that when $M < 1$, the ratio of all the cases is negative and velocity, density and pressure differs inversely with the cross-sectional area, whereas for $M > 1$, the ratio of all the cases is positive and velocity, density and pressure differs identically with the cross-sectional area for the gases. In Eq. (2.56) has

another relation between the relative change in density with respect to the relative change in velocity for $M > 0$ is represented by Fig. 2.11.

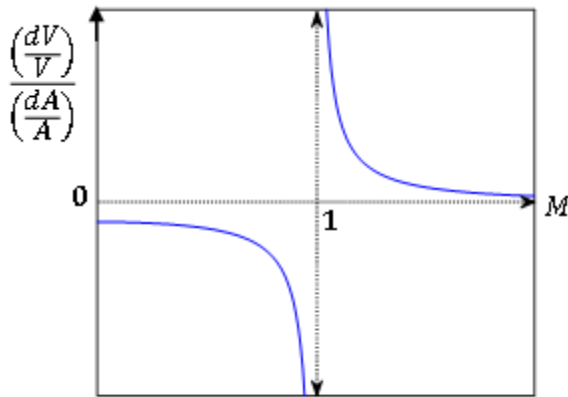


Fig. 2.8: Effect of relative velocity with cross-sectional area to Mach number

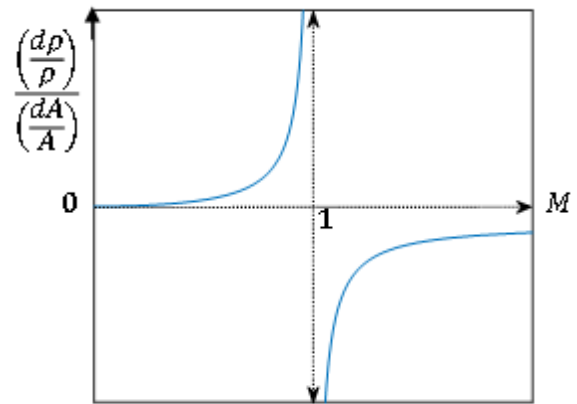


Fig. 2.9: Effect of relative density with cross-sectional area to Mach number

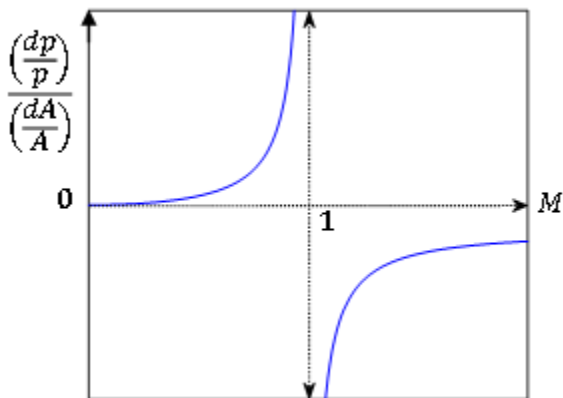


Fig. 2.10: Effect of relative pressure with cross-sectional area to Mach number

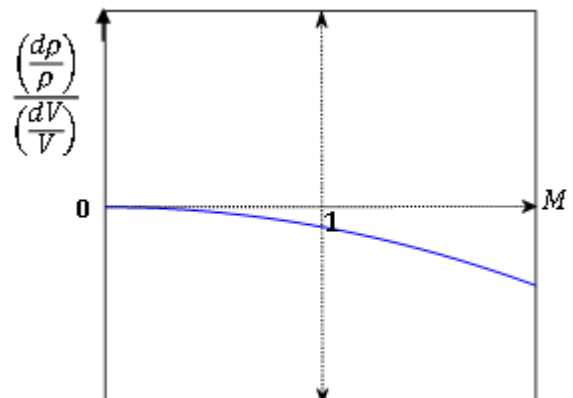


Fig. 2.11: Effect of relative density with velocity to Mach number


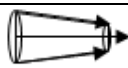
The following possible outcomes are carried out from the above discussion:

(i). The fluid acceleration or deceleration at any point depends on the cross-sectional area and the Mach number of the flow is more or less than 1 those are described by Eq. (2.55). The opposite effects on subsonic and supersonic have been occurred by the change of cross-sectional area. Now, for convergent duct, the flow becomes subsonic at $M < 1$, but it is also behaved as a supersonic diffuser at $M > 1$.

(ii). When the cross-sectional area is unchanged, *i. e.* $dA = 0$ and $M = 1$, then $dV = 0$, $d\rho = 0$, and $dp = 0$ which are evaluated from Eqs. (2.55), (2.56), and (2.57) respectively. These results implies that the constant velocity, density, and pressure are exhibited at $dA = 0$ and $M = 1$ which section is known as throat of the device. Also, the sonic velocity of isentropic flow is appeared only at the throat section, not for others.

(iii). The acceleration of subsonic flow in a nozzle cannot be done beyond the Mach number 1. On the other hand, the flow may be accelerated from subsonic to supersonic speed by connecting the convergent portion with divergent section, though it is depended on the exit pressure. That time, throat Mach number is passed the value 1 by the downstream procedure and the acceleration of flow is also occurred continuously.

(iv). And rest of the possible outputs for velocity, density, and pressure associates with Eqs. (2.55) to (2.57) listing in the Table 2.1 and depicting in Fig. 2.12 where ' + ' and ' - ' signs are used for increasing and decreasing cases respectfully.

Table 2.1							
		Mach number, $M < 1$			Mach number, $M > 1$		
$dA +$	Divergent 	$dV -$	$d\rho +$	$dp +$	$dV +$	$d\rho -$	$dp -$
$dA -$	Convergent 	$dV +$	$d\rho -$	$dp -$	$dV -$	$d\rho +$	$dp +$

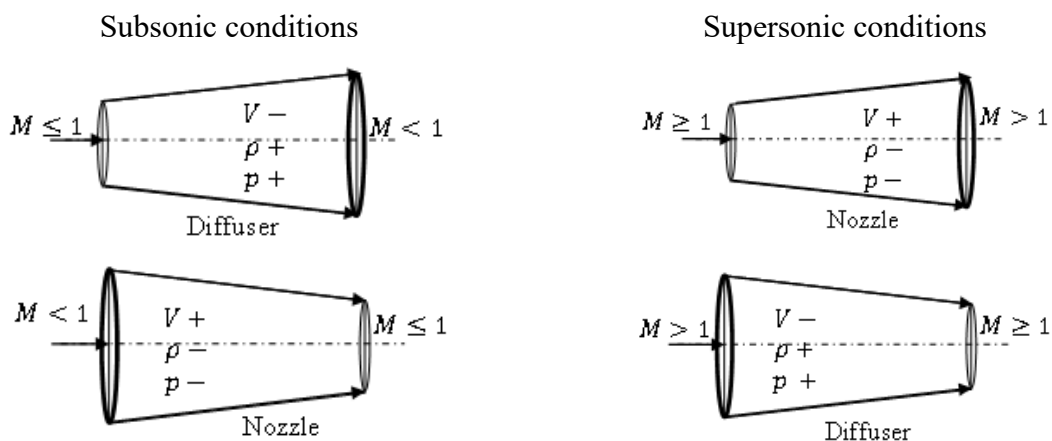


Fig. 2.12: The effect of velocity, density and pressure due to the change of area for the subsonic and supersonic flow with respect to the Mach number.

2.2.20 Isentropic Flow Relations for a Perfect Gas

In this section, the various isentropic relations of a perfect gas are constructed with keeping constant the specific heats. All the expressed relations are based on the properties of stagnation, Mach number and dimensionless.

Combining the energy equation (2.41) and the velocity of sound Eq. (2.44) for an isentropic flow of gas, it can be written as,

$$\frac{V^2}{2} + \frac{\gamma p}{\rho(\gamma - 1)} = k, \quad (2.58)$$

where, the used notations are having their usual meaning. Here, it is clear that the velocity becomes maximum $V = V_{max}$ when the speed of sound $c = 0$, then Eq. (2.58) gives,

$$k = \frac{V_{max}^2}{2}. \quad (2.59)$$

Now, at the throat position, when $V = c$, the speed of sound is called critical speed of sound and denoted by $V = c = c^*$, then the constant of Eq. (2.58) can be expressed as,

$$k = \frac{\gamma + 1}{2(\gamma - 1)} c^{*2}. \quad (2.60)$$

Considering, c_0, ρ_0, p_0 , and T_{0s} be the stagnation values of the static speed of sound (c), density (ρ), pressure (p), and temperature (T) respectively at the fluid velocity, $V = 0$. Then the constant of Eq. (2.58) can be written as follows for $c = c_0$ with Eq. (2.44).

$$k = c_0^2/(\gamma - 1) = \gamma p_0/\rho_0(\gamma - 1). \quad (2.61)$$

Using Eqs. (2.61) and (2.58), it can be written as,

$$\frac{V^2}{2} + \frac{\gamma p}{\rho(\gamma - 1)} = \frac{\gamma p_0}{\rho_0(\gamma - 1)}. \quad (2.62)$$

From Eqs. (2.20) and (2.19), it can be established that,

$$C_p = R\gamma/(\gamma - 1). \quad (2.63)$$

Again, using Eq. (2.63) with the equation of gas state $p = \rho RT$,

$$\frac{\gamma p}{\rho(\gamma - 1)} = \frac{R\gamma}{(\gamma - 1)} T = C_p T. \quad (2.64)$$

Now applying the concept of Eqs. (2.64) in (2.62), then it becomes,

$$V^2/2 + C_p T = C_p T_0. \quad (2.65)$$

$$\Rightarrow \frac{T_0}{T} = 1 + \frac{V^2}{2C_p T} = 1 + \frac{(\gamma - 1)V^2}{2 \times \gamma RT}. \quad (2.66)$$

Using Eqs. (2.44) and (2.46), it becomes,

$$T_0/T = 1 + M^2 \times (\gamma - 1)/2. \quad (2.67)$$

The ratio of the stagnation to the static speed of sound can be evaluated by,

$$c_0/c = \sqrt{(p_0/p) \times (\rho/\rho_0)}. \quad (2.68)$$

From Eq. (2.32) for isentropic flow of a perfect gas,

$$p_0/p = (\rho_0/\rho)^\gamma. \quad (2.69)$$

Using the relation (2.33) with (2.68), it is given as,

$$c_0/c = (\rho_0/\rho)^{\frac{\gamma-1}{2}} = (p_0/p)^{\frac{\gamma-1}{\gamma}}. \quad (2.70)$$

Again, the ratio of the stagnation to static speed of sound is reformed by Eq. (2.44) as,

$$\frac{c_0}{c} = \sqrt{T_0/T} = \left(1 + \frac{\gamma - 1}{2} M^2\right)^{1/2}. \quad (2.71)$$

Using Eqs. (2.71), (2.70), and (2.67), the following relation are obtained by,

$$\frac{\rho_0}{\rho} = \left(\frac{T_0}{T}\right)^{\frac{1}{\gamma-1}} = \left(1 + \frac{\gamma - 1}{2} M^2\right)^{\frac{1}{\gamma-1}}. \quad (2.72)$$

$$\frac{p_0}{p} = \left(\frac{T_0}{T}\right)^{\frac{\gamma}{\gamma-1}} = \left(1 + \frac{\gamma-1}{2} M^2\right)^{\frac{\gamma}{\gamma-1}}. \quad (2.73)$$

If the mass flow rate per unit area (A) is called mass flux G , then it can be defined as,

$$G = \dot{m}/A = \rho V. \quad (2.74)$$

Using the equation of gas state and Eq. (2.44), then the Eq. (2.73) becomes,

$$G = \dot{m}/A = p(V/c) \times \sqrt{\gamma/RT}. \quad (2.75)$$

Substituting the values of T and p from Eqs. (2.67) and (2.73) in Eq. (2.75), then mass flux can be written as,

$$G = \frac{\dot{m}}{A} = \frac{p_0}{\sqrt{T_0}} \sqrt{\frac{\gamma}{R}} \times \left[\frac{M}{\left(1 + \frac{\gamma-1}{2} M^2\right)^{\frac{\gamma+1}{2(\gamma-1)}}} \right]. \quad (2.76)$$

Using the critical condition, the mass flow rate G is maximum when $M = 1$ at the throat section where area is minimum, then Eq. (2.76) becomes,

$$G^* = \dot{m}/A^* = (p_0/\sqrt{T_0}) \sqrt{(\gamma/R) \times (2/\gamma + 1)^{\frac{\gamma+1}{\gamma-1}}}. \quad (2.77)$$

Now the following cross-sectional area ratio can be expressed in terms of γ and the Mach number by using Eqs. (2.76) and (2.77),

$$\frac{A}{A^*} = \frac{G^*}{G} = \frac{1}{M} \left[\frac{2}{\gamma+1} \times \left(1 + \frac{\gamma-1}{2} M^2\right) \right]^{\frac{\gamma+1}{2(\gamma-1)}}. \quad (2.78)$$

It is mentionable that the value of the ratio of cross-sectional area $\frac{A}{A^*}$ is never less than unity, and the minimum value of unity is occurred by Eq. (2.77) at $M = 1$ which is included from the reference [47].

2.2.21 Characterizes of a Perfect Gas through a Nozzle

When a high-speed gas issues from a nozzle, then the compressibility characteristics affect the flow of gas. Usually, the cross-sectional area of the nozzle is one of the reasons for showing such characteristics. The study in this section constructs with such issued gas which is conducting through a convergent nozzle or convergent-divergent nozzle and then the nozzle exits pressure, and the ambient pressure makes the difference to evaluate the flow variables.

(i). Flow through a Convergent Nozzle: In this case, the initial pressure of a gas and the ratio of the total pressure of the gas to the ambient pressure are the key factors to measure the possible encountered situations. In Fig. 2.13 (B), the expected flow schemes have been drawn to evaluate the several scales of pressure into the nozzle (Fig. 2.13 (A)) due to the nozzle axial distance (z). The related mass flow and exit pressure evaluations are also depicted in Fig. 2.13 (C) and Fig. 2.13 (D) separately. All the potential effects are listed in below:

- ❖ The first scheme due to the subsonic flow is characterized with the case *a to c* in Fig. 2.13 (B) where the nozzle exit pressure (p_e) is equal to the ambient or back pressure (p_b) and the mass flow (\dot{m}) is increased with respect to the stagnation pressure (p_0).
- ❖ Second one is stated with the critical condition where the sonic flow is characterized by the case *d* in Fig. 2.13 (B) and the nozzle is said to choked. At this stage, the nozzle exit pressure (p_e) is equal to the critical pressure (p^*) and the mass flow is become maximum (\dot{m}_{max}) which is shown in Fig. 2.13 (C). It is noted that the overall conditions are considered for measuring the flow properties, but the assumption would be different for the presence of boundary layer.
- ❖ Finally, almost similar behavior has been appeared inside the nozzle upon all the flow quantities demarcating in case *e* of Fig. 2.13 (B) yet the exit pressure is higher than the back pressure. Then, an under-expansion wave has been created under this circumstance and the pressure stability is also happened into the ambient.

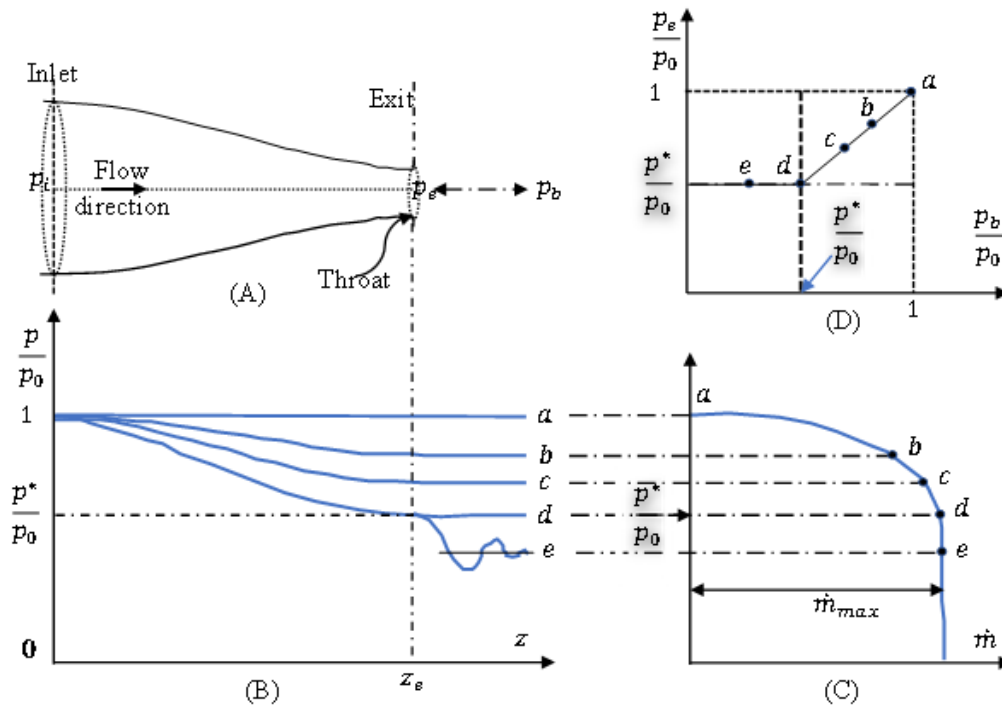


Fig. 2.13: Evaluation of the flow quantities of perfect gas through (A) convergent nozzle for various pressure ratios: (B) pressure, (C) mass flow, and (D) exit pressure.

(ii). **Flow through a Convergent-Divergent Nozzle:** An analogue schematic flow of a perfect gas under this circumstance has been illustrated with Fig. 2.14 where the evaluation of pressure (Fig. 2.14 (B)), Mach number (Fig. 2.14 (C)), mass flow (Fig. 2.14 (D)) and exit pressure (Fig. 2.14 (E)) are also described. In the following section, the potential effects of flow quantities are considered according to case wise:

- ❖ The case b in Fig. 2.14 (B) is indicating the subsonic feature where the nozzle exit pressure (p_e) same as the ambient pressure (p_b) and the mass flow is evaluated with respect to the ratio between back pressure (p_b) to stagnation pressure (p_0).
- ❖ The sonic flow is attained at the throat where the Mach number (M) is equal to 1 and the choked flow is stated by the case c in Fig. 2.14 (B). Then the mass flow can also be measured by the stagnation conditions.
- ❖ The exit pressure will be differed from the ambient pressure, until attending the design operating conditions marked as case d . The under-expansion feature is appeared when the ratio (p_0/p_b) is greater than the ratio (p_0/p^*). The references [3, 47] are recommended for the details understanding of such flow feature.

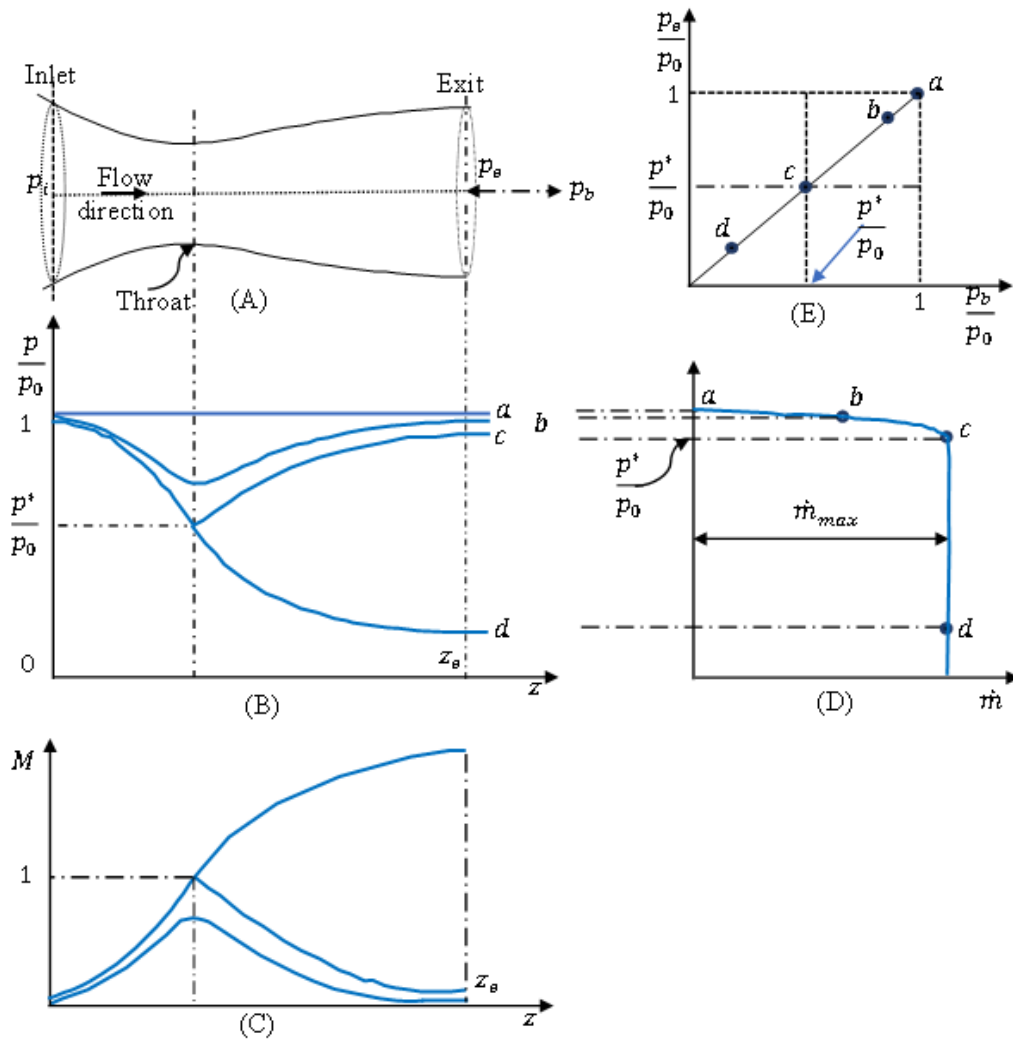


Fig. 2.14: Evaluation of the flow quantities in (A) convergent-divergent nozzle for several pressure ratios: (B) pressure, (C) Mach number, (D) mass flow, (E) exit pressure.

2.2.22 Shock Waves

An intense disturbances or variations in pressure exit across the infinitesimal pressure waves, causing discontinuous and irreversible changes in the fluid properties such as velocity, temperature, pressure, and density which switch from supersonic to subsonic. These are called **shock waves**. In Fig. 2.15 is a rainbow schlieren picture of inviscid nonconducting gas flow where the thin layers or surfaces of gas are indicating as the **shock waves** with the order of finite thickness ($\approx 10^2 \text{ nm}$) [47]. It is noted that the changing properties of the real fluid (such as viscosity, heat conductivity and diffusivity) may affect the thickness of the duct shock.

Consequently, when the flow is extended to isentropic for a sufficiently large change in pressure with an increase in entropy, the wave is called **expansion waves**. In Fig. 2.15, the

focused expansion waves are created on the lip of nozzle exit which propagate to the opposite side of the jet and reflect the free jet layer called **jet boundary** as a **compression wave**. Before attaining the middle of the jet, these converge to the **incident shock waves**, resulting in the mac reflections with the corresponding **Mach discs**, **reflective waves**, and **shear layers** concepts are implemented from [43].

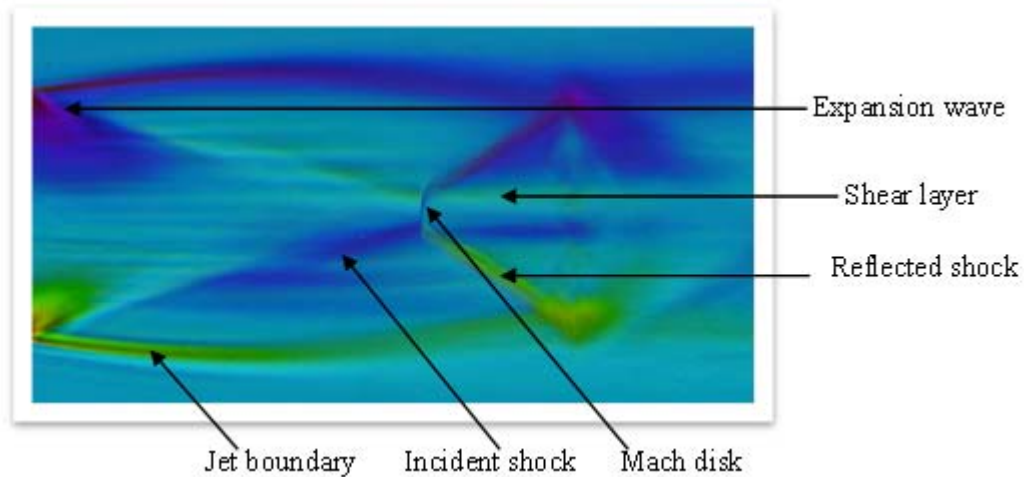


Fig. 2.15: Rainbow Schlieren picture of shock waves.

There are two types of shock waves: normal or one-dimensional shock waves and oblique or multidimensional shock waves are usually observed through the following definitions.

(i). Normal shock waves: If the change of fluid properties in a shock wave occurs to the same direction of the fluid flow, then the shock wave is called one-dimensional or normal shock wave. In a normal shock wave where shock wave is perpendicular to the incoming flow, as stated in Fig. 2.16 through the reference [49].

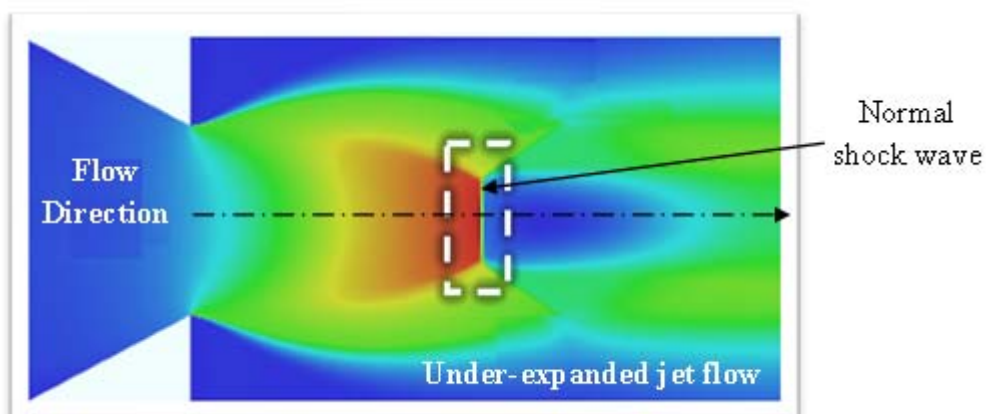


Fig. 2.16: A picture of normal shock wave [49].

(ii). Oblique shock waves: If the change in the fluid properties of the shock wave ρ, M^2 form over supersonically traveling objects occurs in a direction that does not coincide with the overall direction of the flow, then the shock wave is called multidimensional or oblique shock wave. In an oblique shock wave where shock wave is inclined at an angle to the incoming flow. As a concern, the formation of a bow/detached shock wave depends on the structure of the objects which is separated from the object as defined in Fig. 2.17 with the oblique shock wave through the reference [49].

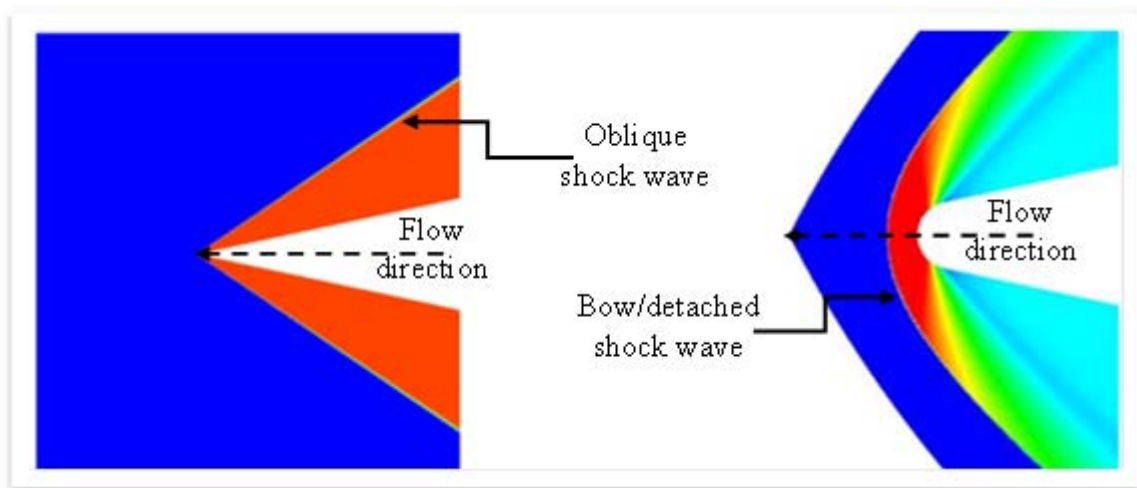


Fig. 2.17: A picture of visualizing oblique and detached shock wave.

The studies in this chapter along with the fundamental concepts of compressible fluid and their flow behavior has been summarized for the overall reflection of work and for the betterment of Chapter 3 and Chapter 4. The characteristics of various nozzles behavior are helpful to construct the governing equations which are followed by the kinematic and dynamic boundary conditions. Newton's law of viscosity, first and second law of thermodynamics and their related topics are discussed to understand the compressible fluid flow. Mach number and Reynold number are the vital subjects to analyze and classify the high-speed jet flow. With the presence of turbulence and molecular viscosity, the compressibility effects of fluid why and how create the complex phenomena into the flow filed has been discussed for the comprehensive observation and finding some information which haven't established yet in the domain of research.

Chapter 3

Shock Containing Circular Jet

3.1 Introduction

To understanding the prominent characteristics of complex shock-containing circular jet, schlieren and shadowgraph methods [21] have been widely used as optical tools because of its simple optical arrangement with a higher degree of resolution and ability to easily observe such shock wave structures, Prandtl-Meyer compression, and expansion waves in supersonic flows. The techniques of conventional schlieren are more applicable for some scientists to analyze the jet flow, but recently laser-based interferometry such as Twyman-Green interferometry [22], Mach-Zehnder interferometry [23, 24] or rainbow schlieren deflectometry [26~32] methods are becoming much more useful for visualizing jet density fields quantitatively. The rainbow schlieren deflectometry (RSD) would presumably be the simplest optical technique to acquire the density fields of underexpanded supersonic jets quantitatively. For getting the information of vector and scalar quantities in the flow field, the microscale devices are required in all the optical methods. Though few, some qualitative information about shock-containing jets from the convergent-divergent circular nozzle are known in the current literature because of technical difficulties in measurements. Although Franquet et al. [3] provided a comprehensive review on axisymmetric supersonic jets issued from convergent or convergent-divergent nozzle, covering papers experimentally dealing with underexpanded jets, the structure, and dynamical properties of axisymmetric underexpanded jets are still known only qualitatively, and there is little quantitative information on the dynamics of microjets.

In this chapter, at first the rainbow schlieren deflectometry is applied for jets from a round Laval nozzle followed by a cylindrical duct for the experimental investigation. Such a Laval nozzle followed by a long duct attracts special attentions on applications for the cold spray technology [50, 51], which includes a deposition process in which small particles in the solid state accelerate to high velocities in a supersonic gas jet and deposit on the substrate material. It has been widely recognized that the quality of the coating depends significantly on the gas flow velocity and stagnation temperature. The higher gas velocity makes the particle velocity increased, resulting in highly tough and dense coatings on a solid surface. To achieve optimal conditions for deposition, the quantitative information of the supersonic jets is required. However, there are little quantitative experimental data about the gas dynamics of the cold spray technology. In addition, the design of the spray gun has been primarily empirical and based upon engineering intuition. Therefore, as a first step of an application for the cold spray technology, the effects of nozzle pressure ratios on flow features of the jet from a supersonic nozzle followed by a long duct are described here. Furthermore, the previous experimental data [29] on a jet issued from a conventional Laval nozzle is used for a comparison with the present RSD data where a long duct is used. A peer reviewed journal paper has been published with this sectional analysis that is available in the references [15].

Secondly, the issued supersonic jet from an axisymmetric convergent-divergent nozzle has been solved analytically by a modified model where the concepts are gathered from the two flow models [16,18]. Former one was proposed by Tam [16] where the thin layer of the jets compared as a vortex sheet, second one was established by Emami et al. [18] where the mean Reynolds stress took into their account. In the present model, the concepts of continuity and momentum equations has been derived by extending the Navier-Stokes equations where the turbulent viscous effects are measured moderately by using the Witz's [19] formula for the fully expanded jet, whereas the turbulent viscous effects in the model [18] was studied for the nozzle exit level. On the other hand, the involvement of modified turbulent viscosity is the contrast of the present modified model and Tam's [16] with Emami's [18] model, but the similarity of present and Tam's [16] models is that those have been analyzed by the fully expanded jet. consequently, the proposed model is completed through the formation of the isentropic equation where the fully expanded speed of sound is specified in the Bernoulli's equation of energy. This expended speed of sound concept isolates the present model from the theory [18], nevertheless, the similar change of perturbed pressure gradient at nozzle exit is deemed in these two models. Whereas, in Tam's model [16], the change of velocity gradient at

the nozzle exit for the inviscid supersonic jet is considered. Two explicit analytical solutions have been come out separately by using the cylindrical transformation due to the circular cross-section at the nozzle exit. The first case of solution is determined for the inviscid jet which is the similar as Tam's model [16] known as vortex sheet model, and second case of solution is modified one which is varied with the Emami et al. [18] model by the flow characteristics of fully expanded jet. The first mode of eigenvalues expansion has been considered to find the complete solutions where arbitrary nozzle pressure ratios and design Mach numbers are depends on the nozzle exit cross-sectional area. The centerline density profile and density contour plots, mesh density contours of shock-cell structures have been calculated separately through these two modified explicit solutions. Finally, the enhanced modified results are also compared with the reliable circular data of RSD experiment [52], original Emami et al. [18] and Tam's [16] model to measure the accuracy of the modified model. One peer reviewed journal and two international conference proceedings have been published with these results which are cited by [15, 52, 53] in the references section.

3.2 Cylindrical Co-ordinates System

The cylindrical coordinate system is an effective three-dimensional coordinate system. Sometimes it is known as cylindrical polar coordinates system. Figure 3.1 is illustrated by the cylindrical co-ordinate system where is showing a transformation between Cartesian and Polar co-ordinates system. The origin of the system is that three coordinates can be specified as O which is the intersecting point of reference plane and the axis. The axis is variously referred to as a cylindrical axis (Z) and the other sides (X, Y) perpendicular to the cylindrical axis (Z) are called the radial lines. The distance from the cylindrical axis is called the radial distance or radius (r), and the angular coordinates (θ) are called the angular position or azimuth. The radius and azimuth are collectively called polar coordinates. This is because it matches the two-dimensional polar system in the plane that passes through the parallel points of the reference plane. If the reference plane is considered horizontal, then third coordinate is called the axial distance (z).

Considering $p(r, \theta, z)$ be any point in a reference plane where r, θ , and z are specified with their usual meaning, then the following relation can be derived,

$$x = r\cos(\theta), y = r\sin(\theta), z = z, \quad (3.1)$$

$$\text{where, } r \geq 0, 0 \leq \theta \leq 2\pi \text{ and } -\infty < z < \infty \quad (3.2)$$

Expressing the cylindrical co-ordinates r, θ, z in terms of Cartesian co-ordinates x, y, z yield,

$$r = \sqrt{x^2 + y^2}, \theta = \tan^{-1}\left(\frac{y}{x}\right) \text{ and } z = z. \quad (3.3)$$

Again, if \vec{R} be a position vector of the point $p(x, y, z)$, then it can be expressed as,

$$\vec{R} = x\hat{i} + y\hat{j} + z\hat{k}. \quad (3.4)$$

$$\vec{R} = r\cos(\theta)\hat{i} + r\sin(\theta)\hat{j} + z\hat{k}. \quad (3.5)$$

Then the vector differential operator $\bar{\nabla}$ can also be written as,

$$\text{In Cartesian form, } \bar{\nabla} = \frac{\partial}{\partial x}\hat{i} + \frac{\partial}{\partial y}\hat{j} + \frac{\partial}{\partial z}\hat{k}. \quad (3.6)$$

$$\text{In cylindrical form, } \bar{\nabla} = \frac{\partial}{\partial r}\hat{i} + \left(\frac{1}{r}\right)\frac{\partial}{\partial \theta}\hat{j} + \frac{\partial}{\partial z}\hat{k}. \quad (3.7)$$

By using the vector differential calculus, the Laplacian of vector differential operator in Cartesian to cylindrical form can be derived as,

$$\text{In cartesian form, } \nabla^2 = \frac{\partial^2}{\partial x^2} + \frac{\partial^2}{\partial y^2} + \frac{\partial^2}{\partial z^2}. \quad (3.8)$$

$$\text{In cylindrical form, } \nabla^2 = \frac{\partial^2}{\partial r^2} + \left(\frac{1}{r}\right)\frac{\partial}{\partial r} + \left(\frac{1}{r^2}\right)\frac{\partial^2}{\partial \theta^2} + \frac{\partial^2}{\partial z^2}. \quad (3.9)$$

On the other hand, the elementary arc-length in cylindrical co-ordinates can be written as,

$$ds^2 = (dr)^2 + (rd\theta)^2 + (dz)^2. \quad (3.10)$$

The usages of cylindrical coordinates [54] are related with several rotating symmetric objects and phenomena centered on the axial direction (cylindrical axis), such as the flow of fluid through a duct or pipe with a circular cross section, the distribution of heat in a metal cylinder, the electromagnetic field generated by an electric current, straight wire, accretion disks in astronomy, and so on.

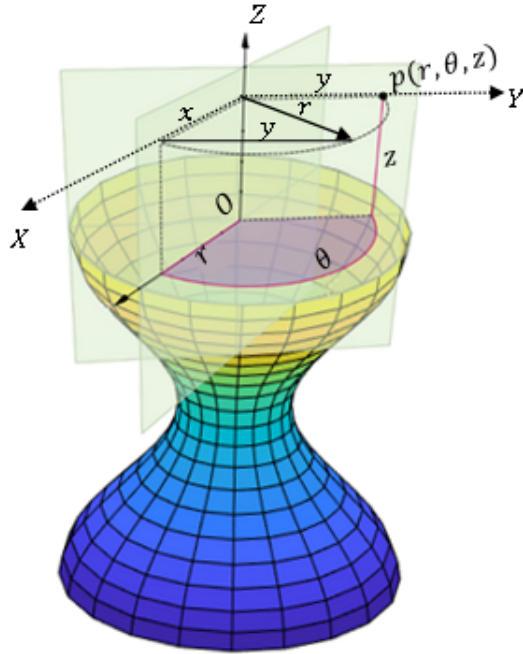


Fig. 3.1: Cylindrical Co-ordinates System

3.3 Experimental Apparatus and Method

A schematic drawing of experimental apparatus with a rainbow schlieren system is shown in Fig. 3.2. A blowdown wind tunnel with a high-pressure tank ($2m^3$) was used to provide the air flow to a cylindrical plenum chamber connected to a test nozzle. The high-pressure dry air from the tank is stagnated in the plenum chamber and then discharged into the atmosphere through the test nozzle. The total temperature in the plenum chamber was equal to the room temperature, and the plenum pressure was controlled and maintained constant during the testing by a valve. The test nozzle is shown schematically in Fig. 3.3. It is made of acrylic and consists of a round Laval nozzle with a design Mach number of 1.5 followed by a constant-area straight duct with an inner diameter of 10 mm and a length of 50 mm. The wall contour of the Laval nozzle has a sinusoidal curve over a range of parts A to B and the contour between the throat (part B) and exit (part C) is designed by the axisymmetric method of characteristics [55] to provide uniform and parallel flow in the nozzle exit plane at the design condition.

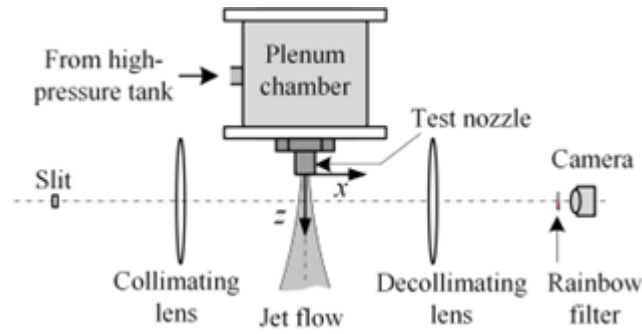
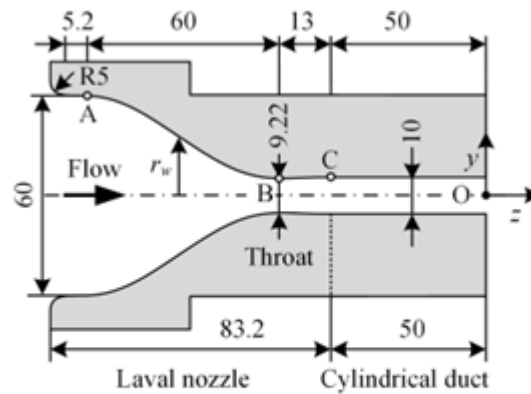


Fig. 3.2: Schematic drawing of experimental apparatus with rainbow schlieren system.



Dimensions in mm

$$\text{Part A to B: } r_w = 12.7 \sin \left[\frac{\pi}{60} (z_w + 33) \right] + 17.31$$

Part B to C: Axisymmetric method of characteristics

Fig. 3.3: Test nozzle with dimensions in mm.

The jet issued from the nozzle was visualized by the rainbow schlieren deflectometry over a range of nozzle pressure ratios ($NPR = p_{os}/p_b$) from 2.0 to 4.5 where p_{os} is the plenum pressure and p_b the back pressure ($= 101.8 \text{ kPa}$) or atmospheric pressure, and $T_b (= 295.5 \text{ K})$ the ambient temperature.

The rainbow schlieren system consists of rail-mounted optical components including a continuous 250 W metal halide light source with a $3 \text{ mm} \times 50 \text{ }\mu\text{m}$ rectangular slit, collimating and decollimating lenses with a 100 mm diameter and 500 mm focal length, a rainbow filter, and a digital camera (Nikon D7100) with a 30 mm diameter focusing lens of 600 mm focal length. Figure 3.4 (a) shows a rainbow filter used in the present experiment and the corresponding calibration curve is displayed in Fig. 3.4 (b). The rainbow filter was fabricated in computer software and then printed digitally on a high-resolution 35 mm color film recorder. It has continuous hue variation from $Hue = 0$ to 360 deg in a 2.0 mm wide strip, and the background hue is $Hue = 192 \text{ deg}$ in the present experiment. The

characteristics of the rainbow filter were performed by traversing the rainbow filter in intervals of $20 \mu\text{m}$ to the vertical (y) direction at the schlieren cutoff plane before starting experiment.

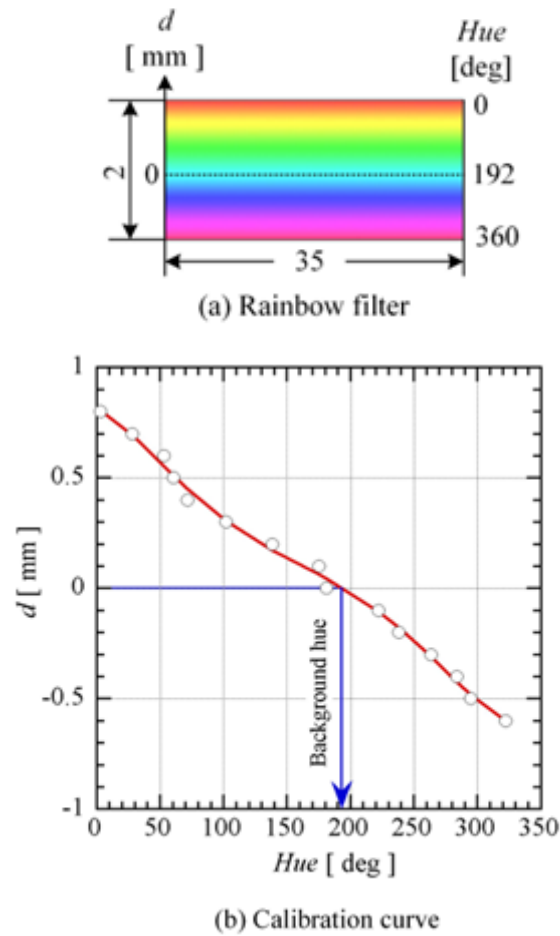


Fig 3.4: Rainbow filter with calibration curve.

The rays from the rectangular light source paralleled by the collimating lens traverse a transparent, refracting schlieren test area and are refocused by the decollimating lens to form an inverted image of the light source at the schlieren cutoff plane where the rainbow filter is placed. In rainbow schlieren systems, when a collimated light ray is deflected through the test area, a color image of the area revealing the ray deflections is formed on a recording medium of the digital camera. The schlieren image of the test area is digitized to obtain a direct quantification of the light deflections using the calibration curve of the rainbow filter. The camera output in the RGB format was digitized by a computer with 24-bit color frame grabber.

In the present experiments, multiple viewing rainbow schlieren pictures were acquired over a range of nozzle angular angles from 0 deg to 180 deg by rotating the nozzle about its longitudinal axis (z axis) in equal angular intervals of 10 deg . These 19 schlieren pictures were

used for reconstruction of the jet density field. The detailed description for the reconstruction process is given in Awata et al. [56]. The jet three-dimensional density field was reconstructed using both Abel inversion method based upon the assumption of axisymmetric jets and the convolution back-projection (CBP) method. However, only those obtained from the CBP method are demonstrated in the present studies because the density fields obtained by the Abel inversion method produced some noises on the jet centerline. The principle of the rainbow schlieren deflectometry combined with the CBP method is also given by [28, 29].

3.4. Modified Model of Circular Jet

In an off-design setup, a slightly moderated supersonic jet issued from a convergent-divergent nozzle shown in Fig. 3.5 which is free from outside disturbance and considering the mean Reynolds number for the eddy viscosity. In this model, the jet has flowed through the axial direction (z) and (r) is the radial distance from the cylindrical axis where mixing thin layer of jet treated as a vortex sheet surface established by Tam's [16]. Also, the emerged vortex surfaces are constructed in Cartesian shape for the fully developed jets. As a result, the shock-cell structures are also narrowed to the inside of the vortex sheet. Since the perturbation methods are required in the motion of fluid, so the velocity (V), pressure (p) and density (ρ) can be stated as the sum of mean quantities with perturbed quantities entire the flow field:

$$V_i = \bar{V}_i + dV_i, \bar{V}_z = U_j, \bar{V}_x = \bar{V}_y = 0, p = p_j + dp \text{ and } \rho = \rho_j + d\rho, \quad (3.11)$$

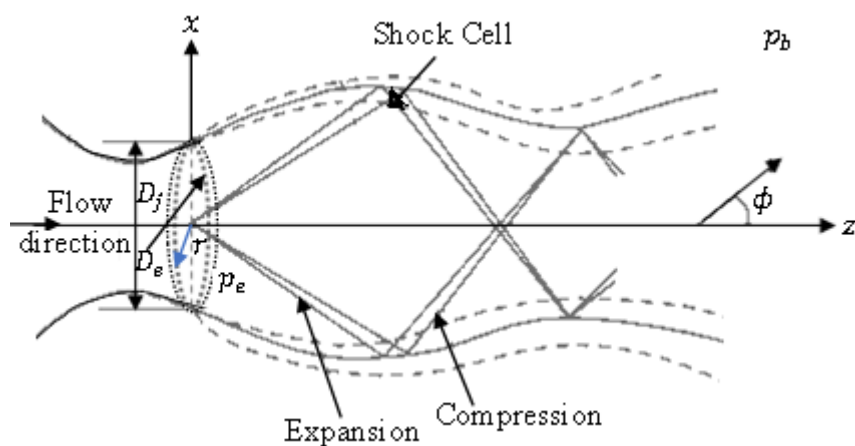


Fig 3.5: Schematic diagram of the decaying shock-cell structures of underexpanded jet from convergent-divergent circular nozzle.

where, the notations dV_i, dp , and $d\rho$ are accustomed to perturbation associated velocity, pressure, and density in the shock-cell structures. Consequently, \bar{V}_i is indicating the mean value of velocities where suffix (i) bearing the x, y, z axes. The fully expanded density, pressure, and velocity are labelled by the notation $\rho_j, p_j,$ and U_j respectively. Therefore, the perturbation relations (3.11) are applied to extend the Navier-Stokes equation through the Eqs. (2.35), (2.37), and (2.43) for the following equations of motion which are associated with Emami et al. [18] model where the exit results were compared only for the inviscid fluid.

$$\text{The equation of continuity, } \rho_j \frac{\partial dV_i}{\partial x_i} + U_j \frac{\partial d\rho}{\partial z} = 0, \quad (3.12)$$

$$\text{The momentum equation, } \rho_j U_j \frac{\partial dV_i}{\partial z} + \frac{\partial dp}{\partial x_i} + \frac{4\mu_t U_j}{3\rho_j} \frac{\partial}{\partial x_i} \left(\frac{\partial d\rho}{\partial z} \right) = 0, \quad (3.13)$$

$$\text{The isentropic equation, } \frac{dp}{d\rho} = a_j^2, \quad (3.14)$$

where, $(\partial/\partial x_i)$ and a_j represent the vector differential operator and expended speed of sound respectively. In Eq. (3.13), the turbulent viscosity (μ_t) is measured from the following formula, which is modified by the fully developed characteristics, because the eddy viscosity remains almost constant over the flow field of jet, based on this theme the original formula [19] was explored by the exit characteristics where the value of η was 0.01:

$$\mu_t = \eta \rho_b^{0.28} \rho_j^{0.72} U_j D_j (1 - 0.16M_j). \quad (3.15)$$

In Eq. (3.15), the notation η is using for the best data fitting with the RSD experimental data. According to the Tam's [16] model, the following homogeneous Eqs. (3.16) to (3.19) based on the kinematic and dynamic boundary conditions which are required for the governing Eqs. (3.12) to (3.14) where the nozzle exit pressure (p_e) is greater than ambient pressure (p_b):

$$dp(z, r = 0) = 0, \quad (3.16)$$

$$\frac{\partial(dp)}{\partial z}(z = 0, r) = 0, \quad (3.17)$$

$$dp\left(z = 0, r \in \left[\frac{D_e}{2}, \frac{D_j}{2}\right]\right) = 0, \quad (3.18)$$

$$dp\left[z = 0, r \in \left(0, \frac{D_e}{2}\right)\right] = \Delta p = p_e - p_b, \quad (3.19)$$

here, the symbols D_e and D_j are used for the nozzle exit diameter and expanded diameter of jet respectively. The condition (3.16) is applied for the nozzle exit region to appear the shock-cell structures, because of variation of pressure. Also, the perturbed pressure is zero at the center and jet exit boundary to expanded boundary with out side which are expressed by Eqs. (3.18) and (3.17) separately. The pressure gradient is also zero shown at the nozzle exit by Eq. (3.19).

Using Eq. (3.14) in Eqs. (3.12) and (3.13), then the followings are found:

$$\rho_j U_j \frac{\partial dV_i}{\partial x_i} + M_j^2 \frac{\partial dp}{\partial z} = 0, \quad (3.20)$$

$$\rho_j U_j \frac{\partial dV_i}{\partial z} + \frac{\partial dp}{\partial x_i} + \frac{4 \mu_t U_j}{3 \rho_j a_j^2} \frac{\partial}{\partial x_i} \left(\frac{\partial dp}{\partial z} \right) = 0, \quad (3.21)$$

$$\text{where, } M_j = \frac{U_j}{a_j}, \quad (3.22)$$

here, M_j is called the fully expanded jet Mach number. Now differentiating Eqs. (3.21) and (3.20) with respect to x_i and z respectively, then the followings are derived as,

$$\rho_j U_j \frac{\partial^2 dV_i}{\partial z \partial x_i} + \frac{\partial^2 dp}{\partial x_i^2} + \frac{4 \mu_t U_j}{3 \rho_j a_j^2} \frac{\partial^2}{\partial x_i^2} \left(\frac{\partial dp}{\partial z} \right) = 0 \quad (3.23)$$

$$\rho_j U_j \frac{\partial^2 dV_i}{\partial x_i \partial z} + M_j^2 \frac{\partial^2 dp}{\partial z^2} = 0. \quad (3.24)$$

By subtracting Eq. (3.23) to (3.24), the required pressure differential equation is become as,

$$\frac{\partial^2 dp}{\partial x_i^2} + \alpha \frac{\partial^2}{\partial x_i^2} \left(\frac{\partial dp}{\partial z} \right) - M_j^2 \frac{\partial^2 dp}{\partial z^2} = 0, \quad (3.25)$$

$$\text{where, } \alpha = \frac{4 \mu_t U_j}{3 \rho_j a_j^2}. \quad (3.26)$$

Using Eq. (3.9) into Eq. (3.25) for the transforming the Laplacian operator Cartesian to cylindrical form, because of the nozzle exit is circular cross-section, then it is found as,

$$\frac{\partial^2 dp}{\partial r^2} + \frac{1}{r} \frac{\partial dp}{\partial r} + \frac{\partial^2 dp}{\partial z^2} + \alpha \left(\frac{\partial^3 dp}{\partial r^2 \partial z} + \frac{1}{r} \frac{\partial^2 dp}{\partial r \partial z} + \frac{\partial^3 dp}{\partial z^3} \right) - M_j^2 \frac{\partial^2 dp}{\partial z^2} = 0.$$

$$\therefore \alpha \left(\frac{\partial^3 dp}{\partial z^3} + \frac{\partial^3 dp}{\partial r^2 \partial z} + \frac{1}{r} \frac{\partial^2 dp}{\partial r \partial z} \right) + (1 - M_j^2) \frac{\partial^2 dp}{\partial z^2} + \frac{\partial^2 dp}{\partial r^2} + \frac{1}{r} \frac{\partial dp}{\partial r} = 0. \quad (3.27)$$

Thus, Eq. (3.27) is called the perturbation pressure partial differential equation for the circular underexpanded jet. A method of separation of variables for the eigenfunction expansion is applied on Eq. (3.27) to find the explicit solution of the required linearized model. Thus, the perturbed pressure $dp(r, z)$ can be considered as,

$$dp(r, z) = R(r) \times Z(z). \quad (3.28)$$

By utilizing Eqs. (3.27) and (3.28), the following form is obtained,

$$\frac{R'' + R'/r}{R} = \frac{-\alpha Z'''(z) + (M_j^2 - 1)Z''(z)}{\alpha Z'(z) + Z(z)} = -\lambda^2, \quad (3.29)$$

where, λ is the eigen value, and the negative sign indicates that the shock-cells are decaying downstream wise with increasing the distance along the flow direction from the nozzle exit. Using the first and third part of Eq. (3.29), then it is given as,

$$r^2 R''(r) + rR'(r) + [(r\lambda)^2 - 0]R(r) = 0, \quad (3.30)$$

Equation (3.30) is a Bessel's differential equation of zeroth order, then the following general solution is obtained by using the series solution technique of ordinary differential equations:

$$R(r) = C_1 J_0(\lambda r) + C_2 Y_0(\lambda r), \quad (3.31)$$

$$\text{where, } J_0(\lambda r) = 1 + \sum_{n=1}^{\infty} \frac{(-1)^n}{n!} \times \left(\frac{\lambda r}{2} \right)^{2n}; \quad (3.32)$$

$$\text{and, } Y_0(\lambda r) = \frac{2}{\pi} \left[E_M + \ln \left(\frac{\lambda r}{2} \right) \right] J_0(\lambda r) + \sum_{n=1}^{\infty} \frac{(-1)^{n+1} H_n}{(n!)^2} \left(\frac{\lambda r}{2} \right)^{2n}, \quad (3.33)$$

where, $J_0(\lambda r)$ and $Y_0(\lambda r)$ are the Bessel's function of first kind and second kind respectively, and C_1, C_2 are also constants. In Eq. (3.33), E_M is called the Euler Masecheroni constant that approximate value is evaluated by.

$$E_M \approx \lim_{n \rightarrow \infty} [H_n - \ln(n)] \cong 0.5772 \quad (3.34)$$

$$\text{where, } H_n = \sum_{n=1}^{\infty} \left(\frac{1}{n}\right). \quad (3.35)$$

Again, by using the last two terms of Eq. (3.29), the following form is obtained:

$$\frac{-\alpha Z'''(z) + (M_j^2 - 1)Z''(z)}{\alpha Z'(z) + Z(z)} = -\lambda^2, \quad (3.36)$$

$$\therefore -\alpha Z'''(z) + (M_j^2 - 1)Z''(z) + \lambda^2[\alpha Z'(z) + Z(z)] = 0. \quad (3.37)$$

Eq. (3.37) is ordinary differential equation where the term α depends on the turbulent viscosity (μ_t) that play an important rule on flow model. There are two possible cases have been raised for the $\mu_t = 0$ and $\mu_t \neq 0$ which are described as follows:

Case -I: When $\mu_t = 0$, the jet becomes an inviscid and there is no turbulent viscosity and molecular diffusion in the flow. Then flow model is turned into the vortex sheet shock-cell model for the inviscid jet where first Fourier mode is used to solve the model. So, Eq. (3.37) is become by the following form where the term $\alpha = 0$,

$$Z''(z) + \frac{\lambda^2}{(M_j^2 - 1)} Z(z) = 0 \quad (3.38)$$

The general solution of the homogeneous ordinary differential equation (3.38) is given by,

$$Z(z) = C_3 \cos\left(\frac{\lambda z}{\sqrt{M_j^2 - 1}}\right) + C_4 \sin\left(\frac{\lambda z}{\sqrt{M_j^2 - 1}}\right). \quad (3.39)$$

In Eq. (3.39), the constant C_3 and C_4 must be met up by the boundary conditions. Using Eqs. (3.28), (3.31) and (3.39), the required general solution is formed as,

$$dp(r, z) = [C_1 J_0(\lambda r) + C_2 Y_0(\lambda r)] \times \left[C_3 \cos\left(\frac{\lambda z}{\sqrt{M_j^2 - 1}}\right) + C_4 \sin\left(\frac{\lambda z}{\sqrt{M_j^2 - 1}}\right) \right] \quad (3.40)$$

For the boundary condition (3.16) at $r = 0$, $C_2 = 0$, Eq. (3.40) becomes,

$$dp(r, z) = C_1 J_0(\lambda r) \times \left[C_3 \cos\left(\frac{\lambda z}{\sqrt{M_j^2 - 1}}\right) + C_4 \sin\left(\frac{\lambda z}{\sqrt{M_j^2 - 1}}\right) \right] \quad (3.41)$$

Again, applying the condition (3.17), the perturbed pressure gradient $\partial(dp)/\partial z = 0$ where $z = 0$ then $C_4 = 0$. So, Eq. (3.41) can be written as,

$$dp(r, z) = (C_1 C_3) \times J_0(\lambda r) \cos\left(\frac{\lambda z}{\sqrt{M_j^2 - 1}}\right) \quad (3.42)$$

Since, the jet is fully developed, so it's radius would be $r = (D_j/2)$. Then the condition (3.18) is appropriate under this circumstance for Eq. (3.42) which is given by

$$J_0(\beta_m) = 0. \quad (3.43)$$

$$\text{where, } \beta_n = \lambda \frac{D_j}{2}, \text{ and } n = 1, 2, 3, \dots \quad (3.44)$$

here, β_1, β_2 and so on are called the Bessel's zeros of Eq. (3.43) and the numbers (m) indicate the mode of Bessel's zeros. According to this condition, Eq. (3.42) becomes the following expansion series where the coefficients convey the flow characteristics of jet.

$$dp(r, z) = \sum_{m=1}^{\infty} A_m \times J_0\left(\frac{2\beta_m r}{D_j}\right) \cos\left(\frac{2\beta_m z}{D_j \sqrt{M_j^2 - 1}}\right), \quad (3.45)$$

It is noted that constant C_1, C_3 turns to the constant A_n for the series (3.45). Since all the eigen values bear the flow characteristics of jets sequentially, as though fluid particles extend significantly. Finally, Eq. (3.45) is satisfied by the condition (3.19) at the nozzle exit where the radius vector $r \in \left(0, \frac{D_e}{2}\right)$, then followings formula has been derived,

$$dp\left(0, r \in \left(0, \frac{D_e}{2}\right)\right) = \sum_{m=1}^{\infty} A_m \times J_0\left(\frac{2\beta_m r}{D_j}\right), \quad (3.46)$$

$$\begin{aligned}
&\Rightarrow rJ_0\left(\frac{2\beta_m r}{D_j}\right) \times dp\left(0, r \in \left(0, \frac{D_e}{2}\right)\right) = \sum_{m=1}^{\infty} A_m \times rJ_0^2\left(\frac{2\beta_m r}{D_j}\right), & \text{[Since jets are fully developed]} \\
&\Rightarrow \int_0^{\frac{D_j}{2}} rJ_0\left(\frac{2\beta_m r}{D_j}\right) \times dp\left(0, r \in \left(0, \frac{D_e}{2}\right)\right) dr = \sum_{m=1}^{\infty} A_m \times \int_0^{\frac{D_j}{2}} rJ_0^2\left(\frac{2\beta_m r}{D_j}\right) dr, \\
&\therefore \sum_{m=1}^{\infty} A_m = \left[\int_0^{\frac{D_j}{2}} rJ_0\left(\frac{2\beta_m r}{D_j}\right) \times dp\left(0, r \in \left(0, \frac{D_e}{2}\right)\right) dr \right] / \left[\int_0^{\frac{D_j}{2}} rJ_0^2\left(\frac{2\beta_m r}{D_j}\right) dr \right], \quad (3.47)
\end{aligned}$$

Equation (3.47) is established according to the Fourier formula for the expansion of Bessel's function. Now applying the integral recurrence formula of Bessel's function and imposing the pressure raise with the particular range of developing jets, then Eq. (3.47) gives,

$$\begin{aligned}
A_m &= \left[\int_0^{\frac{D_e}{2}} rJ_0\left(\frac{2\beta_m r}{D_j}\right) \times (\Delta p) dr + \int_{\frac{D_e}{2}}^{\frac{D_j}{2}} (0) \times dr \right] / \left[\int_0^{\frac{D_j}{2}} rJ_0^2\left(\frac{2\beta_m r}{D_j}\right) dr \right] \\
&\Rightarrow A_n = \left[\int_0^{\frac{D_e}{2}} rJ_0\left(\frac{2\beta_m r}{D_j}\right) \times (\Delta p) dr \right] / \left[\frac{\left(\frac{D_j}{2}\right)^2}{2} J_1^2\left(\frac{2\beta_m \times \frac{D_j}{2}}{D_j}\right) \right], \\
&\Rightarrow A_m = \left[\frac{2\Delta p}{\left(\frac{2\beta_m}{D_j}\right)^2} \int_0^{\frac{2\beta_m \times \frac{D_e}{2}}{D_j}} \left(\frac{2\beta_m r}{D_j}\right) J_0\left(\frac{2\beta_m r}{D_j}\right) d\left(\frac{2\beta_m r}{D_j}\right) \right] / \left[\left(\frac{D_j}{2}\right)^2 J_1^2(\beta_m) \right], \\
&\Rightarrow A_m = \left[\frac{2\Delta p}{\left(\frac{2\beta_m}{D_j}\right)^2} \times \left[\left(\frac{2\beta_m r}{D_j}\right) J_1\left(\frac{2\beta_m r}{D_j}\right) \right]_0^{\frac{2\beta_m \times \frac{D_e}{2}}{D_j}} \right] / \left[\left(\frac{D_j}{2}\right)^2 J_1^2(\beta_m) \right], \\
&\Rightarrow A_m = \left[\frac{2\Delta p}{\left(\frac{2\beta_m}{D_j}\right)^2} \times \left(\frac{2\beta_m}{D_j} \times \frac{D_e}{2}\right) \times J_1\left(\frac{2\beta_m}{D_j} \times \frac{D_e}{2}\right) \right] / \left[\left(\frac{D_j}{2}\right)^2 \times J_1^2(\beta_m) \right], \\
&\therefore A_m = \frac{\left(2\Delta p \times \frac{D_e}{D_j}\right) \times J_1\left(\beta_m \frac{D_e}{D_j}\right)}{\beta_n \times J_1^2(\beta_m)}. \quad (3.48)
\end{aligned}$$

By using Eq. (3.45), the particular form of Eq. (3.40) can be written as,

$$dp(r, z) = \sum_{m=1}^{\infty} \frac{\left(2\Delta p \times \frac{D_e}{D_j}\right) \times J_1\left(\beta_m \frac{D_e}{D_j}\right)}{\beta_m \times J_1^2(\beta_m)} \times J_0\left(\frac{2\beta_m r}{D_j}\right) \cos\left(\frac{2\beta_m z}{D_j \sqrt{M_j^2 - 1}}\right), \quad (3.49)$$

Equation (3.49) is the complete solution of Eq. (3.27) where the viscosity $\mu_t = 0$. Putting the value of Eq. (3.49) in the pressure term of Eq. (3.11), then the total pressure equation becomes,

$$\begin{aligned} p &= p_j + \left(2\Delta p \times \frac{D_e}{D_j}\right) \sum_{m=1}^{\infty} \frac{J_1\left(\beta_m \frac{D_e}{D_j}\right)}{\beta_m J_1^2(\beta_m)} J_0\left(\frac{2\beta_m r}{D_j}\right) \cos\left(\frac{2\beta_m z}{D_j \sqrt{M_j^2 - 1}}\right), \\ \Rightarrow p &= p_j + 2(p_e - p_b) \left(\frac{D_e}{D_j}\right) \times \left[\sum_{m=1}^{\infty} \frac{J_1\left(\beta_m \frac{D_e}{D_j}\right)}{\beta_m J_1^2(\beta_m)} J_0\left(\frac{2\beta_m r}{D_j}\right) \cos\left(\frac{2\beta_m z}{D_j \sqrt{M_j^2 - 1}}\right) \right] \\ \therefore \frac{p}{p_j} &= 1 + 2\left(\frac{p_e - p_b}{p_j - p_b}\right) \left(\frac{D_e}{D_j}\right) \times \left[\sum_{m=1}^{\infty} \frac{J_1\left(\beta_m \frac{D_e}{D_j}\right)}{\beta_m J_1^2(\beta_m)} J_0\left(\frac{2\beta_m r}{D_j}\right) \cos\left(\frac{2\beta_m z}{D_j \sqrt{M_j^2 - 1}}\right) \right] \quad (3.50) \end{aligned}$$

Since the extended pressure has the tendency to make balance with ambient pressure at the boundary of extended diameter (D_j), then ratio of (p/p_j) is also tends to ratio (p/p_b). In mathematically,

$$\frac{p}{p_j} = \frac{p}{p_b} \quad (3.51)$$

Therefore, Eq. (3.50) becomes as the following required explicit form of normalized pressure,

$$\frac{p}{p_b} = 1 + 2\left(\frac{p_e}{p_b} - 1\right) \left(\frac{D_e}{D_j}\right) \left[\sum_{m=1}^{\infty} \frac{J_1\left(\beta_m \frac{D_e}{D_j}\right)}{\beta_m J_1^2(\beta_m)} J_0\left(2\beta_m \frac{D_e}{D_j} \frac{r}{D_e}\right) \cos\left(\frac{2\beta_m}{\sqrt{M_j^2 - 1}} \frac{D_e}{D_j} \frac{z}{D_e}\right) \right] \quad (3.52)$$

Again, the density of underexpanded jet can also be measured from the pressure equation (3.52) by applying Eq. (2.69), then the pressure and density are related as,

$$\frac{p}{p_j} = \frac{p}{p_b} = \left(\frac{\rho}{\rho_j}\right)^\gamma, \quad (3.53)$$

The symbol γ is the specific heat constant and the extended density is differed from the ambient density, *i. e* $\rho_j \neq \rho_b$, then Eq. (3.52) turns to,

$$\frac{\rho}{\rho_j} = 1 + \frac{2}{\gamma} \left(\frac{p_e}{p_b} - 1 \right) \left(\frac{D_e}{D_j} \right) \times d\rho_{ap} \left(\frac{r}{D_e}, \frac{z}{D_e} \right), \quad (3.54)$$

$$\text{where, } d\rho_{ap} \left(\frac{r}{D_e}, \frac{z}{D_e} \right) = \left[\sum_{m=1}^{\infty} \frac{J_1 \left(\beta_m \frac{D_e}{D_j} \right)}{\beta_m J_1^2(\beta_m)} J_0 \left(2\beta_m \frac{D_e}{D_j} \frac{r}{D_e} \right) \cos \left(\frac{2\beta_m}{\sqrt{M_j^2 - 1}} \frac{D_e}{D_j} \frac{z}{D_e} \right) \right] \quad (3.55)$$

But Eq. (3.54) can be de formed as,

$$\rho = \rho_j \left[1 + \frac{2}{\gamma} \left(\frac{p_e}{p_0} \times NPR - 1 \right) \left(\frac{D_e}{D_j} \right) \times d\rho_{ap} \left(\frac{r}{D_e}, \frac{z}{D_e} \right) \right]. \quad (3.56)$$

In Eq. (3.54), $NPR = (p_0/p_b)$ is called nozzle pressure ratio of the nozzle stagnation pressure (p_0) to the ambient pressure (p_b). And the ratio (p_e/p_0) obey the relation (2.73) through,

$$\frac{p_0}{p_e} = \left(1 + \frac{\gamma - 1}{2} M_e^2 \right)^{\frac{\gamma}{\gamma - 1}}, \quad (3.57)$$

where, M_e is the design Mach number or exit Mach number and the extended Mach number (M_j) can also be measured from Eq. (2.73) in terms of NPR as,

$$\begin{aligned} NPR = \frac{p_0}{p_j} &= \left(1 + \frac{\gamma - 1}{2} M_j^2 \right)^{\frac{\gamma}{\gamma - 1}}, \\ \therefore M_j &= \sqrt{\frac{2}{\gamma - 1} \left(NPR^{\frac{\gamma - 1}{\gamma}} - 1 \right)} \end{aligned} \quad (3.58)$$

It is very important to know that the jet flow is only effective within the range of jet operating conditions which is defined by M_j and M_e as,

$$|M_j^2 - M_e^2| < 1, \quad (3.59)$$

On the other hand, according to the properties of isentropic flow where stagnation temperature (T_0) and the ambient Temperature (T_b) are equal, the following assumptions are required as,

$$\frac{\rho_j}{\rho_b} = \frac{\rho_j}{\rho_0} \times \frac{\rho_0}{\rho_b} \quad (3.60)$$

Using Eqs. (2.3) and (2.69) in (3.60), then

$$\begin{aligned} \frac{\rho_j}{\rho_b} &= \left(\frac{p_j}{p_0}\right)^{1/\gamma} \times \left(\frac{\frac{p_0}{RT_0}}{\frac{p_b}{RT_b}}\right) \\ \therefore \frac{\rho_j}{\rho_b} &= \left(\frac{p_j}{p_0}\right)^{1/\gamma} \times \frac{p_0}{p_b} \end{aligned} \quad (3.61)$$

Using Eq. (3.51), then Eq. (3.61) can also be written by

$$\rho_j = \rho_b \left[\left(\frac{p_b}{p_0}\right)^{\frac{1}{\gamma}} \times \frac{p_0}{p_b} \right] = \rho_b \times NPR^{\frac{\gamma-1}{\gamma}} \quad (3.62)$$

Through Eq. (3.62), the density equation (3.56) stands for

$$\frac{\rho}{\rho_b} = NPR^{\frac{\gamma-1}{\gamma}} \left[1 + \frac{2}{\gamma} \left(\frac{p_e}{p_0} \times NPR - 1\right) \left(\frac{D_e}{D_j}\right) \times d\rho_{ap} \left(\frac{r}{D_e}, \frac{z}{D_e}\right) \right], \quad (3.63)$$

which is the normalized density profile of the underexpanded jet. In Eqs. (3.52) and (3.63), the ratio (D_e/D_j) can be evaluated by using Eq. (2.78) as,

$$\begin{aligned} \frac{A_e}{A_j} &= \left(\frac{D_e}{D_j}\right)^2 = \frac{M_j}{M_e} \left[\frac{(\gamma-1)M_e^2 + 2}{(\gamma-1)M_j^2 + 2} \right]^{\frac{\gamma+1}{2(\gamma-1)}} \\ \therefore \frac{D_e}{D_j} &= \sqrt{\frac{M_j}{M_e} \left[\frac{(\gamma-1)M_e^2 + 2}{(\gamma-1)M_j^2 + 2} \right]^{\frac{\gamma+1}{2(\gamma-1)}}}. \end{aligned} \quad (3.64)$$

Therefore, the theoretical pressure and density prediction of fully expanded inviscid jet can be performed by Eqs. (3.52) and (3.63) respectively where NPR , M_e , and γ have to be considered as preassigned parameter. Centre line measures and mesh contours of pressure and density can also be demonstrated through these assumptions linking with the source [52].

Case-II: When $\mu_t \neq 0$, then the turbulent viscosity has to consider in the flow of jet and Eq. (3.37) is remain unchanged. Then the modified model obeys the mean flow model proposed by Emami et al. [18] for the round jet. To find the explicit solution of underexpanded jet for the **case-II** where coefficient $\alpha \neq 0$, Eq. (3.37) is reformed by,

$$Z''''(z) + \left(\frac{1 - M_j^2}{\alpha}\right) Z''(z) - \lambda^2 Z'(z) - \frac{\lambda^2}{\alpha} Z(z) = 0, \quad (3.65)$$

Equation (3.65) is a third order homogeneous ordinary differential equation with constant coefficient. Now, for a trail solution $Z(z) = e^{\sigma z}$, the characteristics equation is given by

$$\sigma^3 + \left(\frac{1 - M_j^2}{\alpha}\right) \sigma^2 - \lambda^2 \sigma - \frac{\lambda^2}{\alpha} = 0. \quad (3.66)$$

In Eq. (3.66) is a third-degree polynomial that has three roots. Due to the Descartes' rule of signs for Eq. (3.66) where no change of sign has been occurred two times and change of sign occurred one time, so there has one real root and two complex roots. The well-known Cardano's formula is applied to solve Eq. (3.66), then considering a general form of polynomial of degree three is given by

$$\sigma^3 + a_1 \sigma^2 + a_2 \sigma + a_3 = 0, \quad (3.67)$$

where, Eq. (3.66) and Eq. (3.67) are identical. According to the Cardano's formula, three roots S_1, S_2 , and S_3 of Eq. (3.67) can be written as,

$$S_1 = S + T - \frac{a_1}{3}, S_2 = -\frac{1}{2}(S + T) - \frac{a_1}{3} + i \frac{\sqrt{3}}{2}(S - T), \quad (3.68)$$

$$S_3 = -\frac{1}{2}(S + T) - \frac{a_1}{3} - i \frac{\sqrt{3}}{2}(S - T),$$

In Eq. (3.68), the used symbols S and T are real numbers, whereas i is the complex number. The coefficient a_1, a_2 , and a_3 are bear the following values,

$$a_1 = \frac{1 - M_j^2}{\alpha}, \quad a_2 = -\lambda^2, \quad a_3 = -\frac{\lambda^2}{\alpha}. \quad (3.69)$$

Also, the real S and T in Eq. (3.68) holds the following formula to make the meaningful roots of Eq. (3.67) as,

$$S = \sqrt[3]{R + \sqrt{Q^3 + R^2}}, \quad T = \sqrt[3]{R - \sqrt{Q^3 + R^2}}; \quad (3.70)$$

where, the quantities Q and R bear the below figures which are given by

$$Q = \frac{3a_2 - a_1^2}{9}, \quad R = \frac{9a_1a_2 - 7a_3 - 2a_1^3}{54}. \quad (3.71)$$

The general solution of Eq. (3.65) can be written with the three S_1 , S_2 and S_3 characteristics roots of the indicial Eq. (3.66) as,

$$Z(z) = C_5 e^{S_1 z} + C_6 e^{S_2 z} + C_7 e^{S_3 z} \quad (3.72)$$

$$\Rightarrow Z(z) = C_5 e^{(S+T-\frac{a_1}{3})z} + C_6 e^{\left(-\frac{1}{2}(S+T)-\frac{a_1}{3}+i\frac{\sqrt{3}}{2}(S-T)\right)z} + C_7 e^{\left(-\frac{1}{2}(S+T)-\frac{a_1}{3}-i\frac{\sqrt{3}}{2}(S-T)\right)z},$$

$$\therefore Z(z) = C_5 e^{(S+T-\frac{a_1}{3})z} + e^{\left[-\frac{1}{2}(S+T)-\frac{a_1}{3}\right]z} \left\{ C_6 e^{i\frac{\sqrt{3}}{2}(S-T)z} + C_7 e^{-i\frac{\sqrt{3}}{2}(S-T)z} \right\}. \quad (3.73)$$

Since the postulation of isentropic flow is deemed the wave equation where damped oscillation has to demand by the system. Omitting the term with arbitrary constant C_5 , the asking solution (3.73) is formed where terms with arbitrary constant C_6 , and C_7 are containing as,

$$Z(z) = e^{\left[-\frac{1}{2}(S+T)+\frac{a_1}{3}\right]z} \left\{ C_6 e^{i\frac{\sqrt{3}}{2}(S-T)z} + C_7 e^{-i\frac{\sqrt{3}}{2}(S-T)z} \right\}. \quad (3.74)$$

The rearranging form of Eq. (3.74) yields the general solution of Eq. (3.65) is given by

$$Z(z) = e^{-\varphi z} \{ c_6 \cos(\omega z) + c_7 \sin(\omega z) \}, \quad (3.75)$$

$$\varphi = \left[\frac{1}{2}(S+T) + \frac{a_1}{3} \right], \quad \omega = \frac{\sqrt{3}}{2}(S-T). \quad (3.76)$$

Using Eqs. (3.28), (3.31) and (3.76), the general solution of Eq. (3.27) for **case-II** is made by

$$dp(r, z) = [C_1 J_0(\lambda r) + C_2 Y_0(\lambda r)] \times e^{-\varphi z} \{ C_6 \cos(\omega z) + C_7 \sin(\omega z) \}. \quad (3.77)$$

After attending the boundary conditions (3.16), Eq. (3.77) enhances as,

$$dp(r, z) = C_1 J_0(\lambda r) \times e^{-\varphi z} \{C_6 \cos(\omega z) + C_7 \sin(\omega z)\}. \quad (3.78)$$

Now imposing Eq. (31.7) in Eq. (3.78) where perturbed pressure gradient $(\partial dp/\partial z) = 0$ at $z = 0$, then it is given by

$$\begin{aligned} \frac{\partial dp}{\partial z}(r, z) &= C_1 C_6 J_0(\lambda r) \times (-\varphi e^{-\varphi z}) \left\{ \cos(\omega z) + \frac{C_7}{C_6} \sin(\omega z) \right\} \\ &\quad + C_1 C_6 J_0(\lambda r) \times e^{-\varphi z} \left\{ -\omega \sin(\omega z) + \frac{C_7}{C_6} \omega \cos(\omega z) \right\}, \\ \Rightarrow \frac{\partial dp}{\partial z}(r, 0) &= C_1 C_6 J_0(\lambda r) \times (-\varphi) + C_1 C_6 J_0(\lambda r) \times \left(\frac{C_7}{C_6} \omega \right), \\ &\Rightarrow C_1 C_6 J_0(\lambda r) \times \left\{ -\varphi + \frac{C_7}{C_6} \omega \right\} = 0, \\ &\therefore \frac{C_7}{C_6} = \frac{\varphi}{\omega}. \end{aligned} \quad (3.79)$$

Eq. (3.79) can be reformed by the following way,

$$dp(r, z) = C_1 C_6 J_0(\lambda r) \times e^{-\varphi z} \left\{ \cos(\omega z) + \frac{\varphi}{\omega} \sin(\omega z) \right\}. \quad (3.80)$$

Now, according to the condition (3.18), the obtained Eq. (3.43) is used to fix the quantities φ and ω of Eq. (3.76) which are depended on the eigen vales relation (3.44) as,

$$\varphi_n = \left[\frac{1}{2}(S + T) + \frac{a_1}{3} \right], \quad \omega_n = \frac{\sqrt{3}}{2}(S - T). \quad (3.81)$$

In Eq. (3.78), all linked parameters are also replaced by Eq. (3.43), Eq. (3.80) is developed by

$$dp(r, z) = \sum_{m=1}^{\infty} A_n J_0 \left(\frac{2\beta_m}{D_j} r \right) \times e^{-\varphi_m z} \left\{ \cos(\omega_m z) + \frac{\varphi_m}{\omega_m} \sin(\omega_m z) \right\}. \quad (3.82)$$

Finally, Eq. (3.82) is satisfied by the condition (3.19) where the nozzle exit radius vector $r \in \left(0, \frac{D_e}{2} \right)$, then the value of A_n is replaced by Eq. (3.48). Therefore, the explicit particular solution has been derived as,

$$dp(r, z) = \sum_{m=1}^{\infty} \frac{\left(2\Delta p \times \frac{D_e}{D_j}\right) J_1\left(\beta_m \frac{D_e}{D_j}\right)}{\beta_m J_1^2(\beta_m)} J_0\left(\frac{2\beta_m}{D_j} r\right) \times Z_{comp}(z), \quad (3.83)$$

$$\text{where, } Z_{comp}(z) = \left[e^{-\varphi_n z} \left\{ \cos(\omega_n z) + \frac{\varphi_n}{\omega_n} \sin(\omega_n z) \right\} \right]. \quad (3.84)$$

Using Eqs. (3.50) to (3.52), the normalized pressure equation becomes form Eq. (3.83) as,

$$\frac{p}{p_b} = 1 + 2 \left(\frac{p_e}{p_b} - 1 \right) \left(\frac{D_e}{D_j} \right) \left[\sum_{m=1}^{\infty} \frac{J_1\left(\beta_m \frac{D_e}{D_j}\right)}{\beta_m J_1^2(\beta_m)} J_0\left(2\beta_m \frac{D_e}{D_j} \frac{r}{D_e}\right) \times Z_{comp}(z) \right]. \quad (3.85)$$

Again, by following Eqs. (3.53) to (3.63), the normalized density can be measured from

$$\frac{\rho}{\rho_b} = NPR^{\frac{\gamma-1}{\gamma}} \left[1 + \frac{2}{\gamma} \left(\frac{p_e}{p_0} \times NPR - 1 \right) \left(\frac{D_e}{D_j} \right) \times d\rho_{vis} \left(\frac{r}{D_e}, \frac{z}{D_e} \right) \right], \quad (3.86)$$

$$\text{where, } d\rho_{vis} \left(\frac{r}{D_e}, \frac{z}{D_e} \right) = \sum_{m=1}^{\infty} \frac{J_1\left(\beta_m \frac{D_e}{D_j}\right)}{\beta_m J_1^2(\beta_m)} J_0\left(2\beta_m \frac{D_e}{D_j} \frac{r}{D_e}\right) \times Z_{comp}(z) \quad (3.87)$$

Consequently, the normalized pressure and density profile of fully expanded turbulent viscous jet has been analyzed by Eqs. (3.85) and (3.86) respectively. Then Eq. (3.26 becomes,

$$\alpha/D_e = \frac{4}{3} \times \left(\frac{U_j^2}{a_j^2} \right) / \left(\frac{U_j \rho_j}{\mu_t} \right) = \frac{\left(\frac{4}{3} \right) \times M_j^2}{R_{ed}}, \quad (3.88)$$

$$\text{where, } R_{ed} = \frac{D_e U_j \rho_j}{\mu_t} \quad (3.89)$$

Now applying Eq. (3.15) in Eq. (3.89), the modified Reynolds number (R_{ed}) becomes as,

$$R_{ed} = \frac{(D_e/D_j) \times \left(\frac{\rho_j}{\rho_b} \right)^{0.28}}{\eta(1 - 0.16M_j)} \quad (3.90)$$

From Eqs. (3.90) and (3.88), the quantity α is normalized by

$$\alpha/D_e = \left(\frac{4\eta}{3}\right) \times \frac{M_j^2(1 - 0.16M_j)}{\left(\frac{\rho_j}{\rho_b}\right)^{0.28} \left(\frac{D_e}{D_j}\right)}, \quad (3.91)$$

Also, using Eq. (3.69), the normalized coefficients are,

$$a_1 = \frac{1 - M_j^2}{\alpha/D_e}, \quad a_2 = -\left(\frac{2\beta_m}{\frac{D_e}{D_j}}\right)^2, \quad a_3 = -\left(\frac{2\beta_m}{\frac{D_e}{D_j}}\right)^2 / (\alpha/D_e). \quad (3.92)$$

Subsequently, the center line pressure and density with mesh contour of viscous turbulent underexpanded jet can also be fitted with the appropriate values of η through Eqs. (3.85) and (3.86) separately where the value of catalyzers NPR , M_e , and γ have to be considered according to the flow field. The inbuilt outputs of this case-II are referenced from [53].

3.5 Results and Discussion

3.5.1 Experimental Analysis

3.5.1.1 Rainbow Schlieren Pictures

Jets from a Mach 1.5 round Laval nozzle followed by a cylindrical duct were visualized using a rainbow schlieren system as shown in Fig. 3.6. The flow is from left to right. Schlieren pictures were taken at an exposure time of $1/8000$ s with continuous schlieren light source. In addition, a rainbow filter was placed at the cut-off plane in parallel with respect to the z axis and its orientation is illustrated above Fig. 3.6(a) with the location of the background hue represented as the dashed line on the filter. The value of the nozzle pressure ratio (NPR) is given in the upper right corner of each picture. It should be kept in mind that the jet issued from the duct exit is correctly expanded at $NPR = 3.67$ if the whole flow field through the Laval nozzle and duct obeys the isentropic process. In addition, the inviscid theory shows that the flow field is governed by three different flow features, namely, the flows with a stationary normal shock in the divergent portion of the Laval nozzle for a range of NPR s from 1.29 to 1.49, overexpanded flows for a range of NPR s from 1.49 to 3.67, and underexpanded flows for NPR s beyond 3.67. However, since the nozzle and duct flows are affected by wall friction, the schlieren pictures of Fig. 3.6 display an effect of the wall friction on jets from the duct exit.

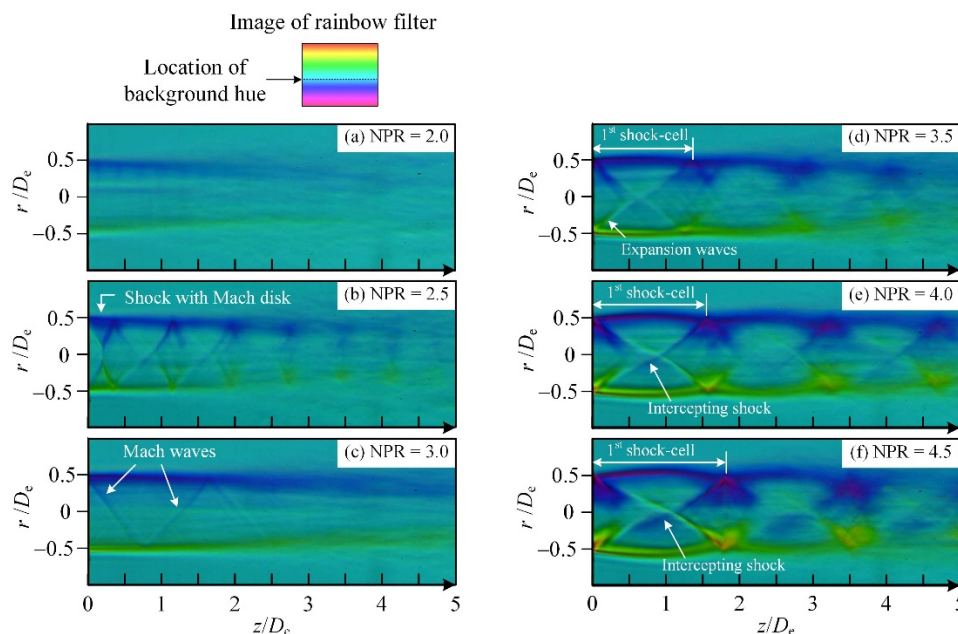


Fig. 3.6: Rainbow schlieren pictures of jet from Laval nozzle with long duct.

Figure 3.6(a) is in the overexpanded flow state ideally, but no regular shock or Mach stem appears in the jet. It presumably shows the flow behind a pseudo-shock wave in the straight duct [50]. Figure 3.6(b) indicates a conventional overexpanded jet because a shock with a Mach stem is present near the duct exit. As shown in Figure 3.6(c), when NPR increases to 3.0, no significant shocks appear in the jet plume. It means that shocks change into Mach waves or weak shocks. This indicates the correctly expanded jet condition for the present Laval nozzle followed by the long duct. In this situation, the wall friction in the cylindrical duct causes the flow Mach number at the duct exit to be less than the isentropic exit Mach number of 1.5. In the case of $NPR = 3.0$, a simple estimation of the Mach number averaged over the cross-section at the duct exit becomes 1.36. An increase in NPR from 3.0 to 3.5 contributes to the occurrence of expansion waves from the duct exit, as shown in Fig. 3.6(d) and the shock-cell structure is quasi-periodically repeated in the flow direction. Figures 3.6(e) and 3.6(f) show that a further increase of NPR from 3.5 to 4.0 or 4.5 causes an intercepting shock to produce in the jet and the shock-cell spacing or the strength of the shock increase as NPR increases.

3.5.1.2 Density Contour Plots

The schlieren pictures of Fig. 3.6 show only qualitative flow features of the jet. Nevertheless, it sometimes utilizes as a comparison for a validation of the results obtained by CFD. However, the validation of simulations by comparisons with the geometrical shapes of shock waves from the schlieren pictures should be done with care, because the pictures display a line-of-sight imaging, or information averaged along the view direction about the first spatial derivative of density profile. In addition, the schlieren image can be changed easily by adjusting the contrast. On the contrary, the density field on a cross-section of the jet would be effective for reliable validation of simulated results. Figures 3.7(a) ~ 3.7(f) exhibit density contour plots of the jets normalized by the ambient density ρ_b where the flow is from left to right. The contour levels with an interval of 0.0625 are shown at the top, and the spatial resolution in the experimental density map is around $13 \mu m$. The schlieren picture can only provide integrated information about the density gradient along in the direction of the optical axis, but Figs. 3.7(a) ~ 3.7(f) can clearly demonstrate the quantitative information of the density fields of the jets. The jet density fields are reconstructed using the convolution back-projection (CBP) method. Unlike the schlieren pictures of Fig. 3.6, the density contour plots shown in Fig. 3.7 illustrate the various flow features of the near-field shock structures quantitatively, such as the shape and size of the expansion and compression regions, shock cell intervals, jet boundaries and so on.

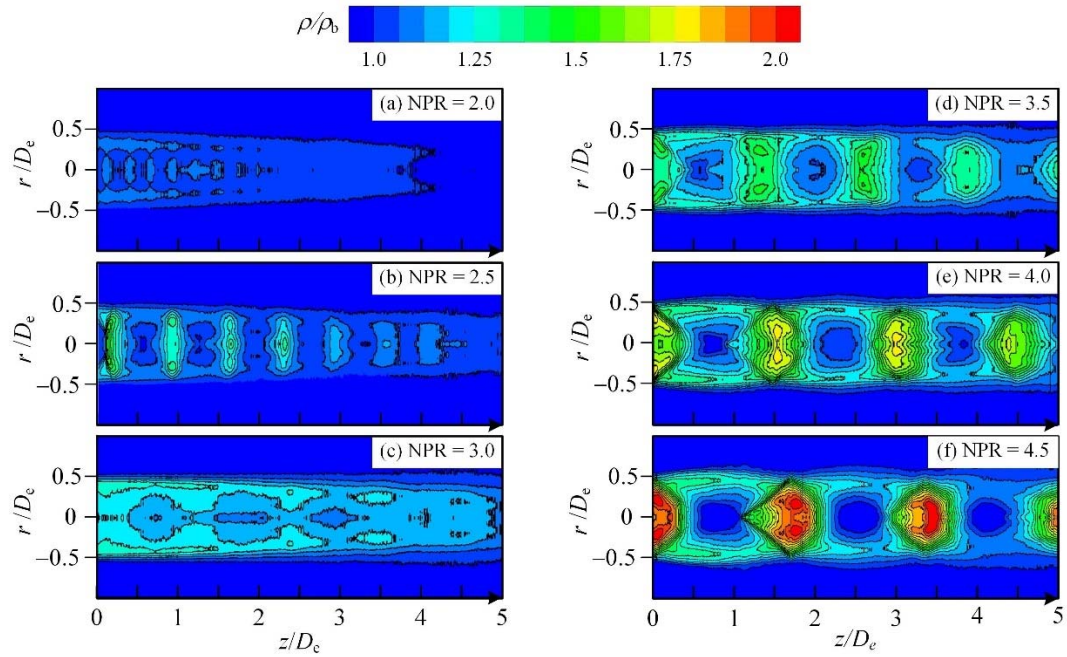


Fig. 3.7: Density contour plots of jet issued from Laval nozzle with duct.

Figure 3.7(a) indicates a series of weak shocks arranged at almost equal spacings in the region less than $z/D_e =$ around 1.0. As shown in Fig. 3.7(b), an increase in NPR results in strengthening the shocks and a shock with a Mach disk appears just downstream of the duct exit and followed by a series of shock-cells with weak shocks like compression waves. It shows a typical feature of the overexpanded flows. Further increase in NPR causes all shocks including the Mach disk to disappear, as shown in Fig. 3.7(c). This nozzle pressure ratio ($NPR = 3.0$) makes the correctly expanded flow with respect to the present nozzle. It should be noted that the theoretical nozzle pressure ratio based upon the assumption of the isentropic flow through the present nozzle is 3.671. As shown in Figs. 3.7(e) and 3.7(f), additional increases in NPR cause the expansion waves at the duct exit to produce and the degree of expansion increase with increasing NPR .

3.5.1.3 Density Profiles along Jet Centerline

Effects of the nozzle pressure ratio on jet centreline density profiles are shown in Figs. 3.8(a) ~3.8(f). The leftward arrow on the vertical axis in each figure indicates the theoretical density ratio at the duct exit when the isentropic flow is assumed through both the nozzle and duct. In addition, the value of the fully expanded jet density ρ_j normalized by the ambient density ρ_b for each nozzle pressure ratio is shown as the dashed horizontal line in the figure. All density data in Figs. 3.8(a) ~3.8(f) are normalized by the ambient density ρ_b .

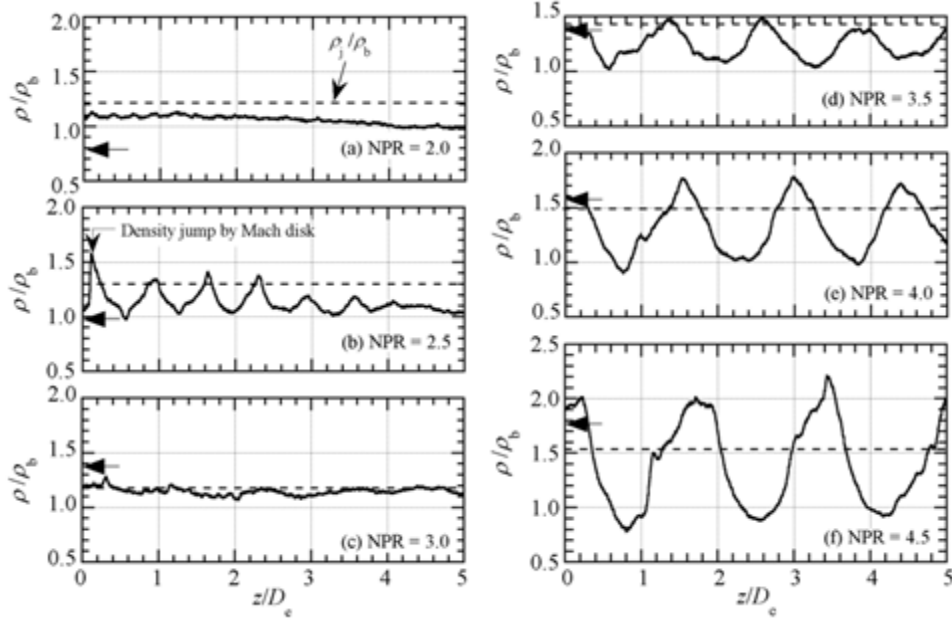


Fig. 3.8: Centerline density profiles of jet issued from Laval nozzle with long duct.

In case of $NPR = 2.0$, multiple weak shocks with a small amplitude of almost equal intervals can be observed faintly between the duct exit and $z/D_e =$ around 1.0. The density fluctuations with a small amplitude just downstream of the duct exit are responsible for the shock-train [57]. For $NPR = 2.5$, a distinct spike in the density profile contributed to the Mach disk appears just downstream of the duct exit. The Mach disk has the maximum density rise and the subsequent shock-cells indicate density increments of almost the same order of magnitude. No significant shocks appear for $NPR = 3.0$ because of the correctly expanded flow condition. For NPR s beyond the $NPR = 3.0$, flow expansion and compression are repeated toward downstream due to the quasi-periodic shock-cell structure. Particularly, for $NPR = 4.5$, the local density fluctuates about ρ_j/ρ_b and it decrease below ρ_j/ρ_b in the expansion region of each shock-cell and increases above ρ_j/ρ_b in the compression region. The sudden density increases at $z/D_e = 1.1$ (around) due to the intercepting shock in the first shock-cell, as shown in Fig. 3.8(f).

3.5.1.4 Effect of Cylindrical Duct

Effects of the cylindrical duct on the density profile along the jet centreline for $NPR = 4.0$ are shown in Fig. 3.9. The black line indicates the same experimental data as Fig. 3.8(e) and the blue one shows the experimental results conducted by Maeda et al. [29]. The red line parallel to the abscissa shows the level of the normalized fully expanded density (ρ_j/ρ_b) and the leftward arrow on the vertical axis is the normalized exit density estimated based on the

assumption of the isentropic flow from the nozzle inlet to the duct exit. The effect of wall friction on the jet structure cannot be clarified from only the schlieren photographs in Fig. 3.6. However, it can predict the friction effect from a quantitative comparison between the density distributions from the Laval nozzles with and without a long duct as shown in Fig. 3.9.

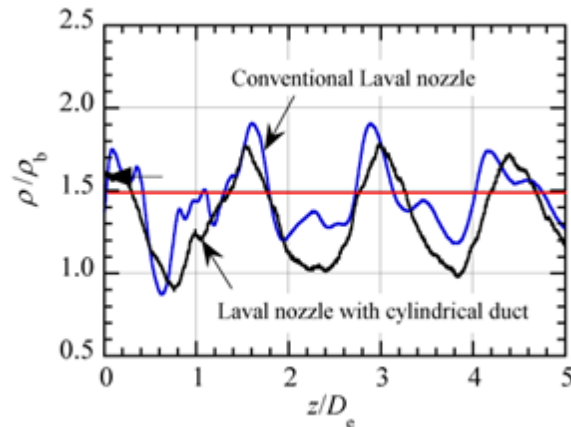


Fig.3.9: Effect of cylindrical duct on jet centerline density profile for $NPR = 4.0$.

Both density profiles for the Laval nozzles with and without the cylindrical duct are very similar to each other in overall trend. The black line shows that the density values at the local minima and local maxima in the density profile are kept almost constant toward the downstream. While the blue line contains higher frequency components when compared to the black line. What needs to be emphasized is that the exit densities for both density profiles are approximately equal to the theoretical exit density. However, the Mach number averaged over the cross-section at the exit is lower in the Laval nozzle with the cylindrical duct than in the conventional Laval nozzle, i.e., the density profiles are affected by the Mach number distribution at the nozzle exit. The Fanno flow theory [58] states that the maximum possible length where the flow is not choked at the duct exit is 85 mm for a constant-area duct with an inlet Mach number of 1.5, constant Fanning friction factor of 0.004 [59], and duct diameter of 10 mm. So, the average Mach number over the cross-section of the duct exit is beyond unity.

3.5.1.5 Three-Dimensional Jet Structure

The three-dimensional structures of two typical shock-containing jets are illustrated in Figs. 3.10 with the respective isopycnic surface, which displays a surface of constant density inside the jet. These descriptions are useful in assessing the structure of density fields including shocks in which the flow properties change rapidly. The range of the density is shown as a

colour bar in the top of the figure. Fig. 3.10 shows overexpanded ($NPR = 2.5$) and underexpanded ($NPR = 4.5$) jet structures, respectively, and they correspond to Figs. 3.7(b) and 3.7(f). As shown in Fig. 3.10(a), the three-dimensional flow features of the Mach disk just downstream of the duct exit as well as the following downstream successive weak shocks with a circular shape each can be seen clearly with suddenly varying colour. Figure 3.10(b) shows that the oblique shocks in shock-cells are reflected at the opposite jet free boundaries to form bicone structure. The structure gradually becomes smaller in shape toward downstream.

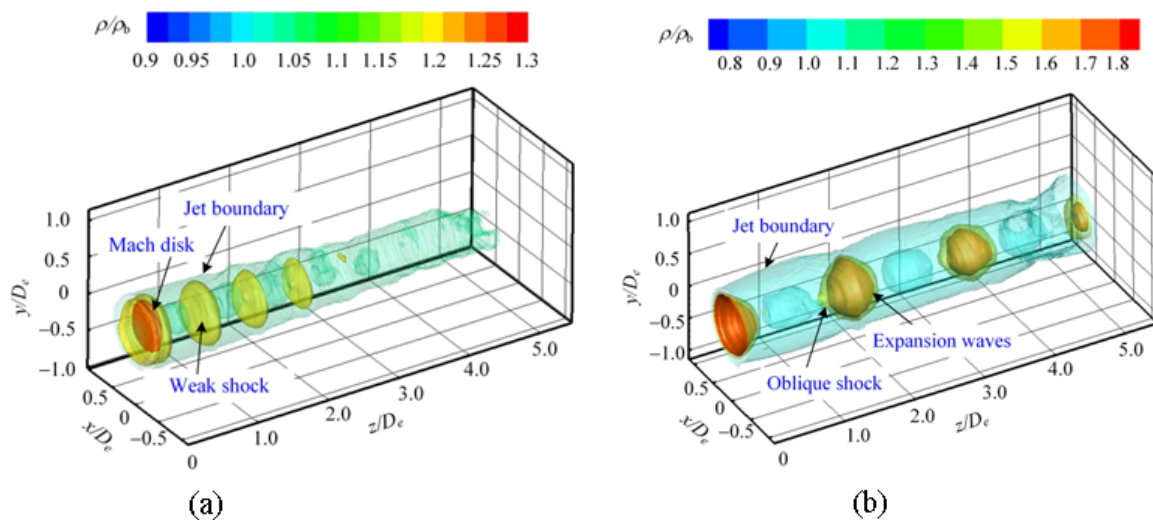


Fig. 3.10. Isopycnic surfaces of (a) overexpanded jets and (b) underexpanded jets.

3.5.1.6 Concluding Remarks of Rainbow Schlieren Pictures

The density fields of jets from a round Laval nozzle followed by a cylindrical duct were measured by the rainbow schlieren deflectometry. The three-dimensional density fields of the jets were reconstructed by the convolution back-projection (CBP) method to investigate the effects of the nozzle pressure ratio on the jet structure. A quantitative comparison between the centerline density profiles from the Laval nozzles with and without a cylindrical duct was performed. As a result, it was found that the jet from the Laval nozzle with the cylindrical duct reaches a shock-free state at a nozzle pressure ratio lower than the design condition because of the wall friction along the duct wall. However, the freestream Mach number at the cylindrical duct exit is almost the same as that calculated based upon the assumption of the isentropic flow. The cylindrical duct causes the average Mach number at the exit to be reduced, but not change the freestream Mach number at the duct exit and it smooths the density profile when compared with that for the jet issued from the conventional Laval nozzle. Two types of shock-containing jets showing overexpanded and underexpanded states were displayed with the respective

isopycnic surface and it was found that the overexpanded jet produces a Mach disk following by successive weak shocks with a circular shape, while the underexpanded jet forms a bicone structure composed of an oblique shock and expansion waves in each shock-cell, which gradually becomes smaller in shape toward downstream. The results are exemplified by the peer reviewed journal [15].

3.5.2 Theoretical Analysis

3.5.2.1 Theoretical Density Profile along Jet Centerline

A centerline density profiles of a free jet issued from an axisymmetric convergent nozzle are compared between theory and experiment [52] under a condition of $NPR = 3.0$ as shown in Fig. 3.11 where the black solid line is the experimental result [52] from the rainbow schlieren deflectometry, the green line is the Emami et al.[18] theoretical outcome, and the red and blue solid lines are ones calculated by using the modified theory. The solution of first mode ($m = 1$) only is considered in the present study as a first stage. The abscissa is the normalized streamwise distance from the nozzle exit and the ordinate is the normalized density. The black leftward arrow on the vertical axis indicates the experimental density value (1.86) measured from RSD data sheet, whereas the pink leftward arrow specifies the theoretical density value (2.28) calculating upon the assumption of the isentropic flow from the nozzle inlet to exit.

The experimental density profile shows that the density gradually decreases with downstream distance from the nozzle exit till the minimum value which is sufficiently lower than the ambient density before a gradual increase in the downstream direction, and then reaches the first local maximum to form the first shock-cell structure. A similar decrease and increase in density are quasi-periodically repeated in the downstream direction with a gradual decrease in the local maxima and minima of the density profile, while the modified theoretical density profiles (magenta curve) exhibit remarkably similar effects of attenuation due to the turbulent viscosity. In particular, the theoretical blue one is significantly displayed a periodical curve for inviscid jet which is same as the Tam's [16] flow model. So, the first case of modified model turns to Tam's model when turbulent viscosity removes by using the value of variation term $\eta = 0.00$. Consequently, the theoretical red curve for $\eta = 0.0026$ is shown in qualitatively excellent agreement with the RSD experiment [52] where the attenuation of shock-cells significantly follow the experimental properties, while the green curve is calculated from the Emami's original theory for the same values of η where the shock-cells are attenuated

rapidly, and the number of the shock-cells are also overestimated due to the turbulence effects.

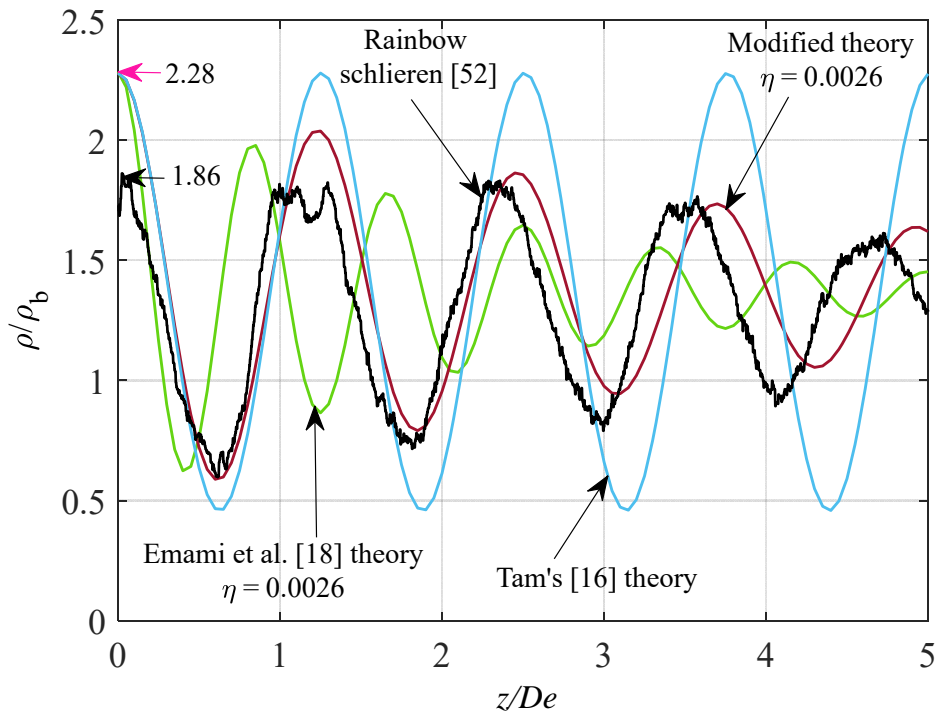


Fig. 3.11: Comparison of theoretical centerline density profiles with experiment [52].

3.5.2.2 Theoretical Density Contour Plot

The theoretical model with explicit solutions of underexpanded jet gives only hypothetical gross results about the specific flow prediction. Yet, it can be used as a comparison to verify the results obtained by the experiments. However, the validity of the simulation should be carefully compared to the geometry of the shock wave specially from the rainbow schlieren deflectometry which is discussed in experimental section. This studied normalized density also helps to gather a thorough ideas about newly unemployed jet flow systems, because near the nozzle exit valid theory can store qualitative density close to experiment. Moreover, there are numerous theories about flow components such as the size and shape of the expansion and compression zones, the spacing of the shock-cells and structures, and the jet boundaries can be known from the theory-based density contours Figures 3.12~3.15 where the flow is acting from left to right. Figure 3.12(a) is illustrated by the RSD data [52] for comparing the modified theoretical results shown in Figs. 3.12(b)~3.12(d) where $NPR = 3.0$, $M_d = 1.0$ and the eigen value expansion first mode, $m = 1$ are considered into the MATLAB script. The specific heat constant, $\gamma = 1.4$ for quiescent air is performed into the convergent-divergent circular cross-section where radius is normalized by the exit diameter, D_e with the effective values $-0.5 \sim 0.5$

units and normalized downstream distance, $z/De = (0\sim 5 \text{ units})$ are deemed.

Figure 3.12(a) is assumed as a standard density distribution referenced from [52] where expansion and compression waves are spaced periodically, and local maxima-minima are decreased gradually along with the downstream direction from the exit, which implies that far distance shocks along the flow direction are less strong than the nearer of nozzle exit, because of back pressure, p_b effects. Sequentially, Figs. 3.12(b) and 3.12(c) are illustrated by the modified theories for $\eta = 0$ and $\eta = 0.0026$ separately where first one obeys vortex sheet model [16] flow features and appearing equally spaced shocks, whereas second one displays qualitatively similar density distribution with Fig. 3.12(a) which is gradually diminishing along with the downstream distance. Also, Fig. 3.12(c) is shown the better density distribution than the Fig. 3.12(d) that is the Emam's [18] original flow distribution where $\eta = 0.0026$ is imposed for qualitative comparison. According to the analysis of Figs. 3.13~3.15, the number of shock-cells are decreased, but the size of shock-cells is increased with increasing the NPR while the design Mach numbers (M_d) must be adjusted with fully expanded jet Mach numbers (M_j), though there has been revealed few inconsistent flow features in the Fig. 3.15(d) under the higher NPR rather than other flow models.

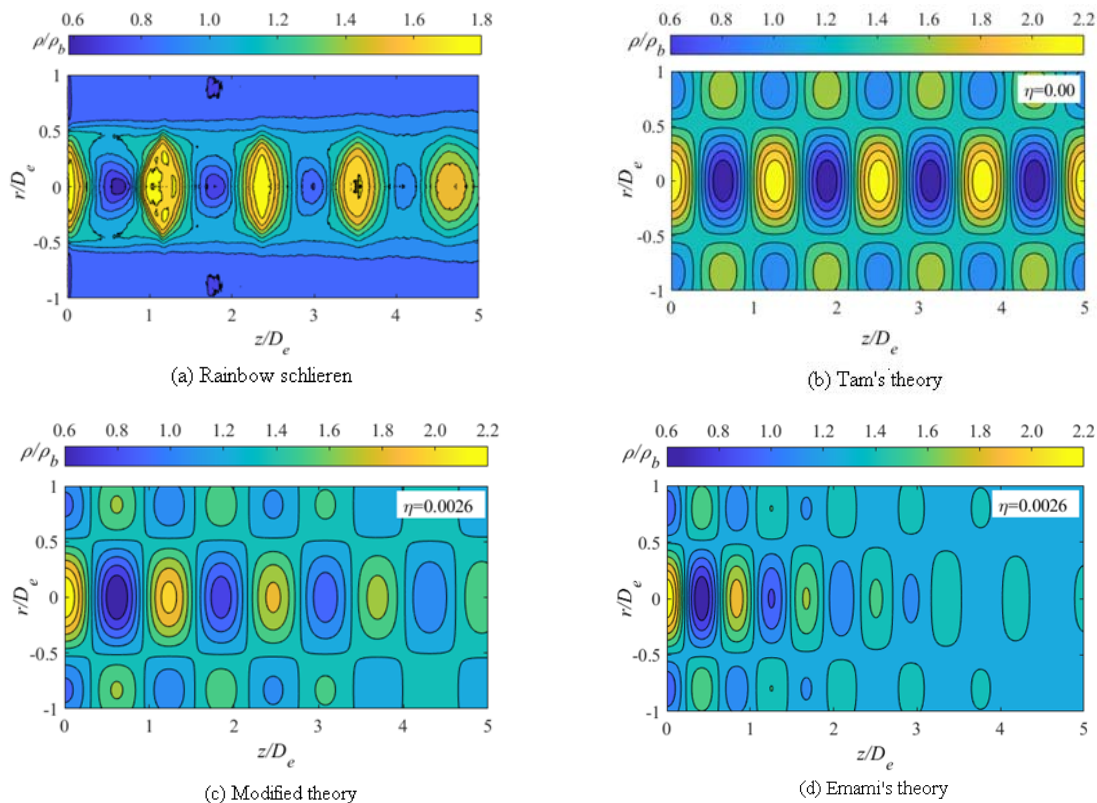


Fig. 3.12: Comparison of theoretical density contours with RSD experiment [52].

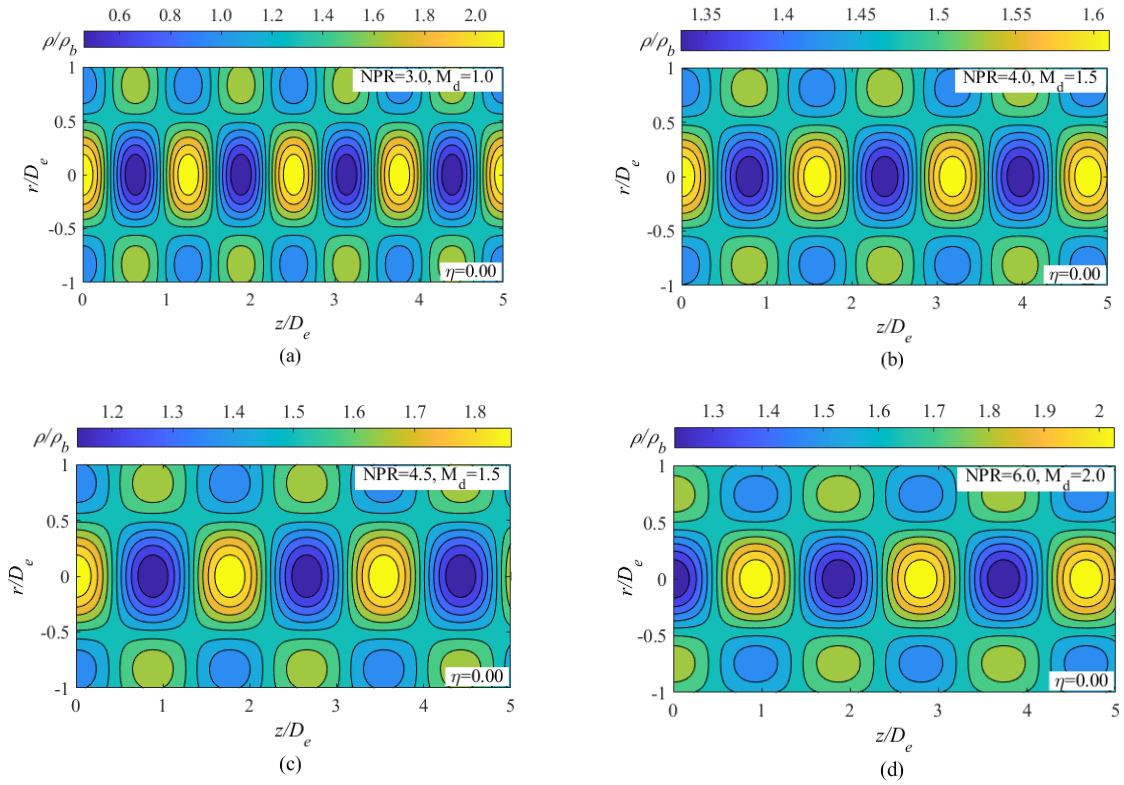


Fig. 3.13: Density contours variation of Tam's theory.

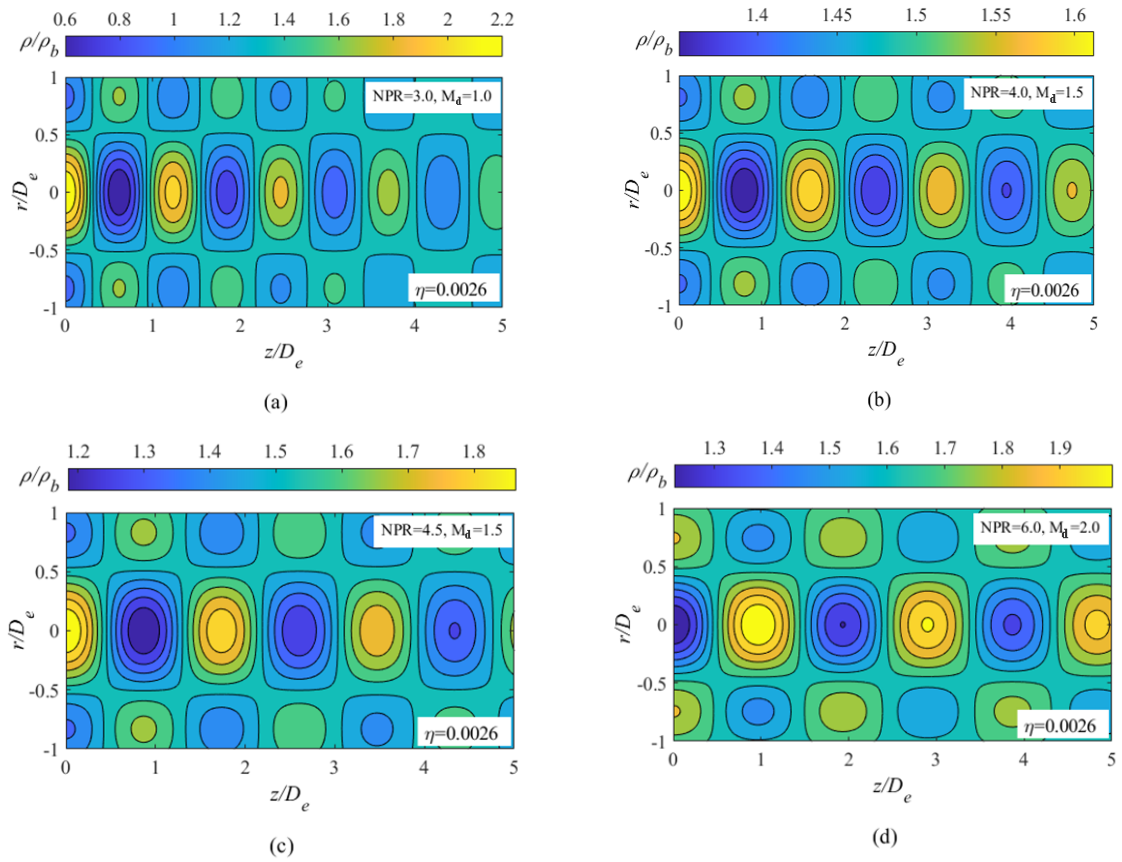


Fig. 3.14: Density contours variation of Modified theory.

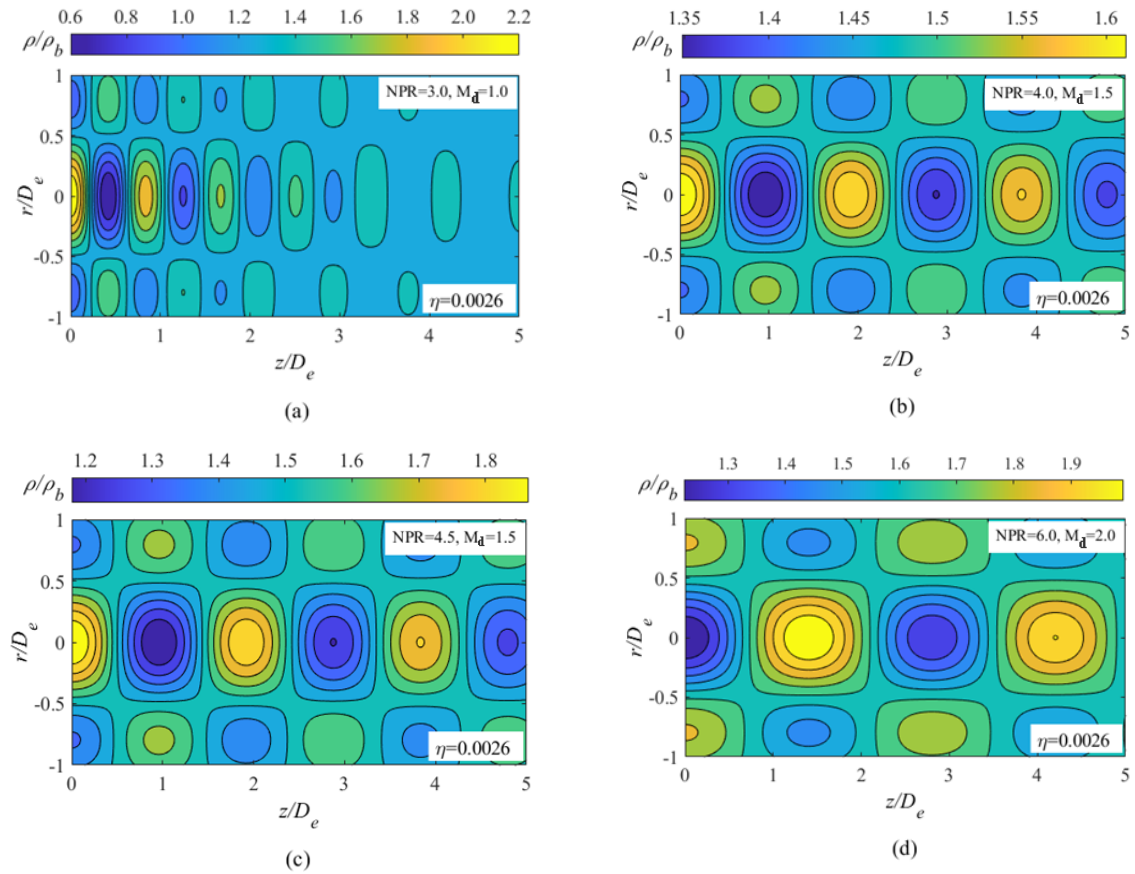


Fig. 3.15: Density contours variation of Emami's theory.

3.5.2.3 Theoretical Density Mesh Plot with Contour

Four distinct density mesh plots with contour plots of axisymmetric underexpanded jet have been illustrated by Figs.3.16(a)~3.16(d) where 3D dimensional jet is appeared with the surface. These types of flow visualization help easily to analysis the shock-cell structures where and how the fluid properties change according to their environments. Fig. 3.16(a) displays rainbow schlieren deflectometry data [52], Fig. 3.16(b) Tam's theory, Fig. 3.16(c) modified theory, and Fig. 3.16(d) Emam's theory where the nozzle pressure ratio, (NPR) of 3.0 and design Mach number, (M_d) of 1.0 are applied. The normalized streamwise distance (z/De), nozzle exits diameter (r/De) and normalized density profile (ρ/ρ_b) are stated by the length, width, and height, respectively. The expansion waves and compression waves of shock cell structures are characterized by the orange and green shapes, each, however the jet boundary based upon the assumption of the underexpanded flow from the inlet of the nozzle to the exit is specified through the shadow blue zone. Only the first mode is considered to describe the fully expanded jet density in the linearized present model with the Tam's [16] and Emami's [18] model

In Fig.3.16(a) demonstrates that the experimental [52] mesh density is gradually diminishes with downstream distance from the nozzle exit on the lower plot, while the state of being is configured by the contour at the upper plot. A three-dimensional schema of first shock-cell structure is built at the first local maximum belonging to the sufficiently minimum value which is underneath the ambient density instead of a progressive increase in the downstream direction. A comparable quasi-periodical expansion and compression waves are repeating itself along the downstream direction with a gradual reduction of the local maxima and minima in the mesh density. Finally, the jet boundary is affected by the ambient pressure when the expanded jet density closes to the ambient density.

In Fig.3.16(b), the inviscid 3D jet distribution exhibits where the effect of turbulent viscosity is neglected upon with the flow characteristics. The resulted mesh pairs with vortex-sheet model have been displayed on the bottom section, while the shock-cell structures are configured at the upper section as a contour plot. The calculated density mesh is agreed with the experimental mesh Fig. 3.16(a) quantitatively. However, the periodicity of the expansion and compression waves have quite variation with the experimental waves, whereas the jet boundary is demarcated hypothetically same as the rainbow schlieren deflectometry.

The fully expanded modified and Emam's density mesh plots are aligned at the bottom layer of Figs. 3.16(c) and 3.16(d) respectively where turbulent viscosity is counted for the same variation term, $\eta = 0.0026$. Nevertheless, the modified mesh in Fig. 3.16(c) point out reasonable improved result than the Emam's one. The effect of shock-cell structure can be measured by the contours which are displayed on the top layer of Figs. 3.16(c) and 3.16(d), where expansion is decreased dramatically after the first shocks in Fig. 3.17(d), whereas the expansions and compressions are occurred in Fig. 3.16(c) similar pattern wise of Fig. 3.16(a) along with the downstream distance started from the exit circular cross-section of convergent-divergent nozzle.

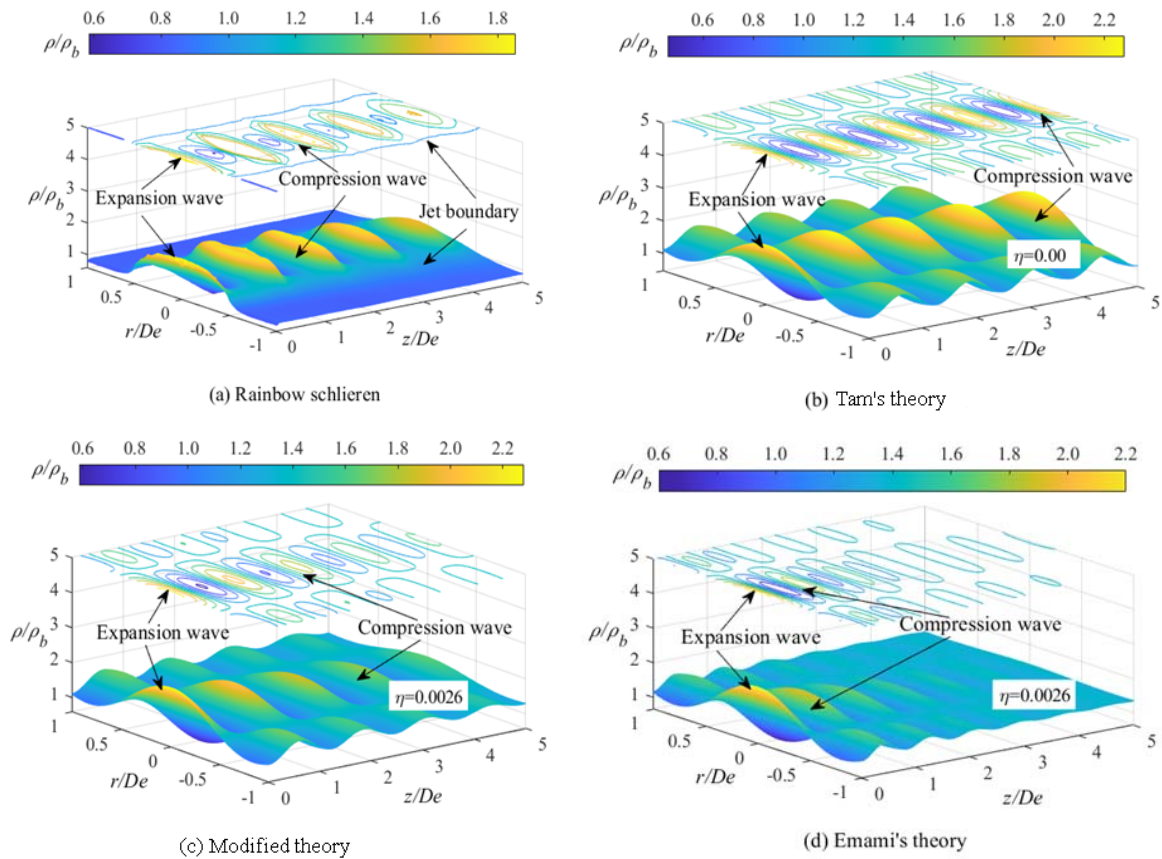


Fig. 3.16: Density Mesh plots with contours underneath of theory with experiment [52].

3.5.2.4 Conclusion Remarks of Theoretical Analysis

The issued slightly underexpanded supersonic jet of convergent-divergent nozzle has been solved explicitly with some modifications of the theoretical model developing through the Emami et al. and Tam's model. The modified model and results are performed qualitatively with experimental data by considering the mean Reynolds stress and the first mode of Fourier expansion. The theoretical density profile along the jet centerline is compared quantitatively with experimental density captured from the rainbow schlieren deflectometry. The obtained normalized mesh density function of axisymmetric fully expanded jet from cylindrical Laval nozzle has been developed and analysed explicitly by employing the modified kinetic and dynamical boundaries for the cases of turbulent viscosity and without viscosity. The modified theoretical results are being forecasted satisfactorily with the experiment and also the renowned vortex-sheet theory of Tam's, especially for the nozzle exit region flow characteristics with complex phenomena.

Chapter 4

Shock Containing Elliptic Jet

4.1 Introduction

Much research on supersonic jets coming out of circular nozzles have been studied already in Chapter 3, to the best of perceptive knowledge, very little investigation has been done on the elliptic nozzle. Elliptical supersonic jets are an encouraging component for efficient blending in air breathing engines to enhance vehicle efficiency [60]. In the off-designed state, the elliptical jet creates a complex impact system in the jet plume, producing a strong noise called screech tone [61]. This plays an important role in advanced aircraft design as it can cause acoustic fatigue failure. Though, the internal shock wave formation of elliptical jets, including shock waves, has not been fully investigated due to its difficulties. Kinzie and McLaughlin [42] were concluded that elliptical jets emit less noise than each circular jet through the experimental investigation of aerodynamic and acoustic properties of impact-free supersonic jets obtained from elliptical and circular nozzles with a design Mach number of 1.5. Menon and Skews [43] have conducted extensive research on the shock wave composition and flow structure of under-propagated sonic jets derived from non-axisymmetric nozzles such as rectangles, ellipses, and slot nozzles. For elliptic underexpanded jets, they experimentally and numerically found that the incident shock generated near the nozzle exit is not formed along the minor axis plane of the nozzle for aspect ratios larger than 2. Instead, it originates downstream from the nozzle exit in the major axis plane. The flow characteristics of underexpanded jets from an elliptic nozzle with a design Mach number and AR of 2 each at the nozzle exit were investigated experimentally by Kumar and Rathakrishnan [8]; they conducted a Pitot probe survey and shadowgraph visualization to demonstrate the streamwise evolution of elliptic jets, such as the

axis-switching phenomena. However, traditional intrusive measuring probes, such as the Pitot tube and hot-wire anemometry, are obstructed by flow intrusion and signal interpretation problems in shock-containing flows. Moreover, the determination of flow properties for many spatial points using intrusive probes requires significant effort. In contrast, Yoon et al. [62] used stereoscopic particle image velocimetry to investigate the near-field structure of an underexpanded jet emerging from a sharp-edged elliptic orifice with an AR of 2. Traditionally, the conventional schlieren and shadowgraph optical techniques [21] provide simple tools to qualitatively investigate the characteristics of shock-dominated flows. Therefore, the primary sources of experimental methods for elliptic supersonic jets include flow visualizations using schlieren [63] or shadowgraph [43] techniques. Recently, Rao et al. [20] utilized time resolved schlieren imaging with near-field acoustic measurements to investigate the screech characteristics of an underexpanded elliptic jet with a high *AR of 7.72*. Although the schlieren technique with a knife edge only presents the qualitative flow features, rainbow schlieren deflectometry, wherein the knife edge is replaced with a rainbow filter [31], can be used to obtain the internal structures of shocks qualitatively and quantitatively.

In this study, the focus is on to investigate the internal flow of supersonic elliptic jets with the modified linearize model addressing in Chapter 3 where the convergent-divergent nozzle is carried out at the off-designed condition, because of so far, the explicit evaluation of the elliptic analytical model is still required to analysis. The established model is modified by the two well-known models of Tam's [17] and Emami et al. [18]. In Tam's [17], a general solution of elliptic jet was provided where the thin layer of inviscid jet specified as vortex sheet through the shock-cell structure measurement theories, but he could not be provided complete solution with validity test. And in Emami's et al. [18], the model was provided the mean flow characteristics of circular jets at the exit level where the turbulent viscosity was estimated by Witz [19] and the first Fourier mode of eigenvalues expansion was implemented. Therefore, the first aim is to develop the governing equations of motion by the elliptic co-ordinates flow surface according to the Chapter 3. Secondly, considering perturbed pressure gradient zero at the center of exit elliptic surface in Tam's [17] boundary conditions instead of velocity condition. Thirdly, providing an explicit solution of this improved model for the case of (i) without and (ii) with turbulent viscosity separately. The explicit solution of first case would be become and obeyed by the behavior of vortex sheet flow model [17] and the solution of second case is explored for the first time. In the result and discussion section, a quantitative comparison among the elliptic centerline density profile along the downstream direction normalized by the

equivalent diameter (D_{eq}) same as the circular exit diameter D_e with the circular experimental [52] and theoretical centerline density of Chapter 3 has been provided for the validity of elliptic results. For the more investigations, the density contour plots and density mesh plots with contours of fully expanded elliptic jets with circular contours have been illustrated through the various effects of the flow parameters. Moreover, the measurements of shock-cell spacing and shock size of fully expanded elliptic jet are also discussed according to their respective theories and graphical explanation where the arbitrary nozzle aspect ratios (ARs), arbitrary nozzle pressure ratios ($NPRs$) and arbitrary nozzle design Mach numbers (M_{aS}) are also considered. It is noted that the shock-cells spacing, and size of shock-cell structures are provided the information about the strength of shock waves which are significantly related to the screech frequencies. Finally, the obtained shock-cell spacing are compared with the result at $AR = 7.72$ of Rao et al. [20] for the betterment of the analysis of fully expanded elliptic jets.

4.2 Elliptic Cylinder Co-ordinates System

For the accessibility of the supersonic elliptic jet analysis, it is clearly significant to discuss the elliptic cylindrical co-ordinates (ξ, θ, z) system [64] where θ be the asymptotic angle of confocal hyperbolic cylinders symmetrical about y -axis and ξ be the co-ordinate of confocal elliptic cylinder centred on the origin are stated in Figs. 4.1(a) and 4.1(b) by,

$$x = a \cosh \xi \cos \theta, \quad y = a \sinh \xi \sin \theta, \quad z = z, \quad (4.1)$$

$$\frac{x^2}{a^2 \cosh^2 \xi} + \frac{y^2}{a^2 \sinh^2 \xi} = 1, \quad (4.2)$$

$$\frac{x^2}{a^2 \cos^2 \theta} - \frac{y^2}{a^2 \sin^2 \theta} = 1. \quad (4.3)$$

A bunch of confocal elliptic curves of major axes ($L_m = a \cosh \xi$) and minor axes ($L_n = a \sinh \xi$) with the common foci $x = \pm a, y = 0$ be presented by Eq. (4.2) are illustrated in Fig. 4.1(b) for the various values of ξ and a set of confocal hyperbolas with the same foci are also presented by Eq. (4.3). Considering the jet is fully developed at $\xi = \xi_j$ as showing in Fig. 4.1 where the major and minor axes of underexpanded elliptic shock-cell is defined by,

$$L_{m_j} = a \cosh \xi_j, \quad L_{n_j} = a \sinh \xi_j. \quad (4.4)$$

$$\text{where, } a = \sqrt{L_{m_j}^2 - L_{n_j}^2}, \quad \xi_j = \tanh^{-1} \left(\frac{L_{n_j}}{L_{m_j}} \right). \quad (4.5)$$

In Fig. 4.1(a), the nozzle outlet is elliptic cross-section where the eccentricity (e) is defined as,

$$e = (a/L_m) = \sqrt{1 - (L_n/L_m)^2} = \sqrt{1 - (1/AR)^2}, \quad (4.6)$$

$$\text{where, } AR = L_m/L_n. \quad (4.7)$$

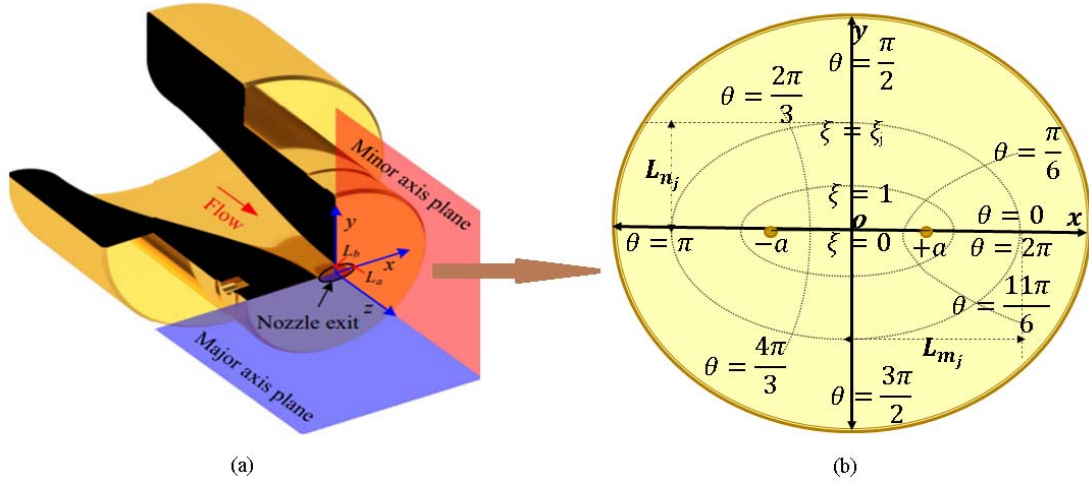


Fig. 4.1: The diagram of (a) an elliptic nozzle with (b) elliptic co-ordinates system.

On the other hand, the nozzle exits cross-sectional surface (S_e) whose equivalent diameter (D_{eq}), and area (A_e) can also be expressed in terms of major axis and minor axis as:

$$D_{eq} \approx 2\sqrt{(L_m L_n)}, \quad A_e \approx \pi(L_m L_n). \quad (4.8)$$

By using the transformation formula of Cartesian coordinates to elliptic cylindrical co-ordinates system [64], then the elliptic coordinates express in terms of Cartesian form as,

$$\xi = \cosh^{-1} \left[\frac{\sqrt{(x+a)^2 + y^2} + \sqrt{(x-a)^2 + y^2}}{2a} \right], \quad (4.9)$$

$$\theta = \cos^{-1} \left[\frac{\sqrt{(x+a)^2 + y^2} - \sqrt{(x-a)^2 + y^2}}{2a} \right], \quad (4.10)$$

$$z = z. \quad (4.11)$$

$$\text{where, } \xi \in [0, \infty), \quad \theta \in [0, 2\pi], \quad \text{and } z \in (-\infty, \infty) \quad (4.12)$$

Again, by using the partial differential transformation formula, the vector differential operator can be transformed into the elliptic Laplacian operator as,

$$\bar{\nabla}^2 = \frac{1}{a^2(\sinh^2 \xi + \sin^2 \theta)} \left(\frac{\partial^2}{\partial \xi^2} + \frac{\partial^2}{\partial \theta^2} \right) + \frac{\partial^2}{\partial z^2}. \quad (4.13)$$

The formulas and properties are pertaining to elliptic membrane experiencing to analyze the problems as dispersion of released fluid, thermal diffusion, electromagnetic wave, and so on which undergoes to the pulsation of the disturbance and intensity of wave.

4.3 Modified Model for Elliptic Jet

In an off-design setup, a slightly underexpanded supersonic elliptic jet issued from a convergent-divergent nozzle shown in Fig. 4.1 where the jet is free from outside disturbance and turbulent eddy viscosity is considered into the modified linearized model described in Chapter 3. Considering the flow is parallel to the axial z -direction of the elliptic nozzle pointing O the center at exit surface, $S_e(x, y)$ whose equivalent diameter (D_{eq}) is shown in the Fig. 4.2(b) where L_m and L_n are the major and minor axes respectively. The mixing layer of jet regarded as the vortex sheet surfaces illustrated as in Fig. 4.2 (a) are being constructed in Cartesian shape for the fully developed jets. As a result, the shock-cell structures are also narrowed to the inside of the vortex sheet. Since the perturbation methods are required in the motion of fluid, so the velocity (V), pressure (p) and density (ρ) can be stated as the sum of mean quantities with perturbed quantities entire the flow field:

$$V_i = \bar{V}_i + dV_i, \bar{V}_z = U_j, \bar{V}_x = \bar{V}_y = 0, p = p_j + dp \text{ and } \rho = \rho_j + d\rho, \quad (4.14)$$

where, the notations dV_i, dp , and $d\rho$ are accustomed to perturbation associated velocity, pressure, and density in the shock-cell structures. Consequently, \bar{V}_i is the mean value of velocities where suffix (i) bearing the x, y, z axes. The fully expanded density, pressure, and velocity are labelled by the notation ρ_j, p_j , and U_j respectively. Therefore, the perturbation relations (4.14) are applied to extend the Navier-Stokes equation through Eqs. (2.35), (2.37), and (2.43) for the following equations of motion:

the equation of continuity, $\rho_j \frac{\partial dV_i}{\partial x_i} + U_j \frac{\partial d\rho}{\partial z} = 0,$ (4.15)

the momentum equation, $\rho_j U_j \frac{\partial dV_i}{\partial z} + \frac{\partial d\rho}{\partial x_i} + \frac{4\mu_t U_j}{3\rho_j} \frac{\partial}{\partial x_i} \left(\frac{\partial d\rho}{\partial z} \right) = 0,$ (4.16)

the isentropic equation, $\frac{dp}{d\rho} = a_j^2,$ (4.17)

where, $(\partial/\partial x_i)$ and a_j represent the vector differential operator and fully expanded speed of sound respectively. In Eq. (4.16), the turbulent viscosity (μ_t) is modified by the fully expanded qualities and measured from the below mentioned formula, since the eddy viscosity remains almost constant over the flow field of high-speed jet, based on this assumption the original formula [19] was explored by the exit characteristics where the variation term, η was 0.01:

$$\mu_t = \eta \rho_b^{0.28} \rho_j^{0.72} U_j D_{eq_j} (1 - 0.16 M_j). \quad (4.18)$$

In Eq. (4.18), the notation η is using for the best data fitting with the RSD experiment of circular jet and D_{eq_j} is the fully expanded equivalent diameter that's major and minor axes dimensions are L_{m_j} and L_{n_j} respectively.

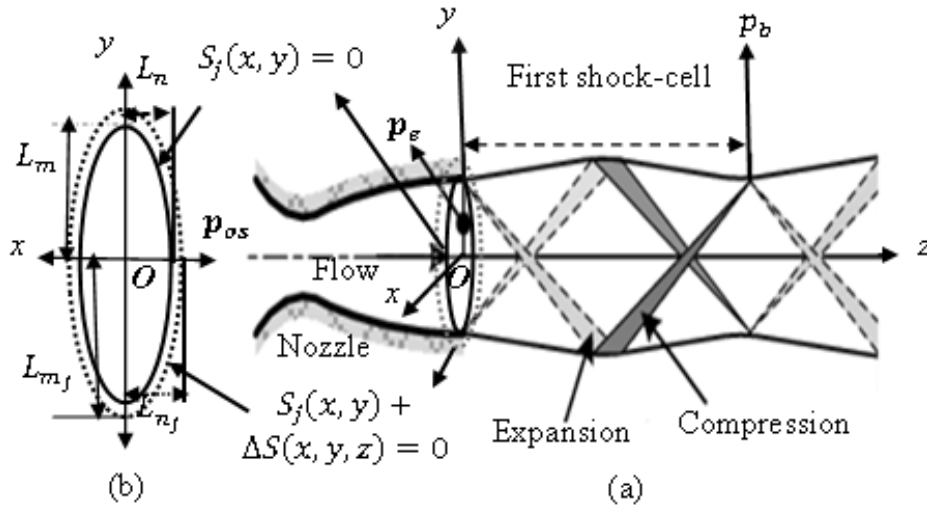


Fig. 4.2: A schematic underexpanded flow of (a) the vortex sheet jets through (b) the elliptic nozzle exit cross-section.

According to the Tam's [17] model, the vortex sheet surface in the Cartesian form $S_j(x, y)$ is bounded by the fully expanded jet where the surface is pertubated by the small change of $\Delta S(x, y, z)$, then the follwing forms are required to:

$$S_j(x, y) = 0, \quad (4.19)$$

$$\text{and } S_j(x, y) + \Delta S(x, y, z) = 0. \quad (4.20)$$

Considering the jet has been fully expanded at $\xi = \xi_j$ where the asymptotic angle, $\theta \in [0, 2\pi]$ and emitted jets features are aslo symmetrical about the flow direction (z), then the Cartesian surface Eq. (4.19) has to convert in elliptic surfac $\Phi_j(\xi, \theta) + \Delta\Phi(z, \xi, \theta)$ whose equivalent diameter is D_{eqj} . According to the kinematic and dynamic conditions of the flow filed are referenced from Tam's [17], the following homogeneous boundaries are constructed in Cartesian form for the requirements of the governing Eqs. (4.15) to (4.17) where the nozzle exit pressure (p_e) is greater than the ambient pressure (p_b):

$$dp = 0, \quad \text{at } S_j(x, y) = 0; \quad (4.21)$$

$$\frac{\partial(dp)}{\partial z} = 0, \quad \text{at } z = 0 \text{ and } S_j(x, y) < 0; \quad (4.22)$$

$$dp = 0, \quad \text{at } z = 0 \text{ and } S_e(x, y) > 0, S_j(x, y) < 0; \quad (4.23)$$

$$dp = \Delta p = p_e - p_b, \quad \text{at } z = 0 \text{ and } S_e(x, y) < 0. \quad (4.24)$$

The condition (4.21) is referred to as the continuity of perturbed pressure at the nozzle exit surface followed by Eq. (4.19). Since the perturbed pressure is uniform inside the surface of Eq. (4.19), so Eq. (4.22) is considerable as a perturbed pressure gradient condition. Also, Eq. (4.23) is formulated where the perturbed pressure is zero between the nozzle exit level up to fully expanded zone, while Eq. (4.24) is established due to the variation of exit and ambient pressure which is valid only for the nozzle inside region.

Since the flow has to experience with the elliptic cross-sectional area, then Eqs. (4.21) ~ (4.24) must convert in elliptic co-ordinate systems which are associated with,

$$dp = 0, \quad \text{at } \Phi_j(\xi, \theta) = 0; \quad (4.25)$$

$$\frac{\partial(dp)}{\partial z} = 0, \quad \text{at } z = 0 \text{ and } \Phi_j(\xi, \theta) < 0; \quad (4.26)$$

$$dp = 0, \quad \text{at } z = 0 \text{ and } \Phi_e(\xi, \theta) > 0, \Phi_j(\xi, \theta) < 0; \quad (4.27)$$

$$dp = \Delta p = p_e - p_b, \quad \text{at } z = 0 \text{ and } \Phi_e(\xi, \theta) < 0. \quad (4.28)$$

Using Eq. (4.17) in Eqs. (4.15) and (4.16), then the followings are found:

$$\rho_j U_j \frac{\partial dV_i}{\partial x_i} + M_j^2 \frac{\partial dp}{\partial z} = 0, \quad (4.29)$$

$$\rho_j U_j \frac{\partial dV_i}{\partial z} + \frac{\partial dp}{\partial x_j} + \frac{4 \mu_t U_j}{3 \rho_j a_j^2} \frac{\partial}{\partial x_j} \left(\frac{\partial dp}{\partial z} \right) = 0, \quad (4.30)$$

$$\text{where, } M_j = \frac{U_j}{a_j}, \quad (4.31)$$

here, M_j is called the fully expanded jet Mach number. Now differentiating Eqs. (4.30) and (4.29) with respect to x_i and z respectively, then the followings are derived as,

$$\rho_j U_j \frac{\partial^2 dV_i}{\partial z \partial x_i} + \frac{\partial^2 dp}{\partial x_i^2} + \frac{4 \mu_t U_j}{3 \rho_j a_j^2} \frac{\partial^2}{\partial x_j^2} \left(\frac{\partial dp}{\partial z} \right) = 0 \quad (4.32)$$

$$\rho_j U_j \frac{\partial^2 dV_i}{\partial x_i \partial z} + M_j^2 \frac{\partial^2 dp}{\partial z^2} = 0. \quad (4.33)$$

By subtracting Eq. (4.32) to (4.33), the perturbed pressure differential equation becomes as,

$$\frac{\partial^2 dp}{\partial x_i^2} + A \frac{\partial^2}{\partial x_j^2} \left(\frac{\partial dp}{\partial z} \right) - M_j^2 \frac{\partial^2 dp}{\partial z^2} = 0, \quad (4.34)$$

$$\text{where, } A = \frac{4 \mu_t U_j}{3 \rho_j a_j^2}. \quad (4.35)$$

Using Eq. (4.13), the Laplacian operator Cartesian form can be transformed to elliptic cylindrical form, because of the nozzle exit is elliptic cross-section, then it is found as,

$$\begin{aligned} A \left[\frac{\partial^3 dp}{\partial z^3} + \frac{1}{a^2 (\sinh^2 \xi + \sin^2 \theta)} \left(\frac{\partial^3 dp}{\partial \xi^2 \partial z} + \frac{\partial^3 dp}{\partial \theta^2 \partial \xi} \right) \right] \\ + \frac{1}{a^2 (\sinh^2 \xi + \sin^2 \theta)} \left(\frac{\partial^2 dp}{\partial \xi^2} + \frac{\partial^2 dp}{\partial \theta^2} \right) + (1 - M_j^2) \frac{\partial^2 dp}{\partial z^2} = 0. \end{aligned} \quad (4.36)$$

Thus, Eq. (4.36) is called the perturbed pressure partial differential equation for the elliptic underexpanded jet. A method of separation of variables for the eigenfunction expansion is applied on Eq. (4.36) to find the explicit solution of the required linearized model. Thus,

considering the following form of perturbed pressure variable in terms of axial distance (z), asymptotic angle (θ), and the confocal elliptic coordinate (ξ) of jet:

$$dp(z, \xi, \theta) = Z(z) \times \Phi(\xi, \theta), \quad (4.37)$$

$$\text{where, } \Phi(\xi, \theta) = \Xi(\xi) \times T(\theta). \quad (4.38)$$

By utilizing Eqs. (4.37) ~ (4.38) in Eq. (4.36), the following form is obtained,

$$\frac{1}{(M_j^2 - 1)a^2(\sinh^2 \xi + \sin^2 \theta)} \left(\frac{\Xi''}{\Xi} + \frac{T''}{T} \right) = \frac{-\frac{A}{(M_j^2 - 1)} Z''' + Z''}{AZ' + Z} = -\lambda^2, \quad (4.39)$$

where, λ is the eigenvalue, and the negative sign indicates that the shock-cells are decaying towards the flow direction from the nozzle exit. Using the first and third part of Eq. (4.39), then the following differential equations have been become,

$$\begin{aligned} \frac{1}{(M_j^2 - 1)a^2(\sinh^2 \xi + \sin^2 \theta)} \left(\frac{\Xi''}{\Xi} + \frac{T''}{T} \right) &= -\lambda^2, \quad (4.40) \\ \Rightarrow \frac{2}{(M_j^2 - 1)a^2(\cosh 2\xi - \cos 2\theta)} \left(\frac{\Xi''}{\Xi} + \frac{T''}{T} \right) &= -\lambda^2, \\ \Rightarrow \frac{\Xi''}{\Xi} + \frac{T''}{T} &= -\frac{(M_j^2 - 1)a^2\lambda^2}{2} (\cosh 2\xi - \cos 2\theta), \\ \therefore -\left[\frac{\Xi''}{\Xi} + \frac{(M_j^2 - 1)a^2\lambda^2}{2} \cosh 2\xi \right] &= \left[\frac{T''}{T} - \frac{(M_j^2 - 1)a^2\lambda^2}{2} \cos 2\theta \right] = -\beta^2. \quad (4.41) \end{aligned}$$

where, β is another eigenvalue which depends on the elliptic surface. Now Eq. (4.41) is the ordinary differential equation of order 2. Using the last two part of Eq. (4.41),

$$\begin{aligned} \frac{T''}{T} - \frac{(M_j^2 - 1)a^2\lambda^2}{2} \cos 2\theta &= -\beta^2. \\ \Rightarrow T''(\theta) + \left[\beta^2 - 2(M_j^2 - 1) \left(\frac{a\lambda}{2} \right)^2 \cos 2\theta \right] T(\theta) &= 0 \\ \therefore T''(\theta) + [\varrho - 2q \cos 2\theta] T(\theta) &= 0. \quad (4.42) \end{aligned}$$

$$\text{where, } \varrho = \beta^2 \text{ and } q = (M_j^2 - 1) \left(\frac{a\lambda}{2} \right)^2. \quad (4.43)$$

Equation (4.42) is called a Mathieu differential equation of angular form referenced by [64]. The solution of Eq. (4.42) is called the angular Mathieu function or periodic Mathieu function which is defined as the sum of cosine series as,

$$ce_{2n}(\theta, q) = \sum_{r=0}^{\infty} A_{2r}^{2n} \cos 2r\theta, \quad \text{where, } n = 0, 1, 2, \dots \quad (4.44)$$

where, the coefficients A_{2r}^{2n} depend on the quantities q and q where r and n indicate the coefficients position and order of the Mathieu function respectively. Eq. (4.44) is also known as even Mathieu function.

Again, using the last two part of Eq. (4.41), then it is given by,

$$\begin{aligned} \frac{\Xi''}{\Xi} + \frac{(M_j^2 - 1)a^2 \lambda^2}{2} \cosh 2\xi &= \beta^2. \\ \Rightarrow \Xi''(\xi) - \left[\beta^2 - 2(M_j^2 - 1) \left(\frac{a\lambda}{2} \right)^2 \cosh 2\xi \right] \Xi(\xi) &= 0. \\ \therefore \Xi''(\xi) - [q - 2q \cosh 2\xi] \Xi(\xi) &= 0. \end{aligned} \quad (4.45)$$

Equation (4.45) is called a modified Mathieu differential equation of radial form linked with [64]. The solution of Eq. (4.45) is called the radial Mathieu function which is defined as the sum of hyperbolic cosine series as,

$$Ce_{2n}(\xi, q) = \sum_{r=0}^{\infty} A_{2r}^{2n} \cosh 2r\xi, \quad \text{where, } n = 0, 1, 2, \dots \quad (4.46)$$

Using Eqs. (4.44) and (4.46), Eq. (4.38) is given by,

$$\Phi(\xi, \theta) = ce_{2n}(\theta, q) \times Ce_{2n}(\xi, q). \quad (4.47)$$

Again, by using the first two terms of Eq. (4.39), the following form is obtained:

$$\frac{-\frac{A}{(M_j^2 - 1)} Z''' + Z''}{AZ' + Z} = -\lambda^2,$$

$$\therefore -\frac{A}{(M_j^2 - 1)} Z''' + Z'' + \lambda^2[AZ' + Z] = 0. \quad (4.48)$$

Equation (4.48) is a third order ordinary differential equation where the term A depends on the turbulent viscosity (μ_t) that play an important rule on the flow model. There are two possible cases have been raised for the $\mu_t = 0$ and $\mu_t \neq 0$ which are described as follows:

Case -I: When $\mu_t = 0$, the jet becomes an inviscid fluid which is free from Reynolds stress. Then flow model is turned into the vortex sheet shock-cell model where is neglecting outside disturbances and molecular interactions. So, Eq. (4.48) is given by

$$Z'' + \lambda^2 Z = 0. \quad (4.49)$$

Equation (4.49) is a second order homogeneous ordinary differential equation with constant coefficient, then its general solution become as,

$$Z(z) = K_1 \cos(\lambda z) + K_2 \sin(\lambda z). \quad (4.50)$$

In Eq. (4.50), the constant K_1 and K_2 must be met up by the boundary conditions. Using Eqs. (4.47) and (4.50), the required general solution is formed as,

$$dp(z, \xi, \theta) = [ce_{2n}(\theta, q)Ce_{2n}(\xi, q)] \times [K_1 \cos(\lambda z) + K_2 \sin(\lambda z)]. \quad (4.51)$$

For the boundary condition (4.25), when $\xi = \xi_j$, $\Phi_j(\xi, \theta) = 0$, then $dp = 0$, Eq. (4.51) is given the information about the zeros of radial Mathieu function by,

$$Ce_{2n}(\xi_j, q) = 0. \quad (4.52)$$

Since the quantity q depends on the eigenvalue λ which conveys the expansion characteristics of jet, then λ is related with the order of Mathieu function n . Then again, the solution of Eq. (4.52) may provide infinite number of roots, then the root of Eq. (4.52) can be expressed as,

$$q_{nm} = \frac{(M_j^2 - 1)a^2 \lambda_{nm}^2}{4}, \quad \text{where, } m = 1, 2, 3 \dots \quad (4.53)$$

In Eq. (4.53), the smallest root is q_{01} . Applying Eq. (4.53) in Eq. (4.51), then it is given by,

$$dp(z, \xi, \theta) = [ce_{2n}(\theta, q_{nm})Ce_{2n}(\xi, q_{nm})] \times [K_1 \cos(\lambda_{nm}z) + K_2 \sin(\lambda_{nm}z)] \quad (4.54)$$

Again, applying the condition (4.26), the perturbed pressure gradient $\partial(dp)/\partial z = 0$, at $z = 0$ and $\Phi_j(\xi, \theta) < 0$, then $K_2 = 0$. So, Eq. (4.54) can be written as,

$$dp(z, \xi, \theta) = K_1 ce_{2n}(\theta, q_{nm})Ce_{2n}(\xi, q_{nm}) \cos(\lambda_{nm}z) \quad (4.55)$$

Now, applying the principles of superposition to express the solution (4.55) as a linear combination of all possible product of eigenfunctions summing over the range of n, m as,

$$dp(z, \xi, \theta) = \sum_{n=0}^{\infty} \sum_{m=1}^{\infty} A_{nm} ce_{2n}(\theta, q_{nm})Ce_{2n}(\xi, q_{nm}) \cos(\lambda_{nm}z) \quad (4.56)$$

It is noted that constant K_1 turns to the constant A_{nm} in the series (4.56). Since all the eigenvalues bear the flow characteristics of jets sequentially, as though fluid particles extend significantly. Finally, Eq. (4.56) is satisfied by the condition (4.28) at the nozzle exit where the perturbed pressure, $\Delta p = p_e - p_b$, at $z = 0$ and inside the surface $\Phi_e(\xi, \theta)$, then followings formula has been derived,

$$dp = \sum_{n=0}^{\infty} \sum_{m=1}^{\infty} A_{nm} ce_{2n}(\theta, q_{nm})Ce_{2n}(\xi, q_{nm}). \quad (4.57)$$

Equation (4.57) is an expansion function where Mathieu function is expanded as a series. The Fourier transform can be applied to find the co-officiant A_{nm} over the elliptic surface $\Phi_j(\xi, \theta)$ where ξ is varied with $(0 \sim \xi_j)$ and θ varied with $[0, 2\pi]$. Applying the Fourier orthogonal properties on Eq. (4.57), the Fourier coefficient A_{nm} can be formulated as,

$$A_{nm} = \frac{\iint_{\Phi_j} dp \times [ce_{2n}(\theta, q_{nm})Ce_{2n}(\xi, q_{nm})] |J| d\xi d\theta}{\iint_{\Phi_j} [ce_{2n}(\theta, q_{nm})Ce_{2n}(\xi, q_{nm})]^2 |J| d\xi d\theta}. \quad (4.58)$$

The quantity dp is required by the boundary conditions (4.27) and (4.28) and $|J|$ is the Jacobian of elliptic co-ordinates system that is associated with:

$$|J| = \frac{a^2}{2} (\cosh 2\xi - \cos 2\theta). \quad (4.59)$$

Using Eqs. (4.27) and (4.28) in Eq. (4.58), the required value of A_{nm} is formulated by,

$$A_{nm} = 2\Delta p \times \alpha_{nm}. \quad (4.60)$$

$$\text{where, } \alpha_{nm} = \frac{\int_0^{\xi_e} \int_0^{2\pi} C e_{2n}(\xi, q_{nm}) c e_{2n}(\theta, q_{nm}) (\cosh 2\xi - \cos 2\theta) d\xi d\theta}{2 \int_0^{\xi_j} \int_0^{2\pi} C e_{2n}^2(\xi, q_{nm}) c e_{2n}^2(\theta, q_{nm}) (\cosh 2\xi - \cos 2\theta) d\xi d\theta}, \quad (4.61)$$

$$\text{and, } \xi_e = \tanh^{-1}\left(\frac{1}{AR}\right). \quad (4.62)$$

To evaluate the coefficient α_{nm} , the below assumptions are desired:

$$\int_0^{2\pi} c e_{2n}(\theta, q_{nm}) d\theta = 2\pi A_0^{2n}. \quad (4.63)$$

$$\int_0^{2\pi} c e_{2n}^2(\theta, q_{nm}) d\theta = \pi \left[2(A_0^{2n})^2 + \sum_{r=1}^{\infty} (A_{2r}^{2n})^2 \right]. \quad (4.64)$$

$$\int_0^{2\pi} c e_{2n}(\theta, q_{nm}) \cos 2\theta d\theta = \pi A_2^{2n}. \quad (4.65)$$

$$\int_0^{2\pi} c e_{2n}^2(\theta, q_{nm}) \cos 2\theta d\theta = \pi \left[A_0^{2n} A_2^{2n} + \sum_{r=0}^{\infty} A_{2r}^{2n} A_{2r+2}^{2n} \right]. \quad (4.67)$$

$$\int_0^{\xi_e} C e_{2n}(\xi, q_{nm}) d\xi = \xi_e A_0^{2n} + \sum_{r=1}^{\infty} \frac{A_{2r}^{2n}}{2r} \sinh(2r\xi_e). \quad (4.68)$$

$$\begin{aligned} & \int_0^{\xi_e} C e_{2n}(\xi, q_{nm}) \cosh 2\xi d\xi \\ &= \frac{1}{2} A_2^{2n} + \frac{1}{4} A_0^{2n} \sinh 2\xi_e + \frac{1}{4} \sum_{r=1}^{\infty} \frac{1}{r} (A_{2r+2}^{2n} + A_{2r-2}^{2n}) \sinh(2r\xi_e). \end{aligned} \quad (4.69)$$

By contrast, the integrations $\int_0^{\xi_j} C e_{2n}^2(\xi, q_{nm}) d\xi$ and $\int_0^{\xi_j} C e_{2n}^2(\xi, q_{nm}) \cosh 2\xi d\xi$ have been evaluated by applying the numerical techniques where the maximum 25 eigen vectors coefficients of Mathieu function are taken in the MATLAB script to compute the coefficient A_{nm} . Consequently, according to the orthogonal normalization of angular Mathieu function referenced by [64], Eq. (4.64) can be written as,

$$\int_0^{2\pi} c e_{2n}^2(\theta, q_{nm}) d\theta = \pi. \quad (4.70)$$

$$\text{where, } \left[2(A_0^{2n})^2 + \sum_{r=1}^{\infty} (A_{2r}^{2n})^2 \right] = 1. \quad (4.71)$$

The value of normalization Eq. (4.70), $(\pi/\sqrt{2})$ is convenient for the angular Mathieu functions over the interval $[0, 2\pi]$ which is addressed by McLachlan [64].

By using Eqs. (4.56), and (4.60), the required solution of Eq. (4.36) becomes,

$$dp(z, \xi, \theta) = \sum_{n=0}^{\infty} \sum_{m=1}^{\infty} 2\Delta p \alpha_{nm} c e_{2n}(\theta, q_{nm}) C e_{2n}(\xi, q_{nm}) \cos(\lambda_{nm} z). \quad (4.72)$$

Equation (4.72) is the complete solution of Eq. (4.36) for the **Case-I** where the turbulent viscosity $\mu_t = 0$. Putting the value of Eq. (4.72) in the pressure term of Eq. (4.14), then the total pressure becomes as,

$$\begin{aligned} p &= p_j + \sum_{n=0}^{\infty} \sum_{m=1}^{\infty} 2\Delta p \alpha_{nm} c e_{2n}(\theta, q_{nm}) C e_{2n}(\xi, q_{nm}) \cos(\lambda_{nm} z). \\ \Rightarrow p &= p_j + 2(p_e - p_b) \sum_{n=0}^{\infty} \sum_{m=1}^{\infty} \alpha_{nm} c e_{2n}(\theta, q_{nm}) C e_{2n}(\xi, q_{nm}) \cos(\lambda_{nm} z). \\ \therefore \frac{p}{p_j} &= 1 + 2 \left(\frac{p_e}{p_j} - \frac{p_b}{p_j} \right) \sum_{n=0}^{\infty} \sum_{m=1}^{\infty} \alpha_{nm} c e_{2n}(\theta, q_{nm}) C e_{2n}(\xi, q_{nm}) \cos(\lambda_{nm} z). \end{aligned} \quad (4.73)$$

Since the tendency of fully expanded pressure has to make balance with ambient pressure, then the ratio of (p/p_j) is equal to the ratio (p/p_b) . In mathematically,

$$\frac{p}{p_j} = \frac{p}{p_b} \quad (4.74)$$

Therefore, Eq. (4.73) becomes as the following required explicit form of normalized pressure,

$$\frac{p}{p_b} = 1 + 2 \left(\frac{p_e}{p_b} - 1 \right) \sum_{n=0}^{\infty} \sum_{m=1}^{\infty} \alpha_{nm} c e_{2n}(\theta, q_{nm}) C e_{2n}(\xi, q_{nm}) \cos(\lambda_{nm} z). \quad (4.75)$$

Again, the density of underexpanded jet can also be measured from the pressure equation (4.75). Applying Eq. (2.69) where the pressure and density are related as,

$$\frac{p}{p_j} = \frac{p}{p_b} = \left(\frac{\rho}{\rho_j} \right)^\gamma, \quad (4.76)$$

The symbol γ is the specific heat ratio and the extended density is differed from the ambient density, *i. e* $\rho_j \neq \rho_b$, then Eq. (4.75) turns to,

$$\frac{\rho}{\rho_j} = 1 + \frac{2}{\gamma} \left(\frac{p_e}{p_b} - 1 \right) \times d\rho_{ell}(z, \xi, \theta), \quad (4.77)$$

$$\text{where, } d\rho_{ell}(z, \xi, \theta) = \sum_{n=0}^{\infty} \sum_{m=1}^{\infty} \alpha_{nm} c e_{2n}(\theta, q_{nm}) C e_{2n}(\xi, q_{nm}) \cos(\lambda_{nm} z). \quad (4.78)$$

But Eq. (4.77) can be rearranged as,

$$\rho = \rho_j \left[1 + \frac{2}{\gamma} \left(\frac{p_e}{p_0} \times NPR - 1 \right) \times d\rho_{ell}(z, \xi, \theta) \right]. \quad (4.79)$$

In Eq. (4.79), $NPR = (p_0/p_b)$ is called nozzle pressure ratio between the stagnation pressure (p_0) to ambient pressure (p_b). Using Eqs. (3.57) ~ (3.62) in Chapter 3, Eq. (4.79) becomes,

$$\frac{\rho}{\rho_b} = NPR^{\frac{\gamma-1}{\gamma}} \left[1 + \frac{2}{\gamma} \left(\frac{p_e}{p_0} \times NPR - 1 \right) \times d\rho_{ell}(z, \xi, \theta) \right], \quad (4.80)$$

which is the normalized density profile of the modified model for elliptic shock containing jet.

Therefore, the theoretical pressure and density prediction of fully expanded inviscid jet can be performed by Eqs. (4.75) and (4.80) respectively where AR , NPR , M_e , and γ have to be considered as the preassigned parameter. which are already presented as a proceeding [65].

Case-II: When $\mu_t \neq 0$, implies that the turbulent viscosity has to consider in the flow of jet and Eq. (4.48) is remain unchanged. To find the explicit solution of underexpanded elliptic jet for the **Case-II** where coefficient $A \neq 0$, Eq. (4.48) can be rearranged by,

$$Z'''' - \left(\frac{M_j^2 - 1}{A} \right) Z'' - (M_j^2 - 1) \lambda^2 Z' - \left(\frac{M_j^2 - 1}{A} \right) \lambda^2 Z = 0, \quad (4.81)$$

Equation (4.81) is a third order homogeneous ordinary differential equation with constant coefficient. Now, for a trial solution $Z(z) = e^{\sigma z}$, the characteristics equation is given by,

$$\sigma^3 - \left(\frac{M_j^2 - 1}{A}\right)\sigma^2 - (M_j^2 - 1)\lambda^2\sigma - \left(\frac{M_j^2 - 1}{A}\right)\lambda^2 = 0. \quad (4.82)$$

Equation (4.82) is a third-degree polynomial that has three roots. Due to the Descartes' rule of signs for Eq. (4.82) where no change of sign has been occurred two times and change of sign occurred one time, so there has one real root and two complex roots. The well-known Cardano's formula is applied to solve Eq. (4.82), then considering a general form of polynomial of degree three is given by

$$\sigma^3 + a_1\sigma^2 + a_2\sigma + a_3 = 0, \quad (4.83)$$

where, Eq. (4.82) and Eq. (4.83) are identical. According to the Cardano's formula, three roots R_1, R_2 , and R_3 of Eq. (4.83) can be written as,

$$R_1 = P + Q - \frac{a_1}{3}, R_2 = -\frac{1}{2}(P + Q) - \frac{a_1}{3} + i\frac{\sqrt{3}}{2}(P - Q), \quad (4.84)$$

$$R_3 = -\frac{1}{2}(P + Q) - \frac{a_1}{3} - i\frac{\sqrt{3}}{2}(P - Q),$$

In Eq. (4.84), the used symbols P and Q are real numbers, whereas i is the complex number. The coefficient a_1, a_2 , and a_3 are bear the following values,

$$a_1 = -\frac{M_j^2 - 1}{A}, \quad a_2 = -(M_j^2 - 1)\lambda^2, \quad a_3 = -\left(\frac{M_j^2 - 1}{A}\right)\lambda^2. \quad (4.85)$$

Also, the real P and Q in Eq. (4.84) holds the following formula to make the meaningful roots of Eq. (4.83) as,

$$P = \sqrt[3]{\Omega + \sqrt{\Psi^3 + \Omega^2}}, \quad Q = \sqrt[3]{\Omega - \sqrt{\Psi^3 + \Omega^2}}, \quad (4.86)$$

where, the quantities Ψ and Ω bear the below formulas are given by

$$\Psi = (3a_2 - a_1^2)/9, \quad \Omega = (9a_1a_2 - 7a_3 - 2a_1^3)/54. \quad (4.87)$$

The general solution of Eq. (4.81) can be written with the three R_1 , R_2 and R_3 characteristics roots of the indicial Eq. (4.82) as,

$$\begin{aligned} Z(z) &= K_3 e^{R_1 z} + K_1 e^{R_2 z} + K_2 e^{R_3 z} \quad (4.88) \\ \Rightarrow Z(z) &= K_3 e^{\left(P+Q-\frac{a_1}{3}\right)z} + K_1 e^{\left(-\frac{1}{2}(P+Q)-\frac{a_1}{3}+i\frac{\sqrt{3}}{2}(P-Q)\right)z} + K_2 e^{\left(-\frac{1}{2}(P+Q)-\frac{a_1}{3}-i\frac{\sqrt{3}}{2}(P-Q)\right)z}, \\ \therefore Z(z) &= K_3 e^{\left(P+Q-\frac{a_1}{3}\right)z} + e^{-\left[\frac{1}{2}(P+Q)+\frac{a_1}{3}\right]z} \left\{ K_1 e^{i\frac{\sqrt{3}}{2}(P-Q)z} + K_2 e^{-i\frac{\sqrt{3}}{2}(P-Q)z} \right\}. \quad (4.89) \end{aligned}$$

Since the postulation of isentropic flow is deemed the wave equation where damped oscillation has to demand by the system. Omitting the term with arbitrary constant K_3 , the asking solution (4.89) can be written with other two arbitrary constants K_1 and K_2 as,

$$Z(z) = e^{-\left[\frac{1}{2}(P+Q)+\frac{a_1}{3}\right]z} \left\{ K_1 e^{i\frac{\sqrt{3}}{2}(P-Q)z} + K_2 e^{-i\frac{\sqrt{3}}{2}(P-Q)z} \right\}. \quad (4.90)$$

The rearranging form of Eq. (4.90) yields the general solution of Eq. (4.81) is given by

$$Z(z) = e^{-\varphi z} \{ K_1 \cos(\omega z) + K_2 \sin(\omega z) \}, \quad (4.91)$$

$$\varphi = \left[\frac{1}{2}(P+Q) + \frac{a_1}{3} \right], \quad \omega = \frac{\sqrt{3}}{2}(P-Q). \quad (4.92)$$

Using Eqs. (4.37), (4.47), and (4.91), the general solution of Eq. (4.36) is written as,

$$dp(z, \xi, \theta) = [c e_{2n}(\theta, q) C e_{2n}(\xi, q)] \times e^{-\varphi z} \{ K_1 \cos(\omega z) + K_2 \sin(\omega z) \}. \quad (4.93)$$

Using Eqs. (4.52) and (4.53) which are derived by utilizing Eq. (4.25), Eq. (4.93) is given by,

$$dp(z, \xi, \theta) = [c e_{2n}(\theta, q_{nm}) C e_{2n}(\xi, q_{nm})] e^{-\varphi_{nm} z} [K_1 \cos(\omega_{nm} z) + K_2 \sin(\omega_{nm} z)] \quad (4.94)$$

In Eq. (4.95), φ_{nm} and ω_{nm} depends on the eigenvalues λ_{nm} which is applicable in Eq. (4.81). Again, applying the condition (4.26) in Eq. (4.94), Eq. (4.94) is simplified by,

$$dp = K_1 c e_{2n}(\theta, q_{nm}) C e_{2n}(\xi, q_{nm}) e^{-\varphi_{nm} z} \left[\cos(\omega_{nm} z) + \frac{\varphi_{nm}}{\omega_{nm}} \sin(\omega_{nm} z) \right] \quad (4.95)$$

Now, applying the principles of superposition to express the solution (4.95) as a linear combination of all possible product of eigenfunctions summing over the range of n, m as,

$$dp = \sum_{n=0}^{\infty} \sum_{m=1}^{\infty} A_{nm} c e_{2n}(\theta, q_{nm}) C e_{2n}(\xi, q_{nm}) \times e^{-\varphi_{nm}z} \left[\cos(\omega_{nm}z) + \frac{\varphi_{nm}}{\omega_{nm}} \sin(\omega_{nm}z) \right] \quad (4.96)$$

Finally, Eq. (4.96) is satisfied by the condition (4.28), then the following complete solution of Eq. (4.36) is obtained by using Eqs. (4.57) ~ (4.71),

$$dp(z, \xi, \theta) = \sum_{n=0}^{\infty} \sum_{m=1}^{\infty} 2\Delta p \alpha_{nm} c e_{2n}(\theta, q_{nm}) C e_{2n}(\xi, q_{nm}) \times e^{-\varphi_{nm}z} \left[\cos(\omega_{nm}z) + \frac{\varphi_{nm}}{\omega_{nm}} \sin(\omega_{nm}z) \right]. \quad (4.97)$$

Using Eqs. (4.73) and (4.74), Eq. (4.97) can be written as,

$$\frac{p}{p_b} = 1 + 2 \left(\frac{p_e}{p_b} - 1 \right) \sum_{n=0}^{\infty} \sum_{m=1}^{\infty} \alpha_{nm} c e_{2n}(\theta, q_{nm}) C e_{2n}(\xi, q_{nm}) \times e^{-\varphi_{nm}z} \left[\cos(\omega_{nm}z) + \frac{\varphi_{nm}}{\omega_{nm}} \sin(\omega_{nm}z) \right], \quad (4.98)$$

where, α_{nm} is measured from Eq. (4.61). Thus, Eq. (4.98) is the required explicit normalized pressure profile for the modified elliptic model where turbulent viscosity is utilized.

Finally, applying Eqs. (4.76) ~ (4.80), the explicit viscous normalized density is derived as,

$$\frac{\rho}{\rho_b} = NPR^{\frac{\gamma-1}{\gamma}} \left[1 + \frac{2}{\gamma} \left(\frac{p_e}{p_0} \times NPR - 1 \right) \times d\rho_{ell}(z, \xi, \theta) \right], \quad (4.99)$$

where,

$$d\rho_{ell} = \sum_{n=0}^{\infty} \sum_{m=1}^{\infty} \alpha_{nm} c e_{2n}(\theta, q_{nm}) C e_{2n}(\xi, q_{nm}) \times e^{-\varphi_{nm}z} \left[\cos(\omega_{nm}z) + \frac{\varphi_{nm}}{\omega_{nm}} \sin(\omega_{nm}z) \right] \quad (4.100)$$

Consequently, the normalized pressure and density profile of fully expanded turbulent viscous elliptic jet has been analyzed by Eqs. (4.98) and (4.99) respectively. Then using the Eq. (4.35), the following formulas are required,

$$A/D_{eq} = \frac{4}{3} \times \left(\frac{U_j^2}{a_j^2} \right) / \left(\frac{U_j \rho_j D_{eq}}{\mu_t} \right) = \frac{(4/3) \times M_j^2}{R_{ed}}, \quad (4.101)$$

$$\text{where, } R_{ed} = U_j \rho_j D_{eq} / \mu_t \quad (4.102)$$

Now applying Eq. (4.18) in Eq. (4.102), the modified Reynolds number (R_{ed}) becomes as,

$$R_{ed} = \frac{(D_{eq}/D_{eqj}) \times (\rho_j/\rho_b)^{0.28}}{\eta(1 - 0.16M_j)} \quad (4.103)$$

From Eqs. (4.103) and (4.101), the quantity A is normalized by equivalent diameter D_{eq} as,

$$A/D_{eq} = \left(\frac{4\eta}{3} \right) \times \frac{M_j^2(1 - 0.16M_j)}{(\rho_j/\rho_b)^{0.28} (D_{eq}/D_{eqj})}, \quad (4.104)$$

$$\text{where, } \therefore \frac{D_{eq}}{D_{eqj}} = \sqrt{\frac{M_j \left[(\gamma - 1) M_e^2 + 2 \right]^{\frac{\gamma+1}{2(\gamma-1)}}}{M_e \left[(\gamma - 1) M_j^2 + 2 \right]}}. \quad (4.105)$$

Also, using Eq. (4.85), the normalized coefficients are given by,

$$a_1 = -\frac{M_j^2 - 1}{A/D_{eq}}, \quad a_2 = -\frac{4q_{nm}}{(a/D_{eq})^2}, \quad a_3 = -\frac{4q_{nm}}{(a/D_{eq})^2} / (A/D_{eq}) \quad (4.106)$$

Therefore, the modified pressure and density prediction of fully expanded viscous jet can be performed by Eqs. (4.98) and (4.99) respectively. Centre line measures and mesh contours of pressure and density can also be demonstrated through these assumptions where AR, NPR, M_d , and γ have to be considered as the preassigned parameter.

4.4 Shock-cell Spacing

It is truism that the shock-cell spaces of waves or preiodic structures depend on the smallest eigenvalue of the corresponding phenomenas related with pulsation. Using the smallest root (q_{01}) of Eq. (4.53), the smallest eigenvalue (λ_{01}) is associated by

$$\lambda_{01} = \frac{(2\sqrt{q_{01}})}{a\sqrt{M_j^2 - 1}} \quad (4.107)$$

According to the Tam's [17] model, the shock-cell spacing (L_S) is defined as

$$L_S = \frac{2\pi}{\text{Smallest Eigenvalue}} = \left(\pi a \sqrt{M_j^2 - 1} \right) / \sqrt{q_{01}} \quad (4.108)$$

The shock-cell spacing can be normalized by the equivalent diameter (D_{eq}) of the nozzle exit. Then Eq. (4.108) is simplified as,

$$\frac{L_S}{D_{eq}} = \pi \sqrt{M_j^2 - 1} \left(\frac{a}{D_{eq} \sqrt{q_{01}}} \right), \quad (4.109)$$

$$\text{where, } \frac{a}{D_{eq}} = \frac{a}{L_{m_j}} \times \frac{L_{m_j}}{D_{eq}}. \quad (4.110)$$

The following useful postulates of estimation zeros (q_{01}) of Eq. (4.53) depend on the *AR* of the elliptic nozzle exit cross-section which have been carried out theoretically by evaluating the distinct scales eccentricities and the coordinate ξ_j integrated with Eqs. (4.5) ~ (4.7):

Postulate-I: When $L_{n_j}/L_{m_j} \approx 1$ that impls small q and large ξ_j and the following asymptotical formula in Mores and Feshbach,[66] is considered to evaluate the quantity q_{01} :

$$\sqrt{q_{01}} \approx 1.2025e_j(1 + 0.250e_j), \quad e_j = \frac{a}{L_{m_j}}. \quad (4.111)$$

Using Eq. (4.5) ~ (4.7) and (4.111), the required normalized shock-cell spacing that is almost equal to a jet with circular shape is given by,

$$\frac{L_S}{D_{eq}} \approx \frac{0.8316\pi\sqrt{M_j^2 - 1}}{1 + 0.125e} \times \frac{L_{m_j}}{D_{eq}}. \quad (4.112)$$

Postulate-II: When $L_{n_j}/L_{m_j} \approx 0$, then the appeared large q and small ξ_j can be measured by expandin Eq. (4.5) which are expressed as

$$\frac{a}{L_{m_j}} \approx 1 - \frac{1}{2}\left(\frac{L_{n_j}}{L_{m_j}}\right)^2, \quad \xi_j \approx \left(\frac{L_{n_j}}{L_{m_j}}\right) + \frac{1}{3}\left(\frac{L_{n_j}}{L_{m_j}}\right)^3. \quad (4.113)$$

The following asymptotic formula for large q is provided by McLachlan [64]:

$$C e_j(\xi, q) \approx C_j \sqrt{2/\cosh\xi} \times \cos\left[2\sqrt{q_{0m}} \sinh\mu - \tan^{-1}\left(\frac{\tanh\mu}{2}\right)\right]. \quad (4.114)$$

The first zero of Eq. (4.53) can be calculated by setting the cosine function (C_j) equal to $(\pi/2)$ and small ξ_j in Eq. (4.114) that can be shown as

$$\sqrt{q_{01}} \approx \left(\frac{\pi}{4\xi_j} + \frac{1}{4}\right). \quad (4.115)$$

In this case, using Eqs. (4.115) and (4.109) where neglecting the higher power of (L_{n_j}/L_{m_j}) , the normalized shock-cell spacing which is equivalent for rectangular jets is given by,

$$\frac{L_S}{D_{eq}} \approx \frac{4\sqrt{M_j^2 - 1}}{\left(\frac{L_{m_j}}{L_{n_j}} + \frac{1}{\pi}\right)} \times \frac{L_{m_j}}{D_{eq}}. \quad (4.116)$$

where,

$$\frac{L_{m_j}}{D_{eq}} = \sqrt{\left(\frac{L_{m_j}}{L_m} \times \frac{L_{n_j}}{L_n}\right) / 4 \left(L_{n_j}/L_{m_j}\right)}. \quad (4.117)$$

Finally, all other cases of (L_{n_j}/L_{m_j}) are generally accepted to compute the normalized shock-cell spacing through the Eq. (4.109) and (4.5).

A theoretical consequential parameter $\left(\frac{a}{D_{eq}\sqrt{q_{01}}}\right)$ of Eq. (4.109) depends on the NPR, M_d and AR . The effect of this parameter has been shown in Fig. 4.3 for several values of

AR against the arbitrary NPR with the corresponding values of M_d specified by the condition (3.59). The vertical red bar at $NPR = 2.23$ and blue bar at $NPR = 5.77$ are indicated the barrier satisfying by the condition (3.59) which is directly allied with the shock-cell spacing.

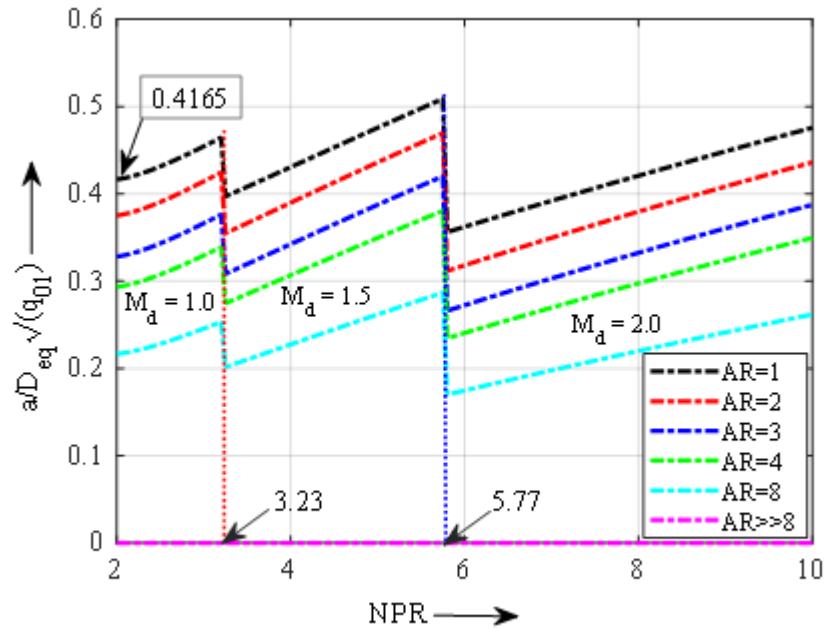


Fig. 4.3: The parametric effects of shock-cell spacing for arbitrary NPR with several AR .

4.5 Size of Fully Expanded Jets

Since the shape and size of the jet resulting from the high-speed jet flow closely depends on the nozzle structure, the difference between fully expanded and the nozzle exit jet size observed is clearly understood through the work [9]. Due to which, in describing the critical flow area where the velocity of jet equal to the critical speed of sound, Chapter 2 is already introduced the following relation between the Mach number M and the critical area ratio A/A^* :

$$\left(\frac{A}{A^*}\right)^2 = \frac{1}{M^2} \left[\frac{2}{\gamma + 1} \left(1 + \frac{\gamma + 1}{2} M^2 \right) \right]^{\frac{\gamma + 1}{\gamma - 1}}, \quad (4.118)$$

where, A^* termed the critical flow area same as the throat of the convergent divergent nozzle working system. Applying the rule (4.118) to the elliptic nozzle exit area (A_e) with the exit Mach number (M_e) and the fully expanded jet area (A_j) with the fully expanded Mach number (M_j), then the elliptic area ratio (A_j/A_e) in Fig. 4.4 is formed by

$$\left(\frac{A_j}{A_e}\right)^2 = \frac{M_e^2}{M_j^2} \left[\left(1 + \frac{1-\gamma}{2} M_j^2\right) / \left(1 + \frac{1-\gamma}{2} M_e^2\right) \right]^{\frac{\gamma+1}{\gamma-1}} \quad (4.119)$$

Due to Fig. 4.4, the perimeter l and major axis (L_m) at the nozzle exit can be expressed as

$$(l\Delta L/2) \approx (A_j - A_e) \quad (4.120)$$

$$L_m = L_{mj} - \Delta L, \quad (4.121)$$

where, the used symbol ΔL is the length increment between the characteristics length of nozzle exit major axis L_m and fully expanded jets major axis (L_{mj}) respectively. Also, considering that the shape size of all the emitted jets is almost similar based on Fig. 4.4; hence, the following required form is to estimate by combing Eq. (4.115) and (4.121):

$$\begin{aligned} \left(\frac{L_{mj}}{L_m}\right) &= 1 + \frac{\Delta L}{L_m} = 1 + \frac{2(A_j - A_e)}{l \times L_m} = 1 + \frac{2A_e \left(\frac{A_j}{A_e} - 1\right)}{l \times L_m} \\ \therefore \frac{L_{mj}}{L_m} &= \left(\frac{A_j}{A_e} - 1\right) \times \left(\frac{2A_e}{l \times L_m}\right) + 1. \end{aligned} \quad (4.122)$$

If the area of the elliptic nozzle exit is adjusting with Eq. (4.8), then the perimeter (l) can be expressed with the complete elliptic integral of second kind as,

$$l = 4L_m \int_0^{\frac{\pi}{2}} \sqrt{1 - e^2 \sin^2 \theta} d\theta \quad (4.123)$$

where, e is the eccentricity of the nozzle exit is measured from Eq. (4.6). Thus, the approximated size of fully expanded elliptic jets major axis wise can be able to measure through Eqs. (4.122), and (4.123) are given by,

$$\frac{L_{mj}}{L_m} = \left(\frac{A_j}{A_e} - 1\right) \times \left(\frac{\pi/AR}{2 \int_0^{\frac{\pi}{2}} \sqrt{1 - e^2 \sin^2 \theta} d\theta}\right) + 1. \quad (4.124)$$

The similar expression of (L_{nj}/L_n) for the minor axis case is also abided by the preceding rules to measure the size of fully developed jets which is given as,

$$\frac{L_{nj}}{L_n} = \left(\frac{A_j}{A_e} - 1 \right) \times \left(\frac{\pi}{2 \int_0^{\frac{\pi}{2}} \sqrt{1 - e^2 \sin^2 \theta} d\theta} \right) + 1. \quad (4.125)$$

Therefore, the shock size measuring formula provides the related information of shock effects and strength of shock-cell structure. Wave propagations, expansion, frequency tone and noise intensity can be measured through the size and shape of shock-cell structures.

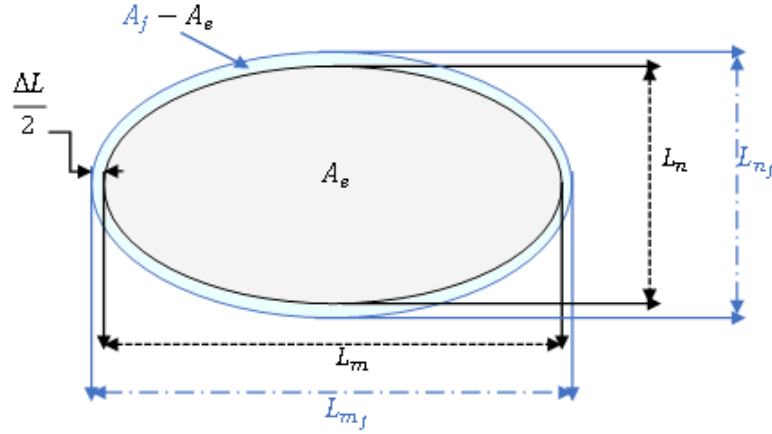


Fig. 4.4: A display of fully expanded jet size in comparison with nozzle exit jet size.

4.6 Results and Discussion

4.6.1 Theoretical Analysis of Elliptic Jets

4.6.1.1 Elliptic Centerline Density with Circular Profile

A modified theoretical centerline density outlines of supersonic jet issued from a convergent-divergent elliptic nozzle of $AR = 2.0$ are compared with the equivalent circular diameter (1 mm) of experiment under the condition of $NPR = 3.0$, $M_d = 1.0$ illustrating in Fig. 4.5. The black solid line is the rainbow schlieren deflectometry result, the green line Tam's [16] circular theory, the magenta line modified circular theory for $\eta = 0.0026$ are presented in Fig. 4.5 for the accuracy of modified elliptic theories which are applied to explore the pink and blue solid lines instead of $\eta = 0.00$, and $\eta = 0.0026$ respectively. In the explicit elliptic solution, the first order ($n = 0$) even Mathieu function and first zero ($m = 1$) of radial Mathieu function have been considered significantly. The necessary scripts of MATLAB have been executed to evaluate the coefficients of Mathieu functions up to 25th position of eigen vectors by using the recurrence formulas and orthogonal properties. The abscissa (z) is the

normalized by the equivalent diameter (D_{eq}) of elliptic nozzle exit and the ordinate is the density (ρ) normalized by the ambient density (ρ_b). The magenta and black leftward arrows on the vertical axis indicate the centerline density values of circular modified theories 2.28 and experimental [52] 1.86 respectively, whereas the blue leftward arrow is specified by the modified elliptic theories value 2.19 calculating upon the assumption of the flow field.

The blue line of modified elliptic theory for $\eta = 0.0026$ shows that a similar decrease and increase in density are quasi-periodically repeated in the downstream direction with a gradual decrease in the local maxima and minima of the density profile. Instead, the modified elliptic density for $\eta = 0.00$ (pink curve) exhibits a periodical curve alike Tam's [16] circular theory for inviscid jet, but the green line shows more deviation than the pink one. Consequently, both the modified circular magenta curve and elliptic blue curve for $\eta = 0.0026$ are shown in qualitatively excellent agreement with the circular black curve where the attenuation of shock-cells significantly follow the experimental properties, while the blue curve is fitted more precisely than the magenta curve. These theories conclude that an elliptical jet can emit less noise than each circular jet which is consistent with the experimental result of [42].

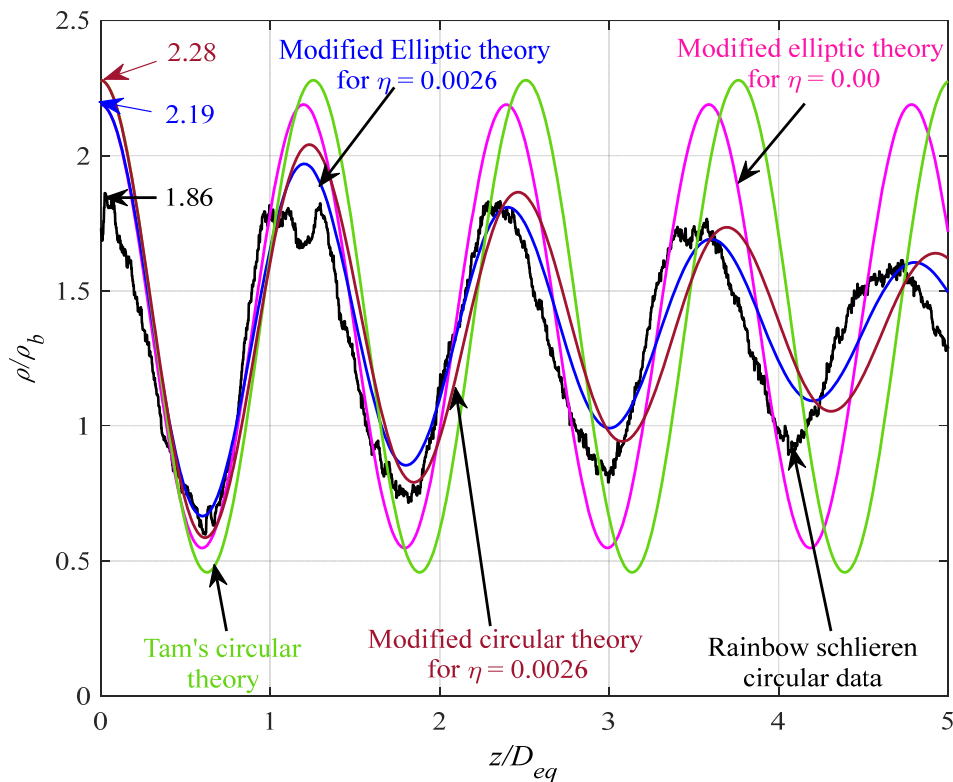


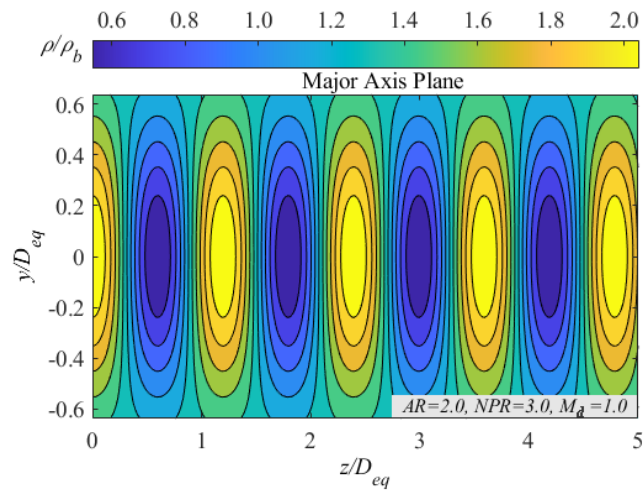
Fig. 4.5: Comparison of elliptic centerline density with RSD circular profiles [52].

4.6.1.2 Theoretical Elliptic Density Contour Plots

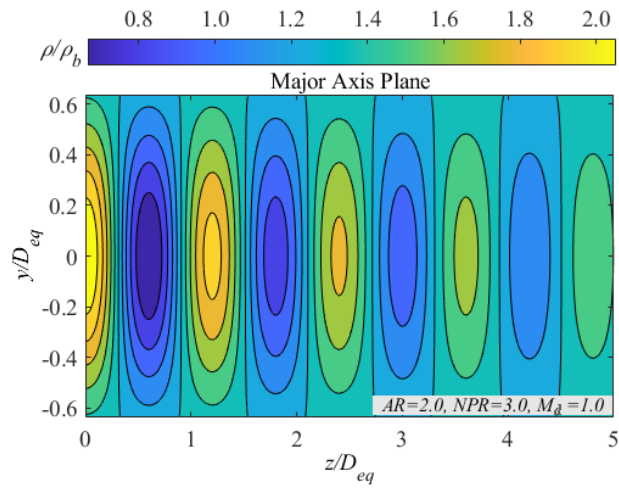
Theoretical elliptic models, including the complete solution of the underlying jet, provide only speculative rough results for the prediction of a particular flow. Still, it can be used as a comparison to validate the results obtained in the test. However, the validity of the simulation should be compared to the shock wave shape, especially the rainbow schlieren deflectometry described in Chapter 3. The calculated modified densities help collecting complete ideas about the elliptic flow components, such as the size and shape of expansion and compression, the spacing between shock cells and structures, and jet boundaries which are illustrated as the contour plots through Figs. (4.6 ~ 4.8) where jet flows from left to right direction. Figure 4.6(c) of experimental circular contour is taken to compare the modified elliptic results of major axis plane view showing in Figs. 4.6(a) to 4.6(b) where $AR = 2.0$, $NPR = 3.0$, $M_d = 1.0$, and eigenvalue expansion of the first mode, ($m = 1$) are considered in MATLAB scripts. The specific heat constant, $\gamma = 1.4$ for quiescent air is performed from elliptic exit geometry where the axes are normalized by the exit equivalent diameter, D_{eq} and the field of density (ρ) is normalized by the ambient density (ρ_b).

Figure 4.6(c) is assumed as a standard density distribution where expansion and compression waves are spaced periodically, and local maxima-minima are decreased gradually along with the downstream direction from the exit, which implies that far distance shocks along the flow direction are less strong than the nearer of nozzle exit, because of back pressure, p_b effects. Sequentially, Figs. 4.6(a) and 4.6(b) are illustrated by the modified theories for $\eta = 0.00$ and $\eta = 0.0026$ separately where the first one is appearing equally spaced shocks for inviscid jet, whereas second one displays qualitatively similar density distribution with Fig. 4.6(c) which is gradually diminishing along with the downstream distance, because of turbulent viscous effect. According to the analysis of Figs. 4.7(a1) ~ 4.7(b2) and Figs. 4.8(a1) ~ 4.8(b2), the number of shock-cells are increased on major and minor axis, but the length and size of shock-cells is slightly decreased with increasing the design Mach number M_d while AR and NPR are remain unchanged. Again, in Figs. 4.7(b1) ~ 4.7(c2) and Figs. 4.8(b1) ~ 4.8(c2), the shock-cells are decreasing on both major and minor axis, while length and size of shocks are increasing with the increasing of NPR , but fixing AR , M_d . Sequentially, Figs. 4.7(c1) ~ 4.7(d2) and Figs. 4.8(c1) ~ 4.8(d2) shows that the shock-cells increase, but length and size decrease remarkably with the increase of aspect ratio (AR) in both axes, whereas NPR , and M_d keeps same value. It should be noted that the changes of AR s closely relate with NPR , while changes

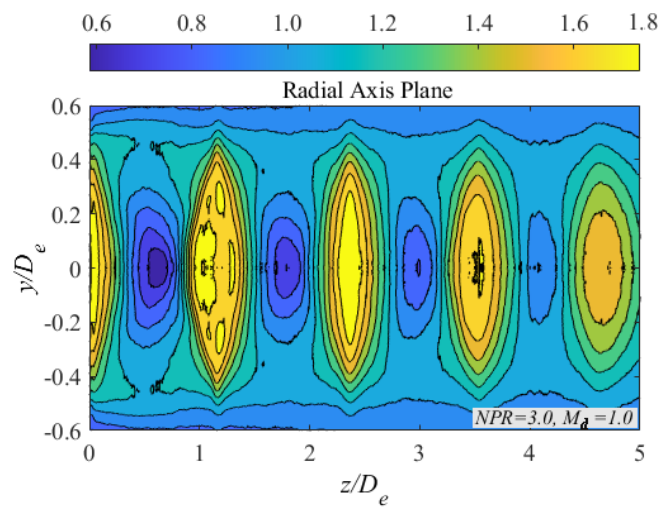
of NPR depend on the condition [Eq. (3.59)] of M_j and M_d for getting feasible flow features.



(a) Modified theory for $\eta = 0.00$



(b) Modified theory for $\eta=0.0026$



(c) Rainbow schlieren circular data

Fig. 4.6: Comparison of density contour plots of elliptic theories with circular RSD [52].

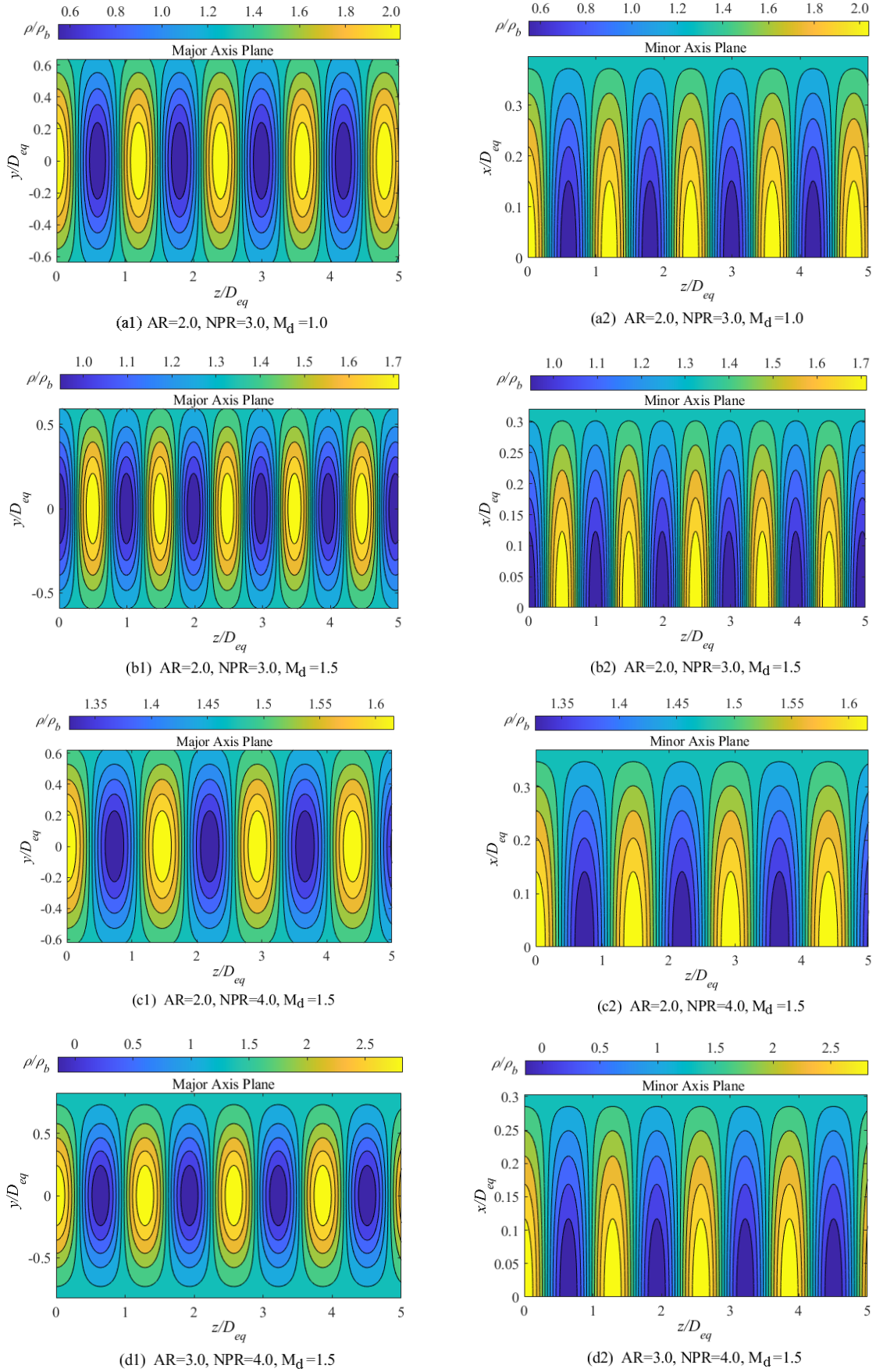


Fig. 4.7: Density contours variation of Modified elliptic theory for $\eta = 0.00$.

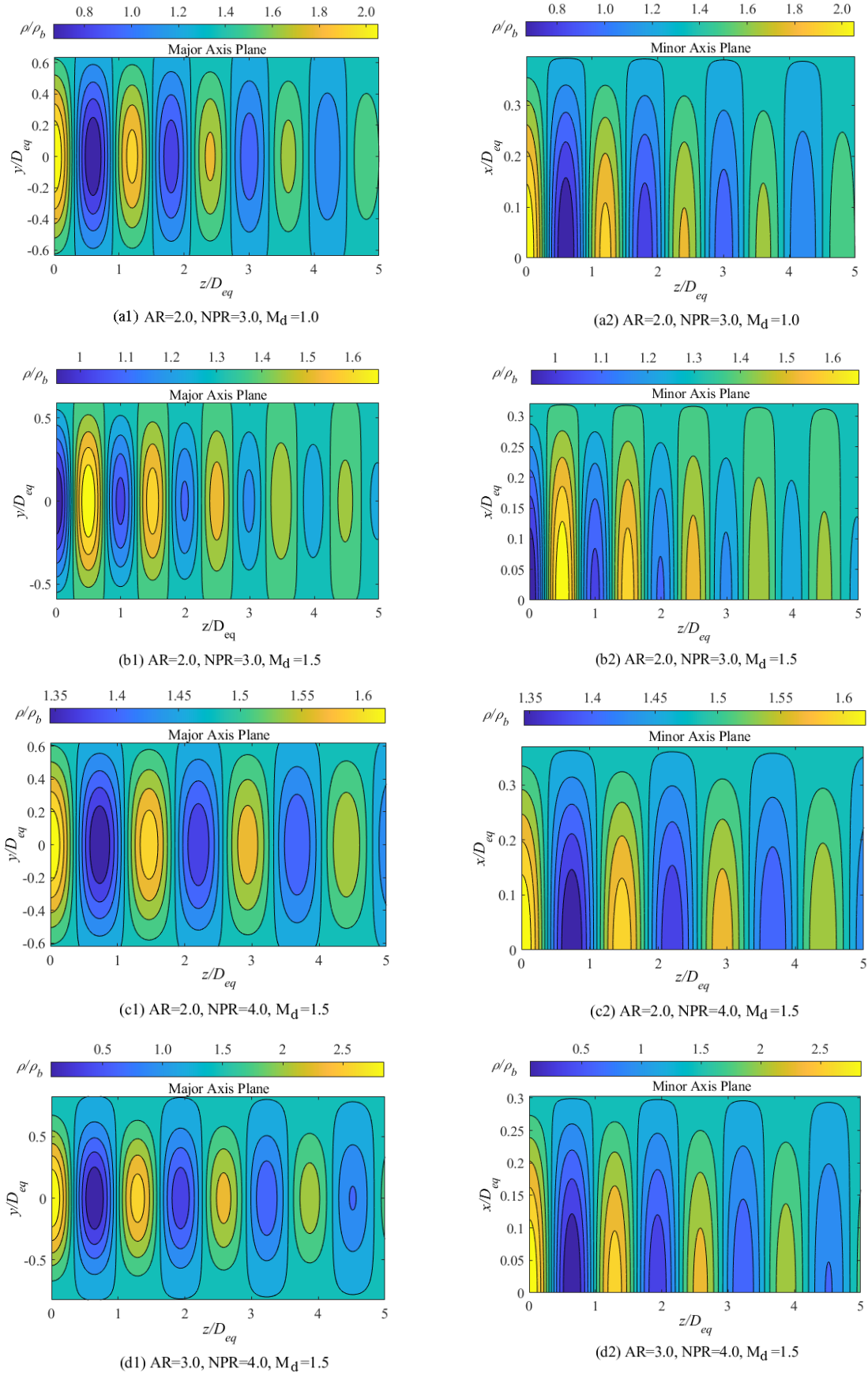


Fig. 4.8: Density contours variation of Modified elliptic theory for $\eta = 0.0026$.

4.6.1.3 Theoretical Elliptic Density Mesh Plots with Contour

The mesh plots of three different densities, including the contour plot of the under-expanded elliptical jet, are shown on a 3D jet surface, as shown in Figs. 4.9 (a) ~ 4.9 (c). The change of fluid properties with the environment may impact on the flow features which can be predicted by analyzing the hypothetical mesh density plots. Figure 4.9(a) modified density theory for inviscid elliptic jet, Fig. 4.9(b) modified theory for elliptic turbulent viscous jet, and Fig. 4.9(c) displays RSD circular data while $AR = 2.0$, $NPR = 3.0$, $M_d = 1.0$ are used where is required. The normalized streamwise distance (z/D_{eq}), normalized major axis (y/D_{eq}), and normalized density (ρ/ρ_b) are stated by the length, width, and height, respectively. The expansion waves and compression waves of shock cell structures are characterized by the orange and green shapes, each, however the jet boundary based upon the assumption of the underexpanded flow from the inlet of the nozzle to the exit is specified through the shadow blue zone. The associate transformation between Cartesian with elliptic co-ordinates and the first Fourier mode are considered to describe the fully expanded jet mesh density by the modified theories of elliptic model.

Figure 4.9(c) demonstrates that the experimental mesh density is gradually diminishes with downstream distance from the nozzle exit on the lower plat, while the state of being is configured by the contour at the upper plat. A three-dimensional schema of first shock-cell structure is built at the first local maximum belonging to the sufficiently minimum value which is underneath the ambient density instead of a progressive increase in the downstream direction. A comparable quasi-periodical expansion and compression waves are repeating itself along the downstream direction with a gradual reduction of the local maxima and minima in the mesh density. Finally, the jet boundary is affected by the ambient pressure when the expanded jet density closes to the ambient density.

The fully expanded modified density mesh plots of elliptic jets are aligned at the bottom layer of Figs. 4.9(a) and 4.9 (b) respectively where the first one is free from turbulent viscosity and the second one has the viscous effect by $\eta = 0.0026$. The modified inviscid mesh in Fig. 4.9(a) points out quantitatively similar agreement with circular experiment Fig. 4.9(c), whereas the modified mesh in Fig. 4.9(b) shows qualitatively parallel pattern with round mesh Fig. 4.9(c).

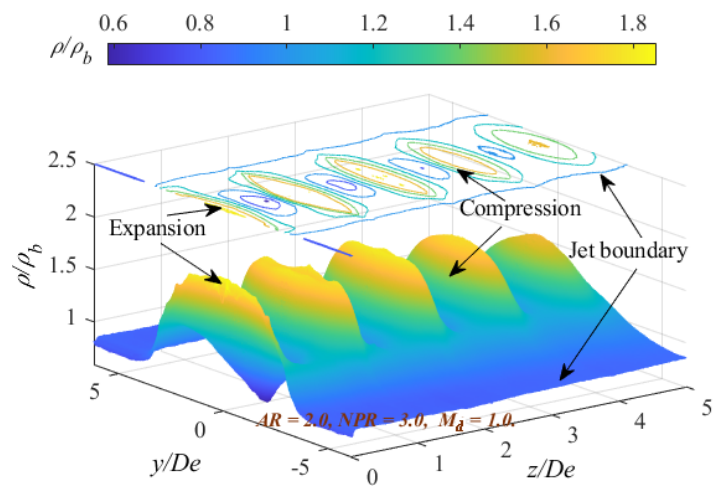
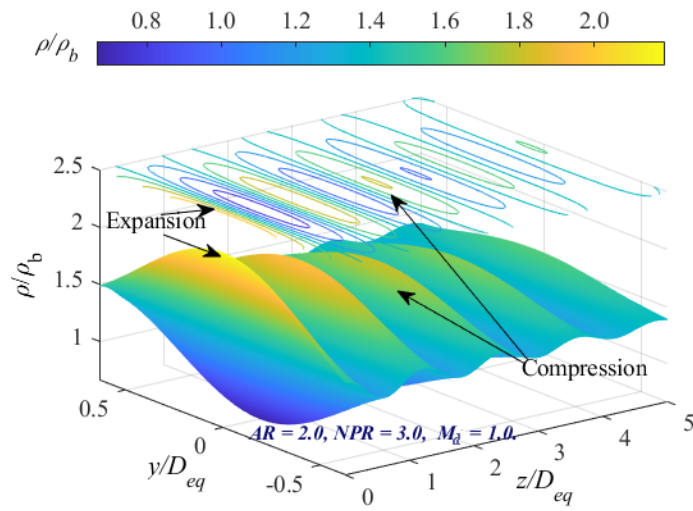
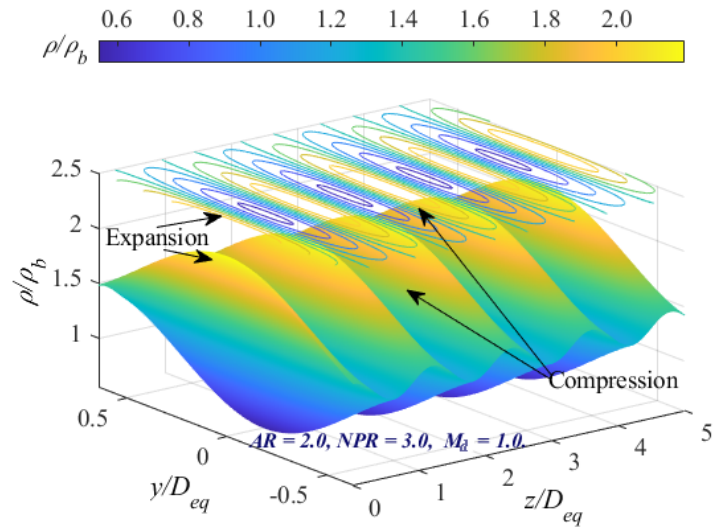


Fig. 4.9: Density Mesh plots with contours underneath of elliptic theory with circular experiment.

4.6.1.4 Analysis of Shock-cell Spacing

It is very important to know the shock-cell spacing, which is significantly related with the shock associated noises [67]. Figure 4.10 shows the variation of the shock-cell spacing for various AR s against the arbitrary NPR with multiple M_d . The embodied black, red, blue, green, purple, and magenta colour shocks spacing are signified by the $AR = 1, 2, 3, 4, 7.72$, and very big AR respectively. Also, two vertical bars at $NPR = 3.23$ and $NPR = 5.77$ are partitioned into three different effective zones which are convinced by Eq. (3.59) for the $M_d = 1.0, 1.5$, and 2.0 . In Fig. 4.10, the shock-cell spacing is normalized by the equivalent diameter of elliptic nozzle exit which is gradually increasing with increases of NPR . The most striking feature is that the shock-cell spacing can be expressed by a single curve. As result, the shock-cell spacing purple line for $AR = 7.72$ is compared with the available Rao [20] experimental pink data for the first time, very good agreement has been shown in Fig. 4.10. In addition, the analytical curve can be clearly classified by design Mach numbers in such a manner that the shock-cell spacing is longer for a higher NPR or M_d .

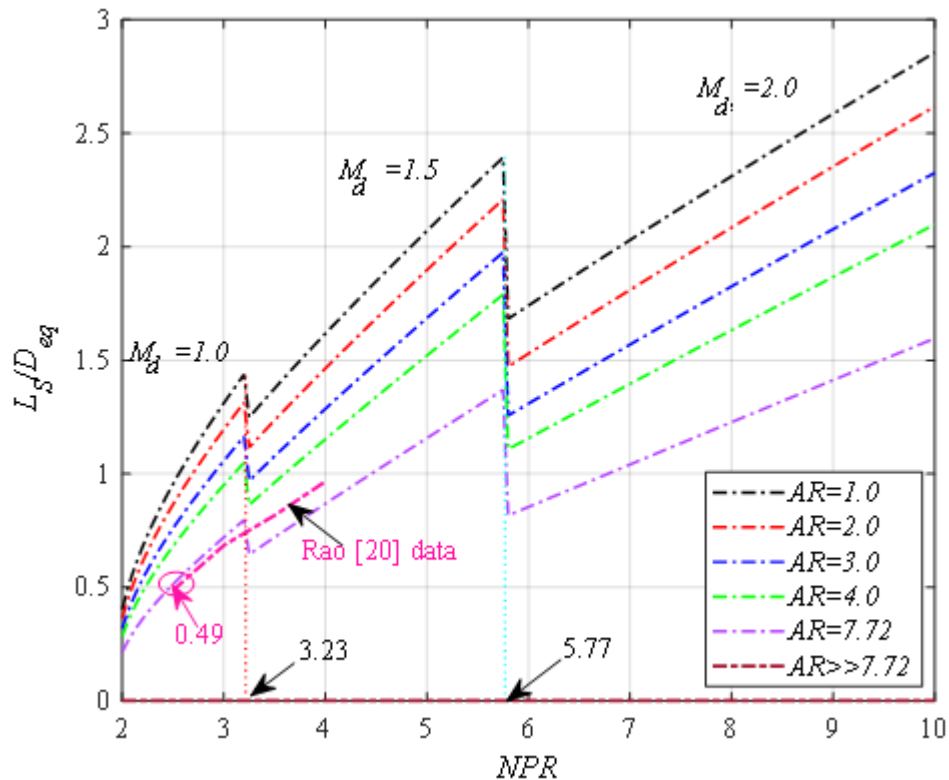


Fig. 4.10: Effect of normalized shock-cell spacing for various AR against arbitrary NPR with several M_d .

4.6.2 Conclusion Remarks of Elliptic Theories

Flow structures of underexpanded jets issued from convergent-divergent nozzles have been studied analytically using the modified elliptic model of shock containing jet. Tam's [17] model has been modified by considering the Reynolds eddy viscosity in momentum equation and imposing perturbed pressure gradient boundary condition. Two distinct explicit solutions have been derived for the inviscid and viscous jet respectively for the first time. Effects of aspect ratio (AR), nozzle pressure ratio (NPR), and design Mach number (M_d) on the jet structures are demonstrated with the static pressure mesh plots and the contour plots on the cross-section at the major axis plane whereas the maximum 25 eigen vectors coefficients of Mathieu function are induced numerically. All the results are compared with equivalent diameter of circular rainbow schlieren deflectometry (RSD) experimental results for the validity of the model and the solutions. In addition, the shock-cell spacings of underexpanded elliptic jets are set out against the NPR for three different significant values of M_d and compared with Rao [20] data for the accuracy of the shock-cell. It is found that the shock-cell spacings for different design Mach numbers can be expressed by a single curve against arbitrary NPR and particular AR as a pioneer work.

Chapter 5

Conclusion

The experimental and analytical results of shock containing circular and elliptic jets were described in previous chapters which lead the following conclusions:

Experimental investigation

- 1) By using the rainbow schlieren deflectometry, a density field of jet emerging from round Laval nozzle followed by a cylindrical duct was measured. To investigate the effect of the nozzle pressure ratio on the jet structure, the three-dimensional density field of jet was reconstructed by the convolution back-projection (CBP) method.
- 2) By an investigation on the centerline density profiles presence of wall friction of round Laval nozzles with and without cylindrical duct, the Laval nozzle with the cylindrical duct exhibited shock-free state at the lower nozzle pressure ratio than the design condition. Also, the freestream Mach number at the exit of duct was almost the same as that calculated based upon the assumption of the isentropic flow.
- 3) The cylindrical duct causes the average Mach number at the exit to be reduced, but not change the freestream Mach number at the duct exit and it smooths the density profile when compared with that for the jet issued from the conventional Laval nozzle.
- 4) To get a three-dimensional flow structure, isopycnic surfaces of overexpanded and underexpanded jets were constructed. It was found that the overexpanded jet produces a Mach disk following by successive weak shocks with a circular shape, while the underexpanded jet forms a bicone structure composed of an oblique shock and expansion waves in each shock-cell, which gradually becomes smaller in shape toward downstream.

Theoretical investigation

1. To get a quantitative theoretical characteristic of an isentropic gas flow, a modified vortex sheet model taking viscosity into account was proposed where circular and elliptic boundary surfaces were examined by the propagated pressures of nozzle exit and fully expanded stream.
2. To calculate the explicit solutions of circular and elliptic jet with and without viscosity separately, the first Fourier mode of eigenvalues expansion, and recurrence relations with orthogonal properties of Bessel's functions for circular jet and Mathieu functions for elliptic jet were executed. The 25 eigenvectors coefficients were also applied in MATLAB scripts to calculate the Mathieu function first time. It was clarified in the explicit solution that square length of Mach numbers of fully extended stream and nozzle exit stream were less than unity and flow properties were normalized by the nozzle exit diameter.
3. The behavior of circular and elliptic jets with viscous and without viscous regimes were examined by the centerline density, density contours, density mesh contours significantly. From the results of the model, it was clarified that the inlet conditions of nozzle influenced to the behavior of flow.
4. To simplify the efficacy of the theoretical results, a comparison among the Tam's [16, 17] theory, Emami's [18] theory with the modified present theory with viscous and without viscous effect of the circular and elliptic jets was executed where the rainbow schlieren deflectometry was as a standard measure. The results of modified theory were exhibited quantitatively excellent agreements with the experiment rather than other models by changing aspect ratios (AR), nozzle pressure ratios (NPR), and design Mach numbers (M_d) arbitrarily.
5. To examine the accuracy of the model, the shock-cell spacing with its parametric effects, and size measuring formulas of elliptic jets were also discussed theoretically and graphically according to normalized fluid properties arbitrarily. By comparing the derived results with the Rao's [20] experiment for the $AR = 7.72$, a satisfactory outcome was found in favor of the modified model. Finally, it was theoretically discovered by the comparison that the modified elliptic jet performed better flow features than the circular one.

Because the purpose of this study is to provide an advanced analytical model with explicit solutions, findings, and reliable experiment data about elliptic and circular phenomena in the shock containing flow field. Various contents were focused on the experiment where the jet was issued through the convergent-divergent nozzle, and the theoretical investigation were also restricted by various assumption for simplification. Therefore, many objects remain unresolved for further clarification and validity. The following recommendations based on this analysis can be concise by,

- ❖ To investigate and get more findings, the underexpanded and overexpanded jet phenomenon in an experimental flow should be conducted through the elliptic duct, elliptic nozzle, and so on. Because lack of reliable data on this field.
- ❖ The effect of molecular interaction and outside disturbances weren't considered in the present model. Therefore, a complete analytical method should be needed, and a great deal of experimental data should be accumulated by considering the normal and shear stress.
- ❖ The first Fourier mode was considered in the present model for the simple flow visualization of the jets at the nozzle exit region. Therefore, the model could be developed by considering the other modes of Fourier series for the distant jet from the nozzle exit.

References

- [1] Harper-Bourne, M. and Fisher, M. J. “The noise from shock waves in supersonic jets”, *Proceedings of the AGARD Conference on noise mechanisms, Brussels, Belgium*. No. 131, (1973).
- [2] Tam, C. K. W., “Stochastic model theory of broadband shock associated noise from supersonic jets”, *Journal of Sound and Vibration*, Vol. 116, (1987), pp. 265-302.
- [3] Franquet, E. Perrier, V., Gibout, S., and Bruel, P., “Free underexpanded jets in a quiescent medium: a review”, *Progress in Aerospace Science*, Vol. 77, (2015), pp. 25-53.
- [4] Scroggs, S.D., and Settles, G.S., “An experimental study of supersonic microjets”, *Experiments in Fluids*, Vol. 21, (1996), pp 401-409.
- [5] Bayt, R. and Breuer, K., “Systems design and performance of hot and cold supersonic microjets”, *AIAA*, No. 2001-0721, (2001).
- [6] Nakao, S. and Takamoto, M.,” Choking phenomena of sonic nozzles at low Reynolds numbers”, *Flow Measurement and Instrumentation*, Vol. 11(4), (2000), pp 285-291.
- [7] Louisos, W.F. and Hitt, D.L., “Heat transfer & viscous effects in 2D & 3D supersonic micro-nozzle flows”, *AIAA Paper*, No. 2007-3987, (2007).
- [8] Kumar, S. M. and Rathakrishnan, E., “Characteristics of a supersonic elliptic jet”, *Aeronautical Journal*, Vol. 120 (1225), (2016), pp. 495-519.
- [9] Tam, C. K. W. and Tanna, H. K., “Shock associated noise of supersonic jets from convergent-divergent nozzles”, *Journal of Sound and Vibration*, Vol. 81, (1982), pp. 337-358.
- [10] Tam, C. K. W. Jackson, J. A. and Seiner, J. M. “A multiple-scales model of the shock-cell structure of imperfectly expanded supersonic jets.”, *Journal of Fluid Mechanics*, Vol. 153, (1985), pp. 123-149.

- [11] Tam, C. K. W. “Broadband shock-associated noise of moderately imperfectly expanded supersonic jets”, *Journal of Sound and Vibration*, Vol. 140 (1), (1990), pp. 55-71.
- [12] Morris, P. J. and Miller, S. A. E., “The prediction of Broadband Shock-Associated Noise using RANS CFD”, *AIAA Paper*, No. 2009-3315.
- [13] Kalyan, A. Karabasov, S. A., “Broad band shock associated noise predictions in axisymmetric and asymmetric jets using an improved turbulence scale model”, *Journal of Sound and Vibration*, Vol. 394, (2017), pp. 392–417.
- [14] Love, E.S., Grigsby, C.E., Lee, L.P., Wooding, M.J., “Experimental and theoretical studies of axisymmetric free jets,” *NASA Technical Report R-6*, (1959).
- [15] Fukunaga, R. Islam, M. M. Awata, Y. Nakao, S. and Miyazato, Y., “Application of Rainbow Schlieren Deflectometry for Jets from Round Laval Nozzles followed by cylindrical Ducts”, *Journal of Flow Control, Measurement & Visualization*, Vol. 9, (2021), pp. 15-27.
- [16] Tam, C. K. W. “On the noise of a nearly ideally expanded supersonic jet”, *Journal of Fluid Mech.*, Vol. 51 (1), (1972), pp. 69-95.
- [17] Tam, C.K.W., “The shock-cell structure and screech tone frequencies of rectangular and non-axisymmetric supersonic jets”, *Journal of Sound and Vibration*, Vol. 12, No.1, (1988), pp. 135-147.
- [18] Emami, B. Bussmann, M. Tran, H. N., “A mean flow field solution to a moderateley under/over-expanded turbulence supersonic jet”, *Comptes Rendus Mécanique*, Vol. 337(4), (2009), pp. 185-191.
- [19] Witze, P. O., “Centerline velocity decay of compressible free jet”, *AIAA Journal*, Vol. 12(4), (1974), pp. 416-418.
- [20] Rao, A. N., Kushari, A., and Mandal, A. C.: Screech characteristics of under-expanded high aspect ratio elliptic jet, *Physics of Fluids*, Vol. 32, (2020), 076106.
- [21] Settles, G.S., “Schlieren and Shadowgraph Techniques: Visualizing Phenomena in Transparent Media”, *Springer*, Berlin, 1st Edition, (2001).

- [22] Sugawara, S. Nakao, S. Miyazato, Y. and Ishino, Y., “Application of Twyman-Green Interferometers for Shock-Containing Free Jets from Axisymmetric Convergent Micro Nozzles”, *Proceedings of 18th International Symposium on Flow Visualization* (ed. T. R ösgen). ETH Zurich, (2018).
- [23] Sugawara, S. Nakao, S. Miyazato, Y. Ishino, Y. and Miki, K., “Three-Dimensional Reconstruction of a Microjet with a Mach disk by Mach-Zehnder Interferometers”, *Journal of Fluid Mechanics*, Vol. 893 (A25), (2020).
- [24] Kaganovich, D. Johnson, L.A. Mamonau, A.A. and Hafizi, B., “Benchmarking Background Oriented Schlieren against Interferometric Measurement Using Open-Source Tools, *Applied Optics*, Vol. 59, (2020), pp. 9553-9557.
- [25] Nicolas, F. Donjat, D. Leon, O. Le Besnerais, G. Champagnat, F. and Micheli, F., “3D Reconstruction of a Compressible Flow by Synchronized Multi-Camera BOS”, *Experiments in Fluids*, Vol. 58 (46), (2017).
- [26] Mariani, R. Zang, B. Lim, H.D. Vevek, U.S. New, T.H. and Cui, Y.D., “A Comparative Study on the Use of Calibrated and Rainbow Schlieren Techniques in Axisymmetric Supersonic Jets”, *Flow Measurement and Instrumentation*, Vol. 66, (2019), pp. 218-228.
- [27] Nazari, A.Z. Ishiko, Y. Ito, F. Kondo, H. Yamada, R. Motohiro, T. Miyazato, Y. and Nakao, S., “Multi-Schlieren CT Measurements of Supersonic Microjets from Circular and Square Micro Nozzles”, *Journal of Flow Control, Measurement & Visualization*, Vol. 8, (2020), pp. 77-101.
- [28] Takano, H. Kamikihara, D. Ono, D. Nakao, S. Yamamoto, H. and Miyazato, Y., “Three-Dimensional Rainbow Schlieren Measurements in Underexpanded Sonic Jets from Axisymmetric Convergent Nozzles”, *Journal of Thermal Science*, Vol. 25, (2016), pp. 78-83.
- [29] Maeda, H. Fukuda, H. Kubo, K. Nakao, S. Ono, D. and Miyazato, Y., “Structure of Underexpanded Supersonic Jets from Axisymmetric Laval Nozzles”, *Journal of Flow Visualization and Image Processing*, Vol, 25, (2018), pp. 33-46.

- [30] Mariani, R. Zang, B. Lim, H.D. Vevek, U.S. New, T.H. and Cui, Y.D., “On Application of Non-Standard Rainbow Schlieren Technique upon Supersonic Jets”, *Journal of Visualization*, Vol. 23, (2020), pp. 383-393.
- [31] Agrawal, A.K. and Wanstall, C.T., “Rainbow Schlieren Deflectometry for Scalar Measurements in Fluid Flows”, *Journal of Flow Visualization and Image Processing*, Vol. 25, (2018), pp. 329-357.
- [32] Ezoe, M. Nakao, S. and Miyazato, Y., “Quantitative Flow Visualization by Rainbow Schlieren Deflectometry and Pitot Pressure Measurements for Leek Peeler Nozzle Jets”, *Journal of Flow Control, Measurement & Visualization*, Vol. 7, (2019), pp. 44-60.
- [33] Powel, A., “On the Noise Emanating from a Two-Dimensional Jet Above the Critical Pressure”, *Aeronautical Quarterly*, Vol. 4, (1953), pp. 103-122.
- [34] Hammitt, A. G., “The oscillation and noise of an overpressure sonic jet”, *Journal of Aerospace Sciences*, Vol. 28, (1961), pp. 673-680.
- [35] Prandtl, “Über die Stationären Wellen in einem Gasstrahl”, *Physikalische Zeitschrift* Vol. 5, (1904), pp. 599-601.
- [36] Emden, R., “Ueber die Ausströmungserscheinungen permanenter Gase”, *Annale der Physik*, Vol. 305(10), (1899), pp. 426-453.
- [37] Pack, D. C., “A note on Prandtl's formula for the wavelength of a supersonic gas jet”, *Quarterly Journal of Mechanics and Applied Mathematics*, Vol. 3, (1950), pp. 173-181.
- [38] Howe, M.S. Ffowcs-Williams, J.E., “On the noise generated by an imperfectly-expanded supersonic jet”, *Philosophical Transactions of the Royal Society of London. Series A, Mathematical and Physical Sciences*, Vol. 289(1358), (1978), pp. 271–314.
- [39] Seiner, J. M. Dash, S. M. and Wolf, D. E., “Analysis of turbulent underexpanded jets. Part II: Shock noise features using SCIPVIS”, *AIAA Journal*, Vol. 23, (1985), pp. 669-677.
- [40] Panda, J., “Shock oscillation in under-expanded screeching jets”, *Journal of Fluid Mech.*, Vol. 363, (1998), pp. 173–198.

- [41] Gutmark, E. Schadow, K.C. and Wilson, K. J., “Noncircular jet dynamics in supersonic combustion”, *Journal of Propulsion and Power*, Vol. 5(5), (1989), pp. 529-533.
- [42] Kinzie, K. W. and McLaughlin, D. K., “Aeroacoustics properties of supersonic elliptic jets”, *Journal of Fluid Mechanics*, Vol. 395, (1999), pp. 1-28.
- [43] Menon, N. and Skews, B. W., “Shock wave configurations and flow structures in non-axisymmetric underexpanded sonic jets”, *Shock Waves*, Vol. 20, (2010), pp. 175–190.
- [44] Mitchell, D. M. Honnery, D. R. Soria, J., “Near-field structure of underexpanded elliptic jets”, *Experiments in Fluids*, Vol. 54, (2013), pp. 1-13.
- [45] Li, X. Zhou, R. Yao, W. and Fan, X., “Flow characteristic of highly underexpanded jets from various nozzle geometries”, *Applied Thermal Engineering*, Vol. 125, (2017), pp. 240-253.
- [46] Zucrow, M. J. and Hoffman, J. D., “Gas Dynamics: Volume I”, *John Wiley & Sons, Inc.*, (1976).
- [47] Saad, M. A., “Compressible fluid flow”, *Prentice Hall*, (1993).
- [48] Raisinghania, M. D., “Fluid Dynamics”, *S. Chand and Company Ltd*, (2010).
- [49] https://courses.ansys.com/wp-content/uploads/2021/04/Lesson2_CB_Image.png
- [50] Katanoda, H. Matsuoka, T. and Matsuo, K., “Experimental Study on Shock Wave Structures in Constant-Area Passage of Cold Spray Nozzle”, *Journal of Thermal Science*, Vol.16, (2007), pp. 40-45.
- [51] Zahiri, S.H. Yang, W. and Jahedi, M., “Characterization of Cold Spray Titanium Supersonic Jet”, *ASM International*, Vol. 18, (2009), pp. 110-117.
- [52] Islam, M. M. Fukunaga, R. Nakao, S. and Miyazato, Y., “Comparison of Theoretical Models and Rainbow Schlieren Deflectometry for Slightly Underexpanded Microjets”, *Seventeenth International Conference on Flow Dynamics*, (2020), pp. 62-63.

- [53] Islam, M. M. Fukunaga, R. Nakao, S. and Miyazato, Y., “Assessment of Linearized Shock-cell Models for Axisymmetric Underexpanded jets by Rainbow Schlieren Deflectometry”, *Eighteenth International Conference on Flow Dynamics*, (2021), pp. 125-127.
- [54] https://en.wikipedia.org/wiki/Cylindrical_coordinate_system#Definition
- [55] Foelsch, K., “The Analytical Design of an Axially Symmetric Laval Nozzle for a Parallel and Uniform Jet”, *Journal of Aeronautical Sciences*, Vol.16, (1949), pp. 161-166.
- [56] Awata, Y. Nakao, S. and Miyazato, Y., “Density Measurements in Free Jets from Axisymmetric Supersonic Nozzles with Constant-Area Straight Ducts”, *Proceedings of 18th International Symposium on Flow Visualization*, (2018), (ed. T. R ösgen). ETH Zurich.
- [57] Matsuo, K. Miyazato, Y. and Kim, H.D., “Shock Train and Pseudo-Shock Phenomena in Internal Gas Flows”, *Progress in Aerospace Sciences*, Vol.35, (1999), pp. 33-100.
- [58] John, J.E.A., “Gas dynamics, 2nd edition”, *Allyn and Bacon*, (1984).
- [59] Miyazato, Y. Sakamoto, S. and Matsuo, K., “An experiment on choking phenomena in supersonic Fanno flows”, *Transactions of the JSME*, Vol. 73, (2007), pp. 2393-2396 (in Japanese).
- [60] Ihme, M., “Combustion and engine-core noise”, *Annual Review of Fluid Mechanics*, Vol. 49, (2017), pp. 277–310.
- [61] Edgington-Mitchell, D., “Supersonic jet screech: Half-century from Powell to the present”, *International Journal of Aeroacoustics*, Vol. 18, (2019), pp. 118–188.
- [62] Yoon, J. H., and Lee, S. J., “Investigation of the near-field structure of an elliptic jet using stereoscopic particle image velocimetry”, *Measurement Science and Technology*, Vol. 14, (2003), pp. 2034–2046.
- [63] Edgington-Mitchell, D.M. Honnery, D. R. and Soria, J., “Multimodal instability in the weakly underexpanded elliptic jet”, *AIAA Journal*, Vol. 53, (2015), pp. 2739–2749.

- [64] McLachlan, N. W., “Theory and Application of Mathieu Functions: 1st edition”, *Oxford University: Geoffery Cumberlege*, (1947).
- [65] Islam, M. M. Nagata, T. Nakao, S. and Miyazato, Y., “Theoretical Study of Supersonic Elliptic Jets”, *The 7th International Conference on Jets, Wakes and Separated Flows*, (2022), pp. 237–244.
- [66] Mores, P. M., and Feshbach, H., “Method of Theoretical Physics”, *New York, McGraw-Hill*, (1953).
- [67] Tam, C.K.W., “Supersonic Jet Noise”, *Annual Review of Fluid Mechanics*, Vol. 27, (1995), pp. 17-43.